INFORMATION TO USERS

While the most advanced technology has been used to photograph and reproduce this manuscript, the quality of the reproduction is heavily dependent upon the quality of the material submitted. For example:

- Manuscript pages may have indistinct print. In such cases, the best available copy has been filmed.

- Manuscripts may not always be complete. In such cases, a note will indicate that it is not possible to obtain missing pages.

- Copyrighted material may have been removed from the manuscript. In such cases, a note will indicate the deletion.

Oversize materials (e.g., maps, drawings, and charts) are photographed by sectioning the original, beginning at the upper left-hand corner and continuing from left to right in equal sections with small overlaps. Each oversize page is also filmed as one exposure and is available, for an additional charge, as a standard 35mm slide or as a 17"x 23" black and white photographic print.

Most photographs reproduce acceptably on positive microfilm or microfiche but lack the clarity on xerographic copies made from the microfilm. For an additional charge, 35mm slides of 6"x 9" black and white photographic prints are available for any photographs or illustrations that cannot be reproduced satisfactorily by xerography.

Order Number 8721778

Fluctuations in dc SQUIDs: Quantum noise effects, low frequency noise, and single electron trapping

Wakai, Ronald Tatsuya, Ph.D.

University of Illinois at Urbana-Champaign, 1987

U·M·I

300 N. Zeeb Rd.
Ann Arbor, MI 48106

FLUCTUATIONS IN DC SQUIDS: QUANTUM NOISE EFFECTS, LOW FREQUENCY NOISE, AND SINGLE ELECTRON TRAPPING

BY

RONALD TATSUYA WAKAI

A.B., Cornell University, 1980
M.S., University of Illinois, 1981

THESIS

Submitted in partial fulfillment of the requirements
for the degree of Doctor of Philosophy in Physics
in the Graduate College of the
University of Illinois at Urbana-Champaign, 1987

Urbana, Illinois

UNIVERSITY OF ILLINOIS AT URBANA-CHAMPAIGN

THE GRADUATE COLLEGE

MAY 1987

WE HEREBY RECOMMEND THAT THE THESIS BY

RONALD TATSUYA WAKAI

ENTITLED FLUCTUATIONS IN DC SQUIDS: QUANTUM NOISE EFFECTS, LOW FREQUENCY NOISE, AND SINGLE ELECTRON TRAPPING

BE ACCEPTED IN PARTIAL FULFILLMENT OF THE REQUIREMENTS FOR THE DEGREE OF DOCTOR OF PHILOSOPHY IN PHYSICS

Dale J. Van Harlingen
Director of Thesis Research

C C Anderson
Head of Department

Committee on Final Examination†

Dale J Van Harlingen
Chairperson

Gail Bayn

H G Drickamer

Bob Eisenstein

† Required for doctor's degree but not for master's

0 517

to my parents

Acknowledgements

First of all, I would like to express my gratitude to Dale Van Harlingen for being an ideal advisor: very patient and knowledgeable. I would also like to thank my fellow group members-- Kendall Springer, Gene Hilton, Fred Sharifi, Jorge Gavilano, and Jui Tien-- for their help and friendship; especially to Gene for assistance in preparing this thesis. I wish them and all my friends from Illinois--remaining or departed-- the best of luck in the future. The indispensible financial support of the University of Illinois at Champaign-Urbana and the National Science Foundation under grant DMR 84 11631 is gratefully acknowledged.

Last, but not least, I would like to thank my parents for their love and encouragement throughout my academic career.

TABLE OF CONTENTS

Chapter 1

INTRODUCTION

Josephson devices have long been of interest to physicists because 1) they are one of the best systems for studying fundamental quantum phenomena and 2) they have given rise to a wide range of some of the best detectors and amplifiers ever made. These qualities are particularly well illustrated by the dc SQUID (Superconducting QUantum Interference Device) where quantum interference of Cooper pairs produces a remarkably sensitive magnetic flux detector. Both signal and noise properties are important in determining the overall SQUID performance and are reasonably well understood in the thermal regime. Interest has now focussed on the need and the potential for producing a practical dc SQUID detector approaching quantum-limited sensitivity. The requirements for achieving such a device will most likely include the ability to produce Josephson junctions capable of very high frequency, low temperature operation. Recent advances in thin-film technology have enabled the fabrication of high quality, submicron-area edge junctions which may satisfy these criteria. Despite this potential, the noise performance of dc SQUIDs based on this technology has not been extensively studied. This thesis presents the results of just such an investigation.

Chapter 2 reviews the elementary signal and noise properties of the dc SQUID. A quantum Langevin theory is used to establish that quantum-limited flux energy resolution can be achieved at low temperatures by using very high critical current density junctions. The advantages of edge junctions for this application are demonstrated in Chapter 3, along

with the development of a Pb-alloy edge junction fabrication process based on electron beam lithography and ion-milling techniques.

The observed signal properties of our SQUIDs reported Chapter 4 are excellent and the noise performance is in reasonable agreement with theory. A minimum flux energy resolution of $1.6\pm.5\hbar$ was measured at 1.5K; this is within a factor of two of the theoretical quantum limit and is the lowest value reported to date. These promising results suggest that the development of an ultrasensitive practical detector based on our SQUID design can be achieved within the near future.

Chapter 5 concerns the unusual low frequency noise properties of our devices. Despite its practical importance, the low frequency noise of dc SQUIDs is not well characterized and its origins are not completely understood. Below about 1MHz, the noise spectrum shows Lorentzian features of varying position and strength superimposed on a background spectrum which is always much flatter than 1/f ($\sim f^{-2/3}$). When these features are strongest, the real-time voltage displays discrete switching events which result from the trapping and untrapping of single electrons into localized defect states residing within the tunneling barrier. The direct observation of these trapping events identifies the resulting critical current fluctuations as the dominant source of low frequency noise in our SQUIDs and provides a useful probe for studying individual electron traps.

Chapter 6 examines the population kinetics of individual electron traps through direct measurement of the discrete voltage switching. The weak temperature dependence (below 4K) of the trap lifetimes reveals that the trapping is dominated by tunneling kinetics, while the voltage bias

dependence is consistent with a simple nonequilibrium model in which the bias enhances the rate for electrons to tunnel into the trap from one side of the barrier and exit out the other side. In addition, the noise does not always exhibit a simple superposition of random telegraph switching when several traps are active at the same time; instead, interactions between the traps can conspire to produce a voltage noise that displays series kinetics. These observations show that the low-frequency noise of this and perhaps other ultra-small systems cannot always be described by a simple parallel kinetics model, composed of independent fluctuators.

Chapter 2

SIGNAL AND NOISE PROPERTIES OF JOSEPHSON JUNCTIONS AND DC SQUIDS

This chapter comprises an introduction to the properties of Josephson junctions and dc SQUIDs which are needed to understand the experimental results in subsequent chapters. The first few sections are aimed towards explaining the Josephson effect and electron tunneling in Josephson junctions. This is intended to motivate the use of the RSJ (resistively-shunted junction) model which forms the basis for studying junction dynamics. Two excellent reviews of these topics are by Waldram (1976) and Anderson (1967). Thermal noise theory is then discussed within the context of the RSJ model and the Langevin equation. The basic principles underlying the Langevin method are examined and this technique is then extended to the quantum noise regime where qualitative effects are predicted at low temperatures in very small-area Josephson junction devices. In particular, quantum-limited performance may now be attainable in practical SQUID detectors using state-of-the-art microfabrication techniques. This possibility provides the motivation for developing high resolution dc SQUIDs and studying their noise properties.

2.1 Superconductivity

Although an elementary knowledge of superconductivity is important for understanding many aspects of Josephson devices, most of the results in this thesis can be understood in terms of a simple discrete model of a Josephson junction known as the RSJ model. Therefore, only a qualitative

review of superconductivity is presented here and the microscopic BCS theory is largely avoided. Standard references such as Tinkham (1975) and DeGennes (1966) should be consulted for a more complete and rigorous introduction to the subject.

Superconductivity was first experimentally observed in 1911 by Kammerlingh Onnes; however, it was not theoretically understood until 1957 when the BCS theory of Bardeen, Cooper, and Schrieffer (1957) was formulated. The mechanism responsible for superconductivity is a very subtle phonon-mediated attraction between electrons which can be neglected in a normal metal. Below the transition temperature, T_c, this causes the electrons to form weakly bound pairs, known as Cooper pairs, which all condense into the same two-electron state. These Cooper pairs do not behave like independent particles; they are locked together in a complicated way so that the condensate forms a single collective quantum state. BCS theory was remarkably successful in explaining the microscopic nature of this ground state, but the response of the superconductor to fields and perturbing forces is most easily characterized in terms of a complex order parameter, $\psi = |\psi| \, e^{i\theta}$, which obeys a Schrodinger-like (Ginzburg-Landau) equation and can be thought of as the center-of-mass wavefunction for all the Cooper pairs. The amplitude of ψ is related to the pair density which is essentially constant throughout the superconductor, while the phase is related to the pair velocity, v_s, through

$$mv_s = \hbar \nabla\theta - (2e/c) \mathbf{A} \qquad (2.1)$$

where **A** is the vector potential. Only differences in phase are

physically significant; the absolute value is arbitrary. This simple order parameter description is possible because the condensate exhibits long-range phase coherence; i.e. the phase of the Cooper pairs is everywhere well-defined and the phase difference between any two points in the superconductor is simply given by (2.1). In contrast, electrons in a normal metal lose phase coherence over length scales comparable to the inelastic scattering length, typically less than one micron. Another important property of superconductors is perfect diamagnetism; superconductors expel all magnetic flux from the interior by generating surface screening currents. The **B** field decays exponentially from the surface over a distance, λ, known as the London penetration length . Therefore, no fields or currents are present within the interior of bulk superconductors with dimensions larger than λ.

A striking manifestation of long-ranged phase coherence is flux quantization in superconducting rings (Figure 2.1). Since the current (and pair velocity) is zero inside a superconductor, the vector potential causes the phase to change according to:

$$\nabla\theta = 2eA/\hbar c \qquad (2.2)$$

In addition, long-range phase coherence requires that the phase must be single valued around the ring. Applying the usual periodic boundary conditions, we find:

$$(2e/\hbar c) \oint A \cdot dl = 2\pi n \qquad (2.3)$$

or

$$\Phi = n(h/2e) \qquad (2.4)$$

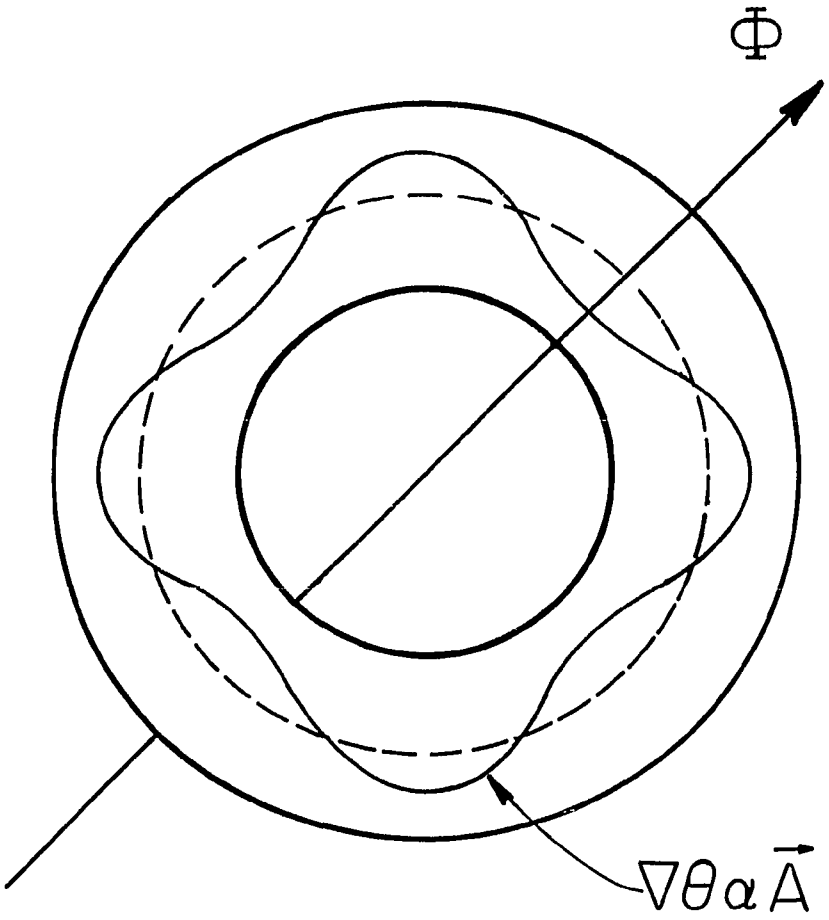

Figure 2.1 - Flux quantization in a superconducting ring imposed by long-range phase coherence.

which says that the flux through the ring is quantized in units of the fundamental flux quantum h/2e. Flux quantization is closely related to an important principle (quantum interference) of SQUID operation.

2.2 Superconductive tunneling: the Josephson effects

A Josephson junction (Figure 2.2a) consists of two superconducting electrodes separated by a very thin (~20Å) insulator which forms a quantum mechanical tunneling barrier. The current-voltage (I-V) characteristic of these junctions usually displays a very nonlinear quasiparticle conductance as shown in Figure 2.2b. Quasiparticles-- essentially broken Cooper pairs-- are the elementary excitations of a superconductor. Because of the pair "binding energy", the quasiparticle energy spectrum

$$E_k = (\epsilon_k^2+\Delta^2)^{\frac{1}{2}} \qquad (2.5)$$

exhibits a low energy gap, Δ, where the ϵ_k are the normal state electronic energies measured from the chemical potential. Well below T_c, the small number of thermal quasiparticles results in a small tunneling current at low voltages. But when the applied voltage exceeds $\Delta_L+\Delta_R/e$, it produces a large quasiparticle tunneling current by breaking Cooper pairs.

Prior to 1962, it was believed that the Cooper pairs would participate in the tunneling only through pair breaking; but in that year, Josephson (1962) predicted the existence of pair tunneling. This was completely unexpected because it was thought that the probability for this process to occur would be extremely small since it required the

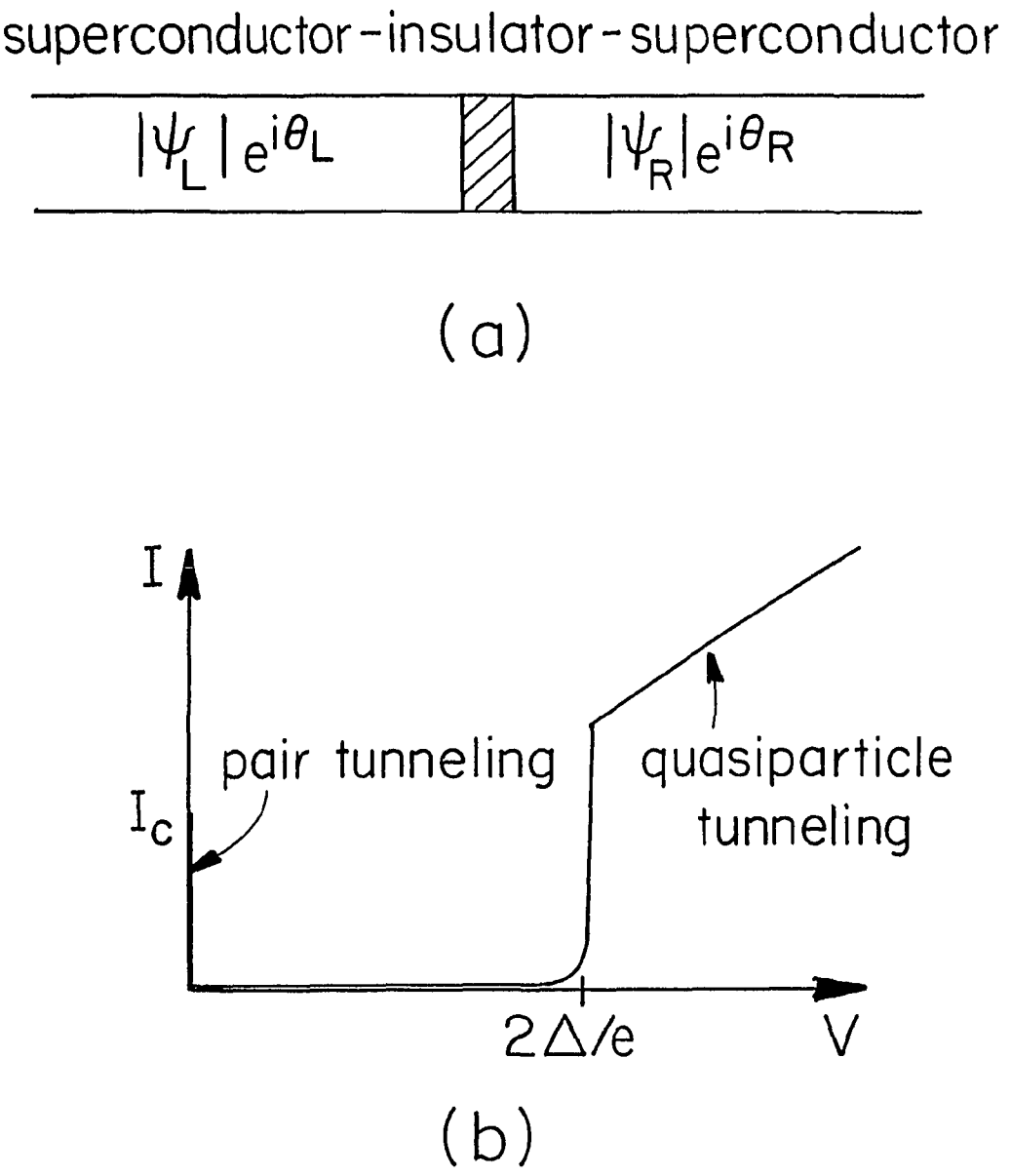

Figure 2.2 - Josephson junction. (a) Superconductor-insulator-superconductor sandwich. (b) Current-voltage characteristic assuming identical superconductors.

simultaneous tunneling of two electrons. Josephson showed that if the tunneling barrier is made very thin, the phases of the order parameters can weakly couple and the pairs will tunnel essentially like single particles. This "weakly-coupled" condition is intermediate between the cases of completely isolated superconductors which have uncorrelated phases and "strongly-coupled" superconductors in intimate contact which act like a single superconductor with the same phase throughout. By definition, the current flow in strongly-coupled superconductors is given by (2.1), while the pair tunneling current between weakly-coupled superconductors is periodic in the phase according to

$$I = I_c \sin\theta \tag{2.6}$$

where $\theta = \theta_L - \theta_R$ is the phase difference between the two order parameters and I_c is the Josephson critical current. To understand why this term is phase-dependent requires some additional insight. The Cooper pairs are not localized on one particular side of the junction, rather, they are in a linear superposition of states, $\psi = \psi_L + \psi_R$, having a large amplitude for being on either side. This coherence lowers the energy of the system by an amount

$$E_J = I_c \Phi_o (1-\cos\theta) \tag{2.7}$$

known as the Josephson coupling energy and it adds a phase dependent interference term to the junction current which corresponds to pair tunneling.

As shown in Figure 2.2b, pair tunneling allows a small dc supercurrent to flow through the junction, but currents larger than the

Josephson critical current cause a voltage to develop. This raises the energy of the Cooper pairs on one side of the junction by an amount $\Delta E = 2eV$. Because the order parameters have the same time dependence as an ordinary wavefunction, $\psi \sim \exp(-iEt/\hbar)$, the phase of the more energetic pairs will evolve more rapidly with time so that the phase difference across the junction changes according to:

$$d\theta/dt = 2eV/\hbar \tag{2.8}$$

Equations (2.7) and (2.8) are known as the Josephson equations and they determine the flow of supercurrent through the junction. Combining them for the case of a voltage-biased (V constant) junction yields:

$$I = I_c \sin(2eVt/\hbar) \tag{2.9}$$

This implies that a dc voltage impressed across the junction produces a monochromatic supercurrent (Josephson) oscillation of very high frequency (486MHz/μV). In practice, the junction is always current biased which causes the oscillations to become very nonlinear; however, this ac Josephson effect forms the basis for using Josephson junctions as a voltage standard and for measuring the fundamental constant h/2e to very high precision (see Taylor et al., 1969).

There is also a predicted contribution to the tunneling due to interference between the quasiparticle and pair currents; however, experiments attempting to measure this effect have led to much controversy (see Langenberg, 1974). Fortunately, this term does not qualitatively alter the junction properties and it is neglected in most analyses.

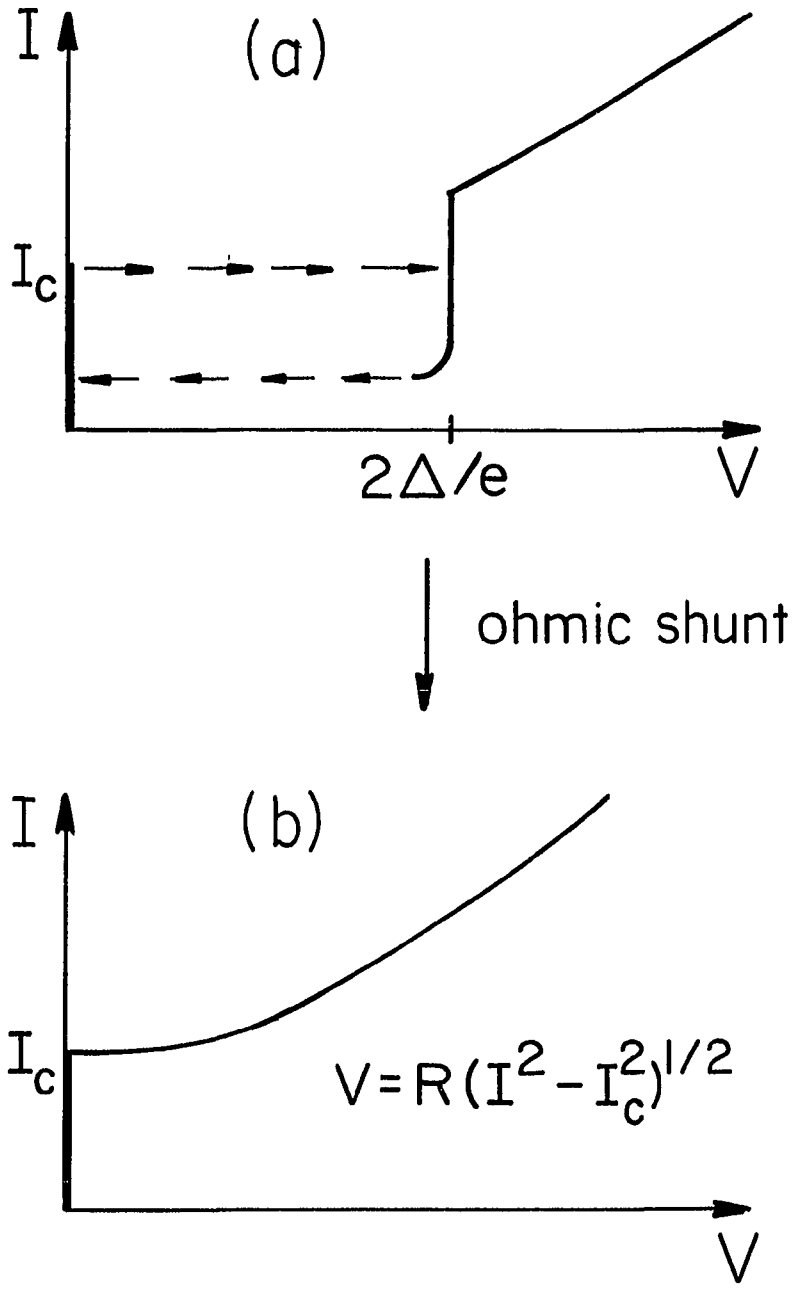

Figure 2.3 - Current-voltage characteristic of Josephson junction for (a) underdamped and (b) overdamped cases.

2.3 The RSJ model

The I-V characteristic of a Josephson junction is intrinsically hysteretic as shown in Figure 2.3a. This is useful for making digital logic elements and also for a number of analog applications which make use of the extreme nonlinearity of the quasiparticle conductance near V= $2\Delta/e$. In particular, superconducting tunnel junctions are now widely used in solid state physics for phonon detection (see Eisenmenger, 1976) and in radioastronomy for millimeter wavelength spectroscopy (see Tucker and Feldman, 1986). However, hysteresis is undesirable for many devices based on the Josephson effect and it can be eliminated by shunting the junction with an ohmic resistance, R, such that the condition

$$\beta_c = (2\pi/\Phi_0)\ I_c R^2 C < 1 \qquad (2.10)$$

is satisfied. The parameter β_c is essentially the ratio of the shunt resistance to the impedance of the parallel capacitance; therefore, the capacitor is often neglected (zero capacitance limit) when this condition is satisfied. The current-voltage (I-V) characteristic for this "overdamped" junction assumes the form shown in Figure 2.3b.

The detailed behavior of shunted Josephson junctions can be understood using the resistively-shunted junction or RSJ model (Stewart, 1969, McCumber, 1968). This simple model also allows the dynamics of more complicated Josephson devices (such as the dc SQUID) to be accurately simulated on a computer and thereby optimized with respect to device parameters and bias conditions. The RSJ model (Figure 2.4) consists of an ideal Josephson element (which obeys the Josephson equations) in parallel with an ohmic resistance and the intrinsic

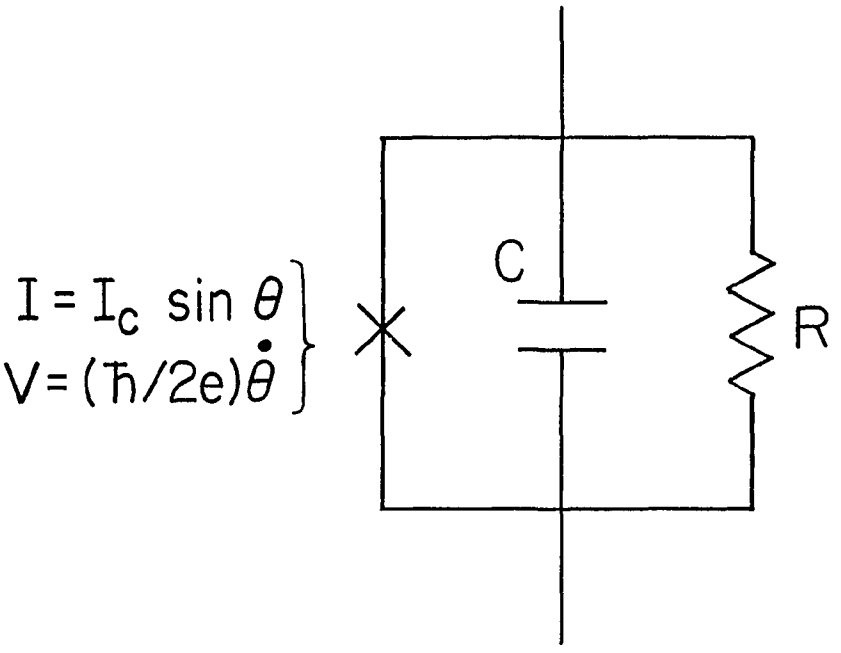

Figure 2.4 - Schematic of resistively shunted junction (RSJ).

junction capacitance. To derive the equation of motion for a current-biased RSJ, we write down the total current through the device:

$$C\ (dV/dt) + V/R + I_c \sin\theta = I \qquad (2.11)$$

and then substitute in for the voltage in terms of the phase using the Josephson relation $2eV = d\theta/dt$.

$$C\ (d^2\theta/dt^2) + (1/R)(d\theta/dt) - (2\pi/\Phi_0)(I - I_c \sin\theta) = 0 \qquad (2.12)$$

This equation is well known from problems in nonlinear dynamics such as chaos and charge density waves. Solving for the time dependence of the phase, we can extract the mean voltage as a function of the total current and the parameter β_c to obtain the dc I-V characteristics. An analytic solution is possible only for the case $\beta_c = 0$ (zero capacitance limit) shown in Figure 2.3b:

$$V = 0 \quad , I < I_c \qquad (2.13)$$
$$V = R\ (I^2 - I_c^2)^{1/2} \quad , I > I_c$$

However, all the $\beta_c < 1$ (nonhysteretic) solutions are essentially identical. Although the detailed behavior of (2.12) is very complicated, it can be thought of as the force equation for a damped (phase) particle of mass C moving in a washboard shaped potential

$$U(\theta) = (2\pi/\Phi)(I - I_c \cos\theta) \qquad (2.14)$$

This so-called washboard analog can be used to help visualize the dynamics of the RSJ. Plotted in Figure 2.5 is the washboard potential for different values of the washboard slope. In this analogy, the

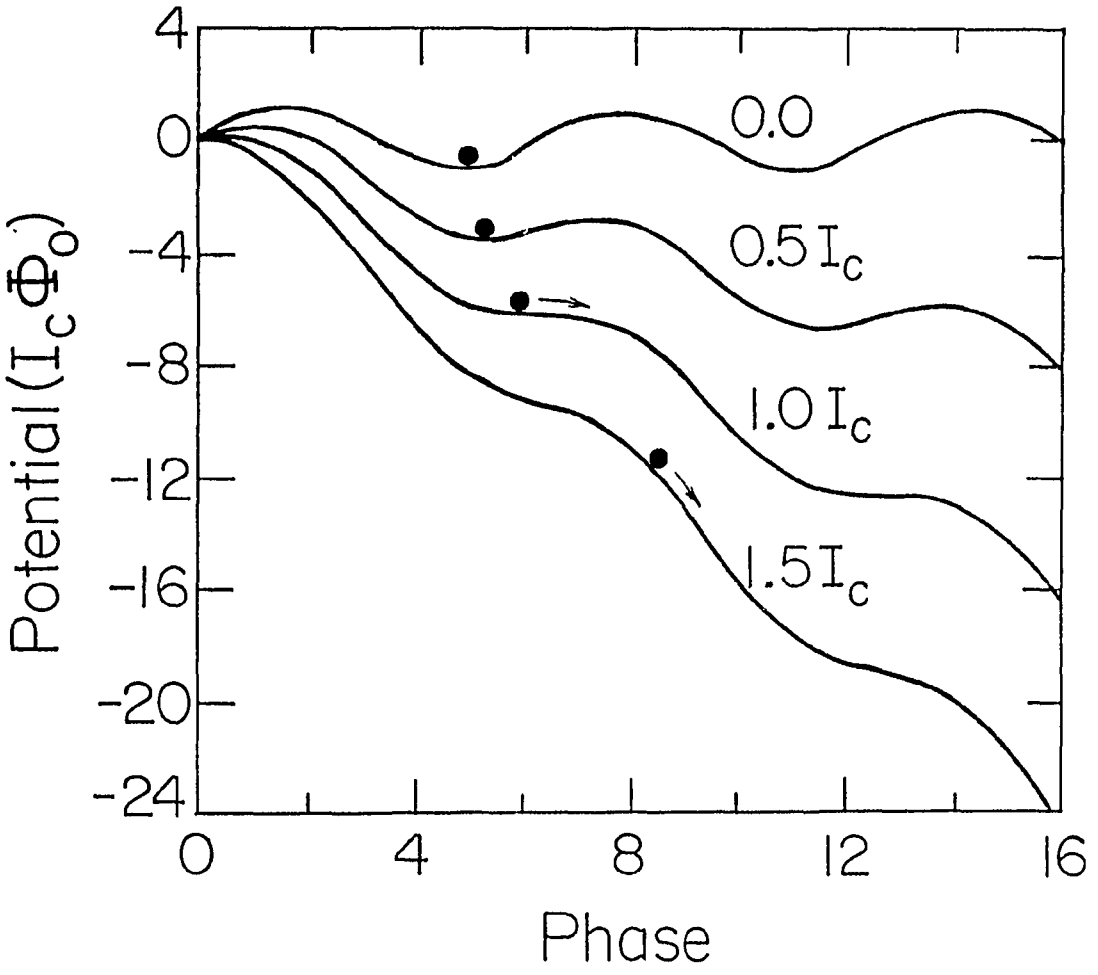

Figure 2.5 - The washboard potential plotted for different values of the bias current.

washboard slope corresponds to the bias current through the junction which is the parameter which can be independently varied. The response of the system is the particle velocity which corresponds to the voltage across the junction. As a simple example of its usefulness, we show how the washboard analog can explain the shape of the I-V characteristic. When the washboard slope is very small, the particle is trapped in one of the wells so that the particle velocity is zero and the junction is in the supercurrent state with $\theta \neq 0$. But as the slope is increased, eventually a critical slope is reached where the wells all disappear and the particle can propagate continuously down the washboard. This corresponds to the transition of the junction out of the zero voltage state as the critical current is exceeded. As the slope (current) is made larger, the mean velocity (voltage) steadily increases . A very important feature of the dynamics are the very high frequency Josephson oscillations (Figure 2.6) which modulate the time averaged voltage and contain frequency components at all harmonics of the fundamental Josephson frequency $\omega_J = 2eV/\hbar$. In the washboard picture, they arise from the corrugation of the washboard potential, while in the junction, they come from ac currents which flow through the shunt resistor due to the ac Josephson effect. Note that in the absence of damping, the washboard dynamics display hysteresis. As the slope is decreased below the critical slope and the wells reappear, the "free-running" particle maintains enough kinetic energy to surmount the hills and continue moving down the washboard. Only when the motion is strongly damped does the particle come to rest as the critical slope is reached.

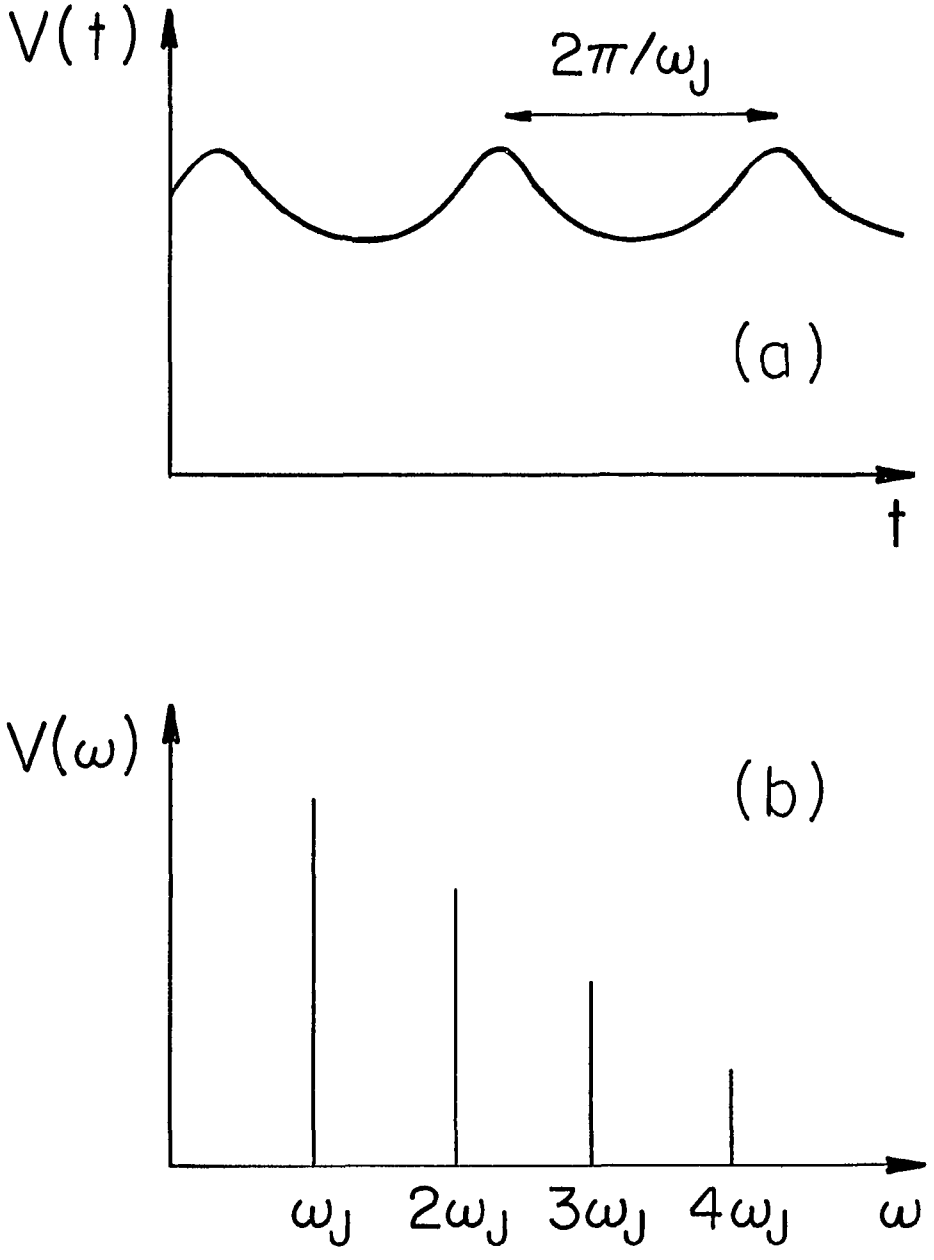

Figure 2.6 - The Josephson oscillations. (a) The instantaneous voltage across the RSJ in the "free-running" state. (b) The Fourier transform of the instantaneous voltage.

2.4 Quantum phase fluctuations

The simplicity of the RSJ model is based upon a number of approximations. In particular, the nonlinear quasiparticle conductance is ignored and the damping is assumed to be independent of frequency. For the overdamped case, where the shunt resistor dominates the normal conductance, these assumptions are reasonable and do not alter the essential correctness of the model.

Of fundamental concern is the implicit assumption that the phase can be treated as a point particle when in fact it is a quantum mechanical operator. It has been demonstrated that the RSJ model fails in the low temperature, weak damping limit for very small area junctions where quantization of the phase is important (Caldeira and Leggett, 1981, Likharev and Zorin, 1985). In fact, the Josephson supercurrent is completely suppressed in the zero capacitance limit. Therefore, the limitations of the RSJ model must first be established before any discussion of the noise properties of small-area junctions can be attempted. This issue has relevance for practical detectors since classical models predict that a reduction in device dimensions leads to improved performance. Despite these concerns, it can be shown that the RSJ model remains valid in the strong damping regime where the quantum phase fluctuations are suppressed by dissipation. This provides some justification for applying the Langevin equation to the overdamped RSJ noise problem as presented in the next section.

In the absence of damping, the Hamiltonian of the unshunted junction in equilibrium (zero current bias) describes the motion of a classical phase particle moving in a periodic potential:

$$H = (e^2/2C)n^2 + I_c\Phi_o\cos\theta \qquad (2.15)$$

$$= \tfrac{1}{2}(\hbar^2 C/2e^2)\dot{\theta} + I_c\Phi_o\cos\theta$$

where

$$n = n_L - n_R = CV/e = (\hbar C/2e^2)\,\dot{\theta} \qquad (2.16)$$

is the number of electrons transferred across the junction. Although the phase and number (velocity of the phase particle) can be specified to arbitrary accuracy in the classical limit, thermal fluctuations are present. When kT is comparable to the amplitude of the Josephson coupling energy, $E_J = I_c\Phi$, the phase particle acquires sufficient thermal energy to activate over the potential barriers separating the wells of the washboard potential (Figure 2.7a). This produces large fluctuations in the phase and number so that the zero voltage state of the junction becomes unobservable.

In addition, quantum uncertainty must also be considered. It can be shown (Anderson, 1967) that the phase and number are quantum mechanical observables subject to the uncertainty relationship

$$(\Delta n)(\Delta\theta) \geq 1 \qquad (2.17)$$

The phase particle should therefore be replaced by a wave packet of width and zero point energy determined by the uncertainty relationship (Figure 2.7b). Treating the phase as a quantum particle, there now exists the possibility that it can propagate into a neighboring well by tunneling through the potential barrier. This process is known as macroscopic

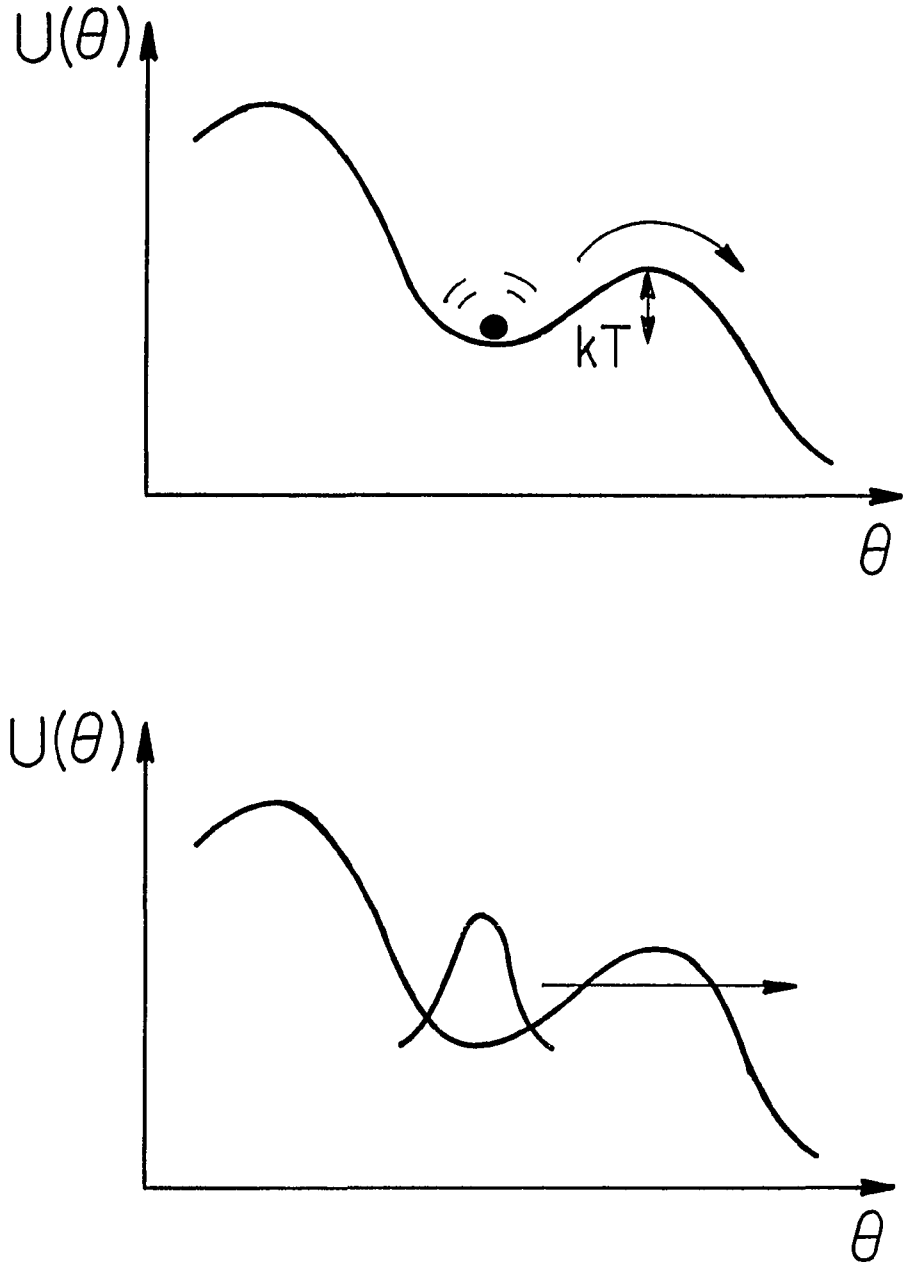

Figure 2.7 - Phase fluctuations in the RSJ model. (a) Thermal activation. (b) Quantum tunneling.

quantum tunneling (MQT) because the phase is a macroscopic variable in the sense that it describes the state of many particles-- all the Cooper pairs have the same phase. In the small capacitance limit where the charging energy e^2/C exceeds the Josephson coupling energy, E_J, the phase becomes delocalized and the expectation value of the Josephson supercurrent vanishes.

We now focus on the importance of damping in suppressing these quantum phase fluctuations. The effect of dissipation on MQT in underdamped junctions has been extensively studied many workers, most notably Caldeira and Leggett (1981). Formally, the problem is to solve for the motion of a junction (more correctly, an ensemble) that is coupled to a heat bath, in this case a resistor, which provides the source of the damping. The total Hamiltonian can be written

$$H = H_{sys} + H_{bath} + H_{int} \tag{2.18}$$

where H_{sys} is the Hamiltonian of the system of interest (the junction), H_{bath} is the Hamiltonian of the heat bath, and H_{int} represents the interaction between the bath and the system which damps the system motion. The heat bath is some complicated object possessing infinitely many degrees of freedom which couple to the system and maintain the temperature of the ensemble at some value T. It can quite generally be modeled as a large collection of oscillators which represent the bath degrees of freedom. The details of the complicated system-bath interaction, H_{int}, are not important for this discussion, but it can be shown that H_{int} leads to the usual damping term in the equation of motion that is proportional to the particle velocity, $d\theta/dt$, and the damping

constant, 1/R. Therefore, phase fluctuations produce dissipation by causing current to flow through the resistor. This provides a classical explanation for the suppression of phase fluctuations by damping. From a quantum point of view, the microscopic system-heat bath interactions responsible for dissipation are said to produce a "watched pot effect" which localizes the phase and collapses the phase wave packet. This localization is similar to what occurs during a measurement process where the system interacts with the measurement apparatus and is forced into a definite eigenstate. In a Josephson junction, the phase wave packet tries to diffuse and leak out of the potential well, but an interaction with the environment can interrupt this diffusion and force the system into a state where it is once again completely localized within the same well. These interactions effectively narrow the width of the phase wave packet, and in the strong damping limit, we regain the phase particle (RSJ) model.

2.5 White noise in the RSJ

Although noise is of great practical importance, many physicists feel that it is very boring. This widely held view has only recently begun to change within the condensed matter physics community. Universal conductance fluctuations, 1/f noise, and the effect of dissipation on macroscopic quantum tunneling are currently very active areas of research. Although this thesis is largely concerned with the effect of noise on device performance, it will be argued here that the fluctuations under study are of fundamental interest in their own right. In particular, these experiments provide a rare test of the quantum

mechanical fluctuation-dissipation theorem. Fluctuation-dissipation lies at the heart of irreversible statistical mechanics and the quantum fluctuations described by this theorem can play an important role in the dynamics of many low temperature quantum systems as well as impose an intrinsic limit on the performance of any practical device.

In the presence of strong damping, the intrinsic phase fluctuations discussed in the last section are dominated by the noise introduced by the damping mechanism (i.e. the shunt resistor). The simplest approach to solving the noise problem is to use the Langevin method where a random noise term (of appropriate spectral density) is added by hand to the equation of motion for the damped system:

$$m(d^2x/dt^2) + \eta(dx/dt) = -(\partial U/\partial x) + F_n \qquad (2.19)$$

where η is the damping constant and F_n is the random fluctuating force. Stated in these terms, this procedure seems rather simplistic and ad hoc. Its justification lies in an examination of the problem from a microscopic point of view. It will be demonstrated that the presence of damping not only requires the existence of this random noise term, but also determines its statistical properties. The starting point for this analysis is again the Hamiltonian (2.18) which describes the coupling of a system to a heat bath possessing many degrees of freedom. Here the system is assumed to be classical. A simple example of this problem is that of a small particle suspended in solution which moves through the liquid in a random, tortuous motion (Brownian motion; see Figure 2.8). The Langevin method attempts to separate the complicated force exerted on the system by the heat bath into two simple parts-- a systematic damping

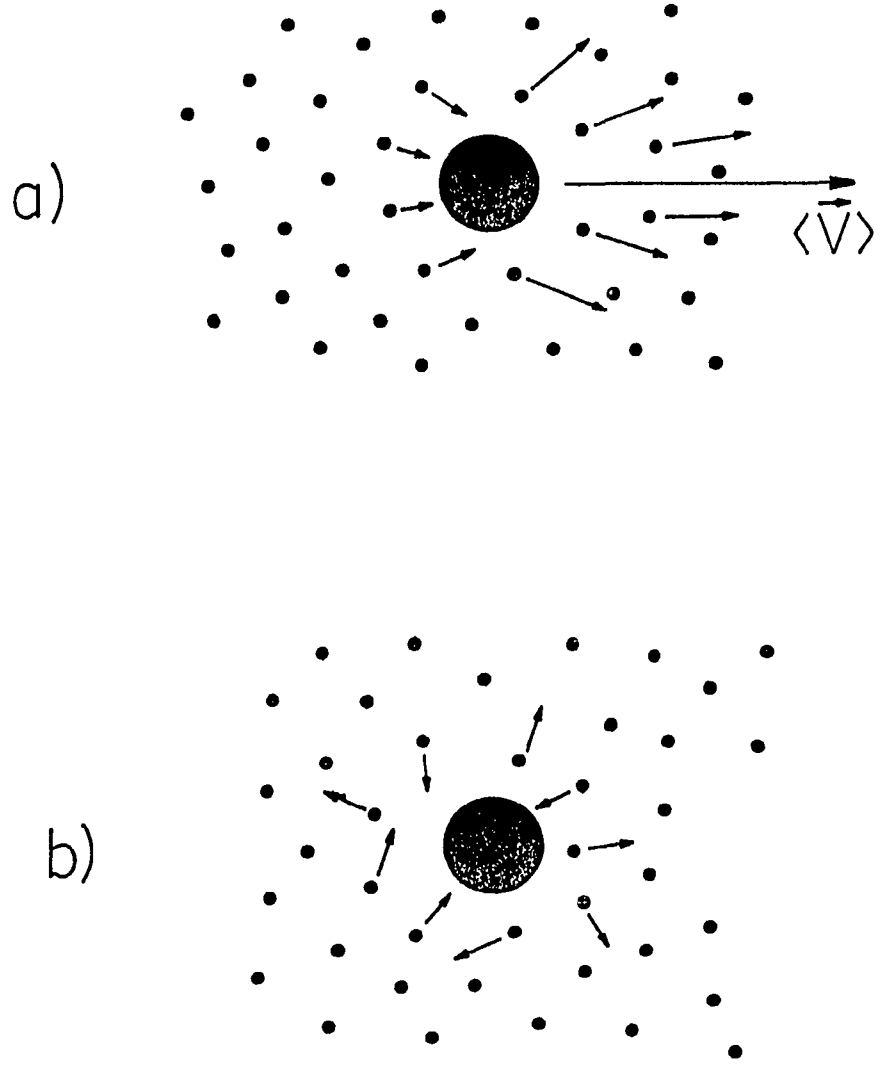

Figure 2.8 - Brownian particle. (a) Motion of particle is damped by dissipation of energy into the bath. (b) In equilibrium, the bath degrees of freedom couple to the particle producing Brownian motion.

term and a randomly fluctuating term that has certain definite statistical properties. The basis for this separation is fluctuation-dissipation. When the system is driven by a coherent external force, the damping exerted by the heat bath is determined by the coupling of the system to the bath degrees of freedom which remove energy from the system (Figure 2.8a). The system-heat bath coupling is described by the damping constant η which is often known. When a driving force is absent (Figure 2.8b), the spontaneous fluctuations exhibited by the system are due to the thermal motion of the bath degrees of freedom coupling energy into the system via the damping mechanism acting in reverse. This is the origin of fluctuation-dissipation which relates the damping constant, η, to the fluctuating force, F_n, exerted on the system by the heat bath, and thereby determines the spectral density of the random noise term appearing in the Langevin equation. Hence, fluctuation-dissipation not only demands the presence of the noise term that is absent from the RSJ model but also determines its statistical properties. This concludes our brief survey of the Langevin method. Further aspects of fluctuation-dissipation will be discussed in the next section where quantum noise effects are examined. An elementary review of these topics can be found in Reif (1965), while a more formal treatment is given by Forster (1975). One final word of caution: despite its success in explaining the noise properties of Josephson devices and many other strongly damped systems, the Langevin method cannot be blindly applied to any situation. Strictly speaking, its use requires rigorous justification, although this is often difficult to obtain. An alternate theoretical technique that deserves

mention involves the Fokker-Planck diffusion equation. This has been successfully applied to the RSJ thermal noise problem (Arai et al., 1982); however, it cannot be easily extended to the quantum case where correlations are present in the noise.

Before reviewing the white noise properties of dc SQUIDs it is instructive to first examine noise effects in single junctions where the results can be more easily understood. The Langevin equation for the RSJ is obtained by adding a random current noise term, I_n, to the equation of motion (2.12). In the washboard picture, current noise causes agitation of the washboard slope which introduces randomness in the motion of the particle. Fluctuations are especially important in a nonlinear system because they can have qualitative effects. For example, the I-V characteristic of the RSJ shows "noise rounding" (Figure 2.9) near V=0 because the phase particle can acquire enough kinetic energy to activate over the potential barrier and into the next well, thus smearing out the sharp transition out of the superconducting state (Ivanchenko et al., 1968, Ambegaokar et al., 1969, Kurkijarvi et al., 1970).

As expected from fluctuation-dissipation, the dominant source of white noise in the RSJ and dc SQUID is the thermal noise of the shunt resistor. Other sources of high frequency fluctuations include 1) chaotic noise due to the nonlinear dynamics of the RSJ, 2) excess noise due to local heating or nonequilibrium effects in the biased shunt resistor or tunnel junction (see Gray, 1981), and 3) shot noise in the quasiparticle tunneling current. These are expected to be negligible for the temperatures and bias conditions used in the SQUID noise measurements. According to Nyquist's theorem, the spectral density of

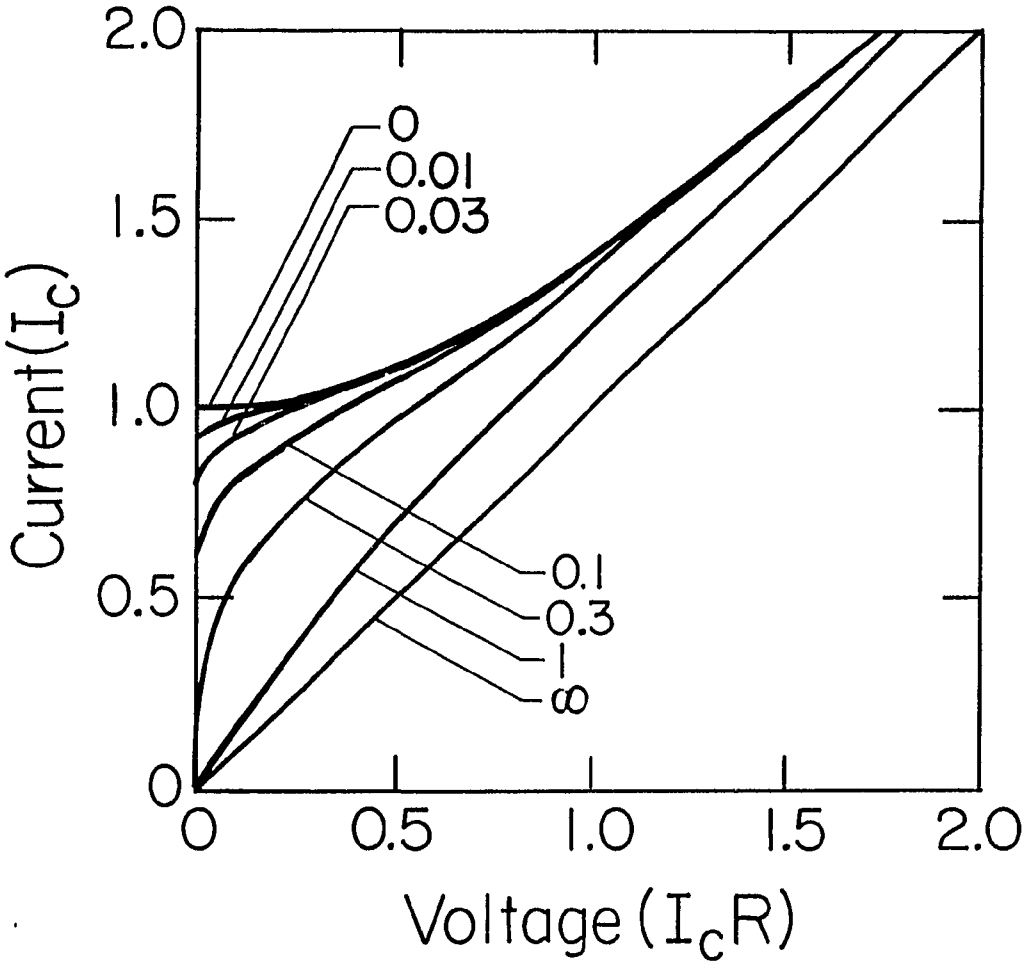

Figure 2.9 - Noise rounding of the I-V characteristic plotted for different values of the thermal noise parameter D= $4\pi ekT/hI$.

thermal noise in a resistor is frequency independent (white) according to

$$S_I(\nu) = \langle I^2(\nu) \rangle = 4kT/R \qquad (2.20)$$

In the zero capacitance limit, the Langevin equation can be solved exactly for the voltage noise (Likharev and Semenov, 1972) :

$$S_V(\nu) = (4kT/R)\ R_D^2[1 + (I/I_c)^2], \qquad (\nu << \nu_J) \qquad (2.21)$$

where $R_D = (\partial V/\partial I)$ is the dynamic or differential resistance. The noise consists of two simple contributions. The first term is just the current noise times the dynamic resistance squared-- the result expected for a linear device. The second term corresponds to noise that gets mixed down from near the Josephson frequency (Figure 2.10). Because of the strong Josephson oscillations and the nonlinear I-V characteristic, some of the white noise near ν_J is mixed down and contributes to the measured noise at much lower frequency. Mixing from higher harmonics is negligible for an ideal RSJ; however, resonance structure, usually associated with stray inductance of the shunt resistor, can produce strong nonlinearities which alter this conclusion. This thermal limit theory has been experimental verified by several groups (Falco et al., 1974, Fulton and Dunkelburger, 1974, Koch et al., 1980).

2.6 Quantum noise effects

When the Josephson frequency is very high, the thermal limit result must be modified to take into account "quantum noise" effects. These are the high frequency fluctuations exhibited by an ordinary thin-film resistor in the quantum noise regime $\hbar\omega/kT > 1$. Physically, the resistor

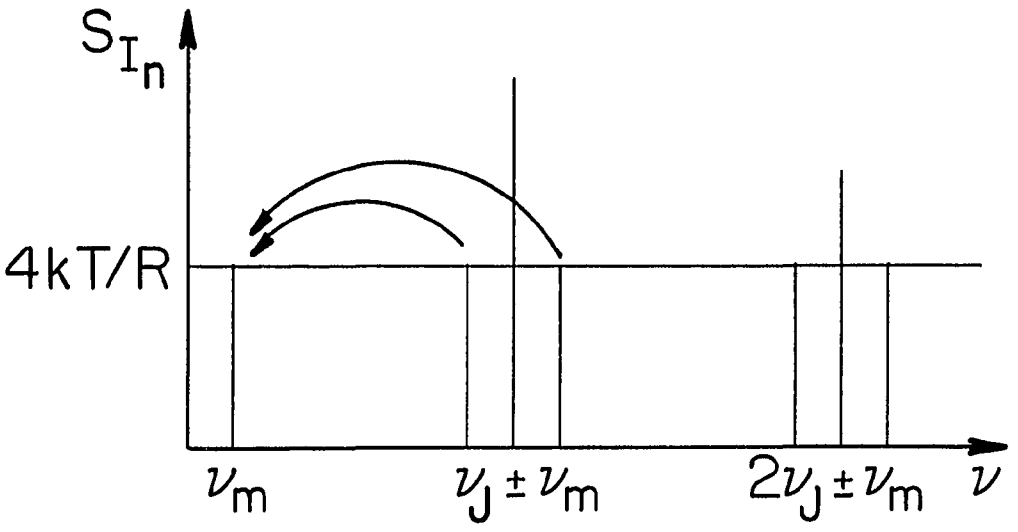

Figure 2.10 - Mixing down of current noise from sidebands of the Josephson frequency in the thermal limit.

noise results from density fluctuations in the conduction electrons. If one examines the resistor at any instant of time, there may be a few more electrons on one side than the other so that a potential difference can be measured between the two ends. Since the conduction electrons form a highly degenerate Fermi gas, these fluctuations will not freeze at zero temperature (as predicted by Nyquist's theorem) since the electrons are still moving very rapidly and randomly at the Fermi velocity. The proper expression for the noise is given by the more general Callen-Welton fluctuation-dissipation theorem (Callen, 1951) which takes into account quantum as well as statistical uncertainty:

$$S_I(\omega) = (4\hbar\omega/R)\left[\frac{1}{2} + \frac{1}{\exp(\hbar\omega/kT)-1}\right] = (2\hbar\omega/R)\coth(\hbar\omega/2kT) \qquad (2.22)$$

Although this result looks rather complicated, it can be obtained from Nyquist's theorem by replacing the thermal energy, $\frac{1}{2}kT$, by the quantum energy

$$\hbar\omega\left[\frac{1}{2} + \frac{1}{\exp(\hbar\omega/kT)-1}\right]$$

At this point, the notion of quantum noise can be somewhat clarified. In a large system possessing many degrees of freedom (e.g. a resistor), the operator for a macroscopic quantity (e.g. the voltage) will not commute with Hamiltonian. Therefore, even at zero temperature, the system has a quantum mechanical probability of being found in different voltage states. "Quantum noise" is defined in the sense that repeated measurement of the voltage will produce a distribution of values governed by quantum mechanical uncertainty.

A better understanding of the fluctuations can be gained by

examining a microscopic picture where the damping mechanism (resistor) is modeled by a large collection of oscillators, i.e an oscillator bath. For a resistor, the oscillators represent modes of electron density fluctuations each having its own characteristic frequency. At high temperatures, the motion of the oscillators is dominated by incoherent thermal fluctuations so that the resistor voltage noise is completely uncorrelated.

$$\langle v(t)v(t')\rangle = \delta(t-t') \qquad (2.23)$$

The power spectrum, given by the Fourier transform of the above autocorrelation function, is therefore frequency independent as given by the Nyquist formula. If we lower the temperature, or alternatively, examine oscillators with larger characteristic frequencies, the oscillators are eventually dominated by coherent zero point fluctuations. The motion is now correlated for times less than a period $2\pi/\omega$. This correlation over very short time scales causes the power spectrum to deviate from the Nyquist result and increase linearly at high frequencies according to (2.22).

To extend the Langevin equation to the quantum regime simply requires the use of a correlated current noise term consistent with the Callen-Welton fluctuation-dissipation theorem. In this case, Koch et.al (1980) derive a slightly different expression for the voltage noise

$$S_V = R_d^2[(4kT/R) + (2eV/R)(I_c/I)^2\coth(eV/kT)], \quad (\nu \ll \nu_J) \qquad (2.24)$$

The first term is the same as before, but the second term is now greater due to the increased current noise at high frequencies (Figure 2.11). In

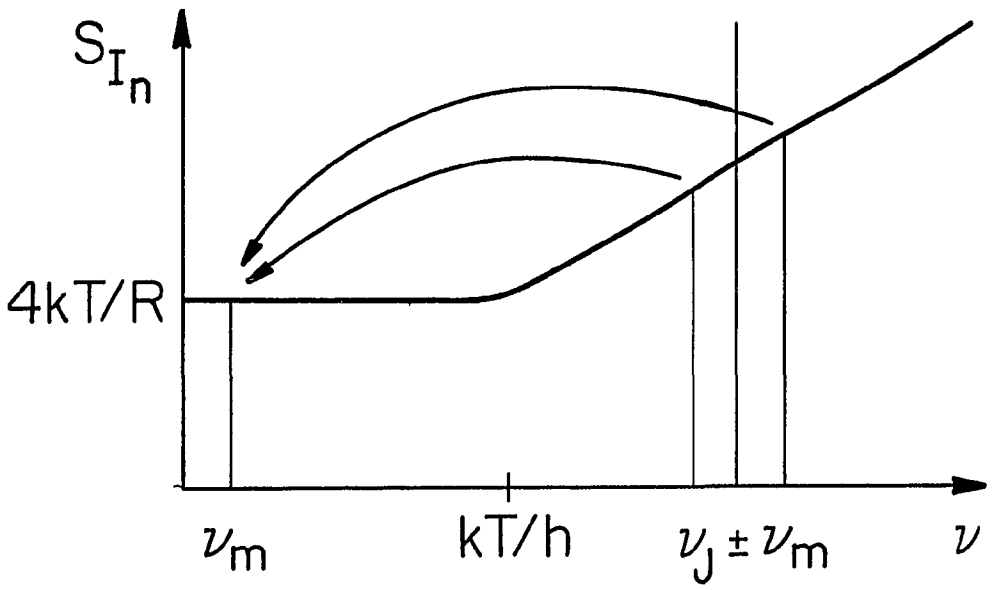

Figure 2.11 - Mixing down of zero point fluctuations from sidebands of the Josephson frequency in the quantum noise regime.

the extreme quantum limit of zero temperature, the white noise disappears and the noise is entirely due to zero point fluctuations. This is the origin of quantum noise effects in the RSJ and dc SQUID, and in fact, these fluctuations will be an intrinsic, limiting source of noise for any electronic device.

The RSJ is an ideal system for studying quantum noise because it combines both high frequency and low temperature operation; however, two conditions must be maintained in order to experimentally observe the effect: 1) the junction must be biased at a voltage large enough to satisfy $2eV = \hbar\omega_J > kT$ so that zero point fluctuations contribute to the mixed down noise and 2) the junction I-V characteristic must be nonlinear at this voltage so that the mixed down noise is large. The first condition is easily met. The second requires that the junctions have large values of I_cR since the junction I-V characteristic is nonlinear only for $V < I_cR$. The Koch simulations show that quantum noise effects are significant in junctions for which

$$\kappa \equiv eI_cR/kT > 1 \tag{2.25}$$

where the critical current and shunt resistance are restricted by the hysteresis condition ($\beta_c < 1$). Substituting this constraint into (2.25) gives

$$\kappa = (e/kT)(\beta_c \Phi_o j_c/2\pi c)^{\frac{1}{2}} \tag{2.26}$$

where j_c is the critical current density and c is the junction capacitance per unit area. Therefore, low temperatures and high critical current densities are required. Recent advances in thin-film technology

have enabled the fabrication of submicron area edge junctions which show distinct advantages for this application. The properties and fabrication of these devices will be discussed in detail in Chapter 3.

2.7 The dc SQUID

The dc SQUID (Superconducting QUantum Interference Device) consists of two RSJs in parallel which form a closed superconducting loop with self-inductance L (Figure 2.12). The dynamics of the SQUID are far more complicated than the RSJ for two reasons: 1) both dc and ac currents (Josephson oscillations) can circulate around the SQUID loop, linking flux through the SQUID and 2) macroscopic phase coherence imposes a flux-dependent constraint on the phase drops across the two junctions. The SQUID equations of motion are fairly straightforward to write down but the solutions (even for zero capacitance) can only be obtained by computer simulation. The reader is referred to the review by Clarke (1977) for details. Instead, it is easiest to understand SQUID operation in terms of an analogy to the Aharonov-Bohm effect. This arises from a phase constraint similar to (2.3) (which leads to flux quantization), but which is appropriately generalized to take into account the added phase drops across the junctions:

$$(e/\hbar c) \oint \mathbf{A}\cdot d\mathbf{l} + \theta_1 - \theta_2 = 2\pi n \qquad (2.27)$$

Since phases are only defined modulo 2π, this becomes

$$\theta_1 - \theta_2 = 2\pi\Phi/\Phi_o \qquad (2.28)$$

This means that the junctions cannot independently adjust their phases to

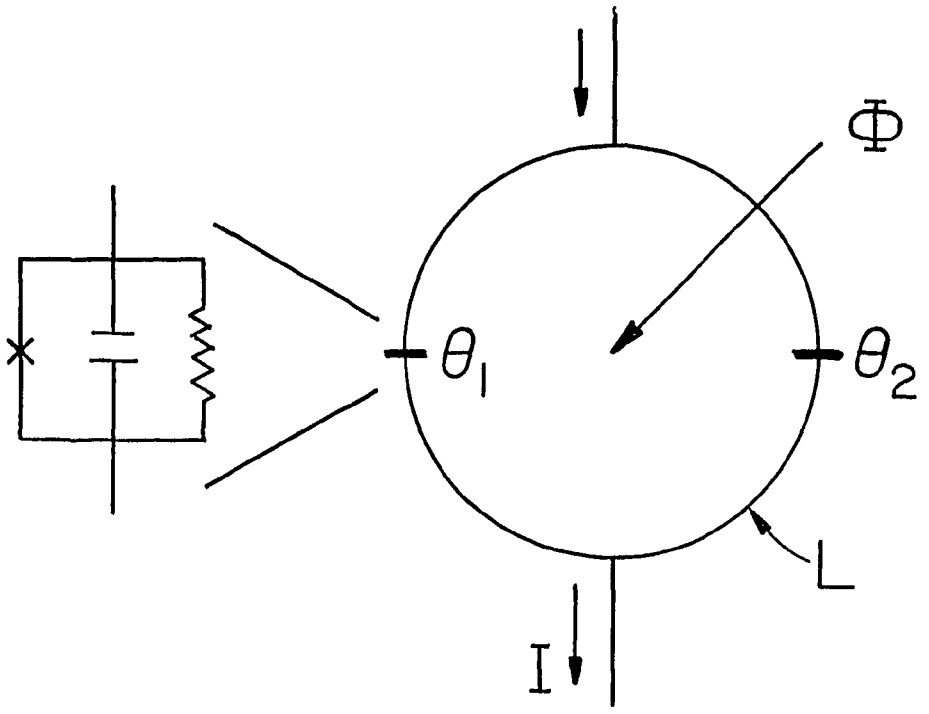

Figure 2.12 - Schematic of the dc SQUID.

give the maximum SQUID critical current, $2I_c$, expected for two parallel junctions; instead, the SQUID critical current, I_c^{SQ}, displays a periodic modulation with applied flux (Figure 2.13a). Inspection of (2.28) shows that this situation is very analogous to the Aharonov-Bohm effect where the amplitude for a particle to arrive at the intersection of two paths depends on the enclosed flux in exactly the same way.

Because of this quantum interference, the SQUID critical current, and therefore, the entire I-V characteristic is strongly modulated by magnetic fields (Figure 2.13b). This effect forms the basis for operating the SQUID as a flux-to-voltage converter. So despite the complex dynamics, the SQUID appears to behave very much like an RSJ whose critical current is a periodic function of the applied flux. In normal operation, a constant bias current is applied to the SQUID so that the measured voltage becomes periodic in the applied flux (Figure 2.14). By varying the bias current, a family of these periodic voltage versus flux (V-Φ) curves can be generated. The flux sensitivity, known as the transfer function, $\partial V/\partial \Phi$, is given by the slope of the V-Φ characteristic. For optimum performance, both the bias current and bias flux are adjusted to give maximum transfer function. The ability to resolve an input flux signal is then limited by the intrinsic voltage fluctuations of the SQUID which are under study here. To achieve a large dynamic range, the V-Φ characteristic should ideally be linear, not periodic. This problem is overcome by operating the SQUID in a flux-locked loop where a feedback flux is applied to the SQUID to keep it precisely at the same operating point. The signal flux is then exactly equal to the feedback flux.

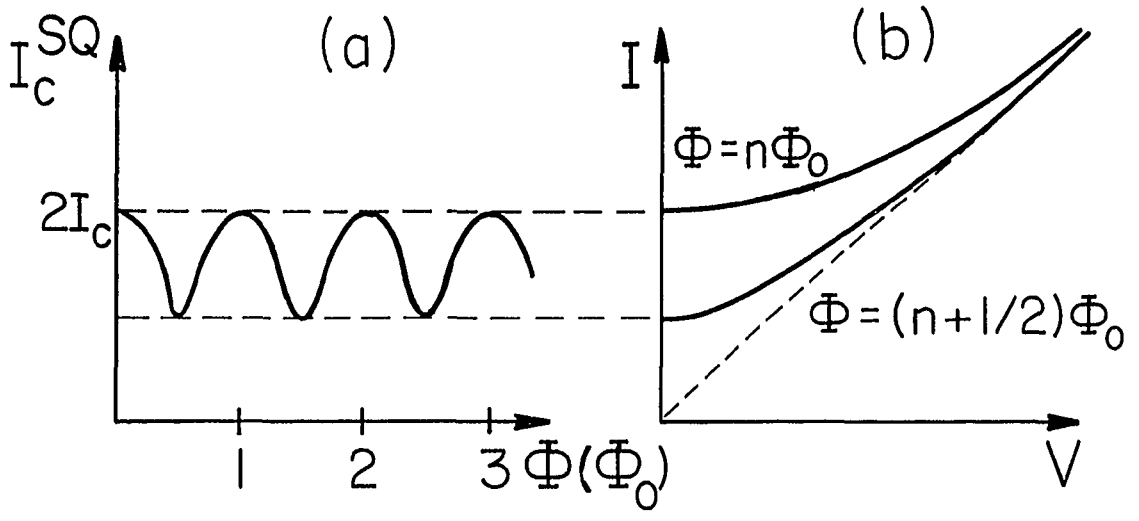

Figure 2.13 - Periodic modulation of (a) SQUID critical current and (b) I-V characteristic with applied flux.

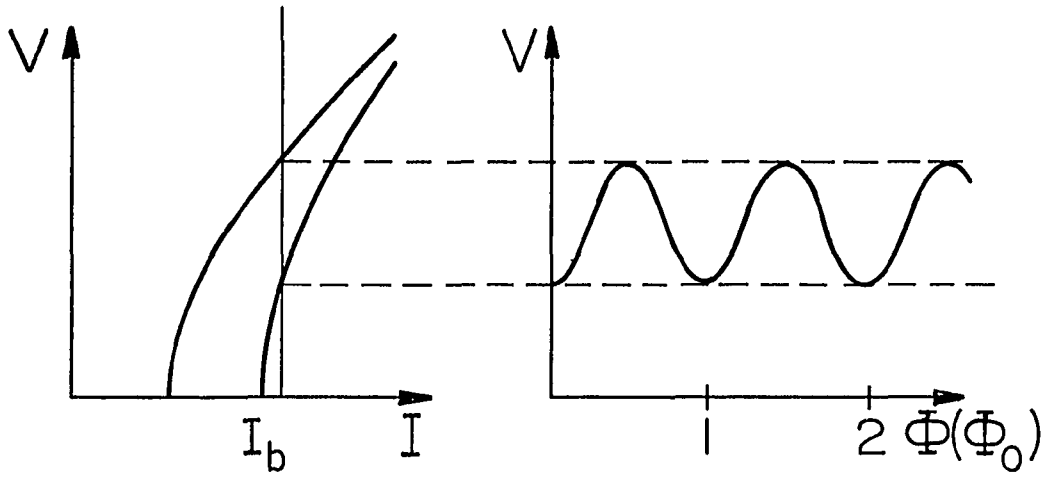

Figure 2.14 - Periodic SQUID voltage versus flux for constant bias current.

2.8 dc SQUID noise

Although quantum noise has been observed in the RSJ (Koch et al., 1981), its effect on the performance of a practical device like the dc SQUID has not yet been measured. Due to the complicated SQUID dynamics, it is not apparent that the behavior of a real device will show good agreement with computer simulations. In particular, the SQUID must be biased at low voltages for these measurements where the nonlinearity is greatest, while the junction measurements of Koch et al. are performed at much higher voltages where the behavior is simpler. Hence, the noise in these two regimes will be sensitive to different aspects of the phase dynamics. In addition, the Koch junctions had rather modest values of κ so that the quantum noise effects were relatively small. It would be interesting to eventually extend their measurement to the far quantum limit where these effects dominate.

The Langevin equations for the dc SQUID is much more complicated than for the a single junction and must be solved on a computer to extract the SQUID voltage noise, S_V. Using the transfer function, this is converted into the equivalent input flux noise

$$S_\Phi = S_V/(\partial V/\partial \Phi)^2 \qquad (2.29)$$

which is the minimum flux signal that can be resolved in the SQUID loop. A more accurate measure of practical performance is the flux energy resolution

$$S_E = \alpha S_\Phi/2L \qquad (2.30)$$

which takes into account the coupling of the SQUID to an input coil where

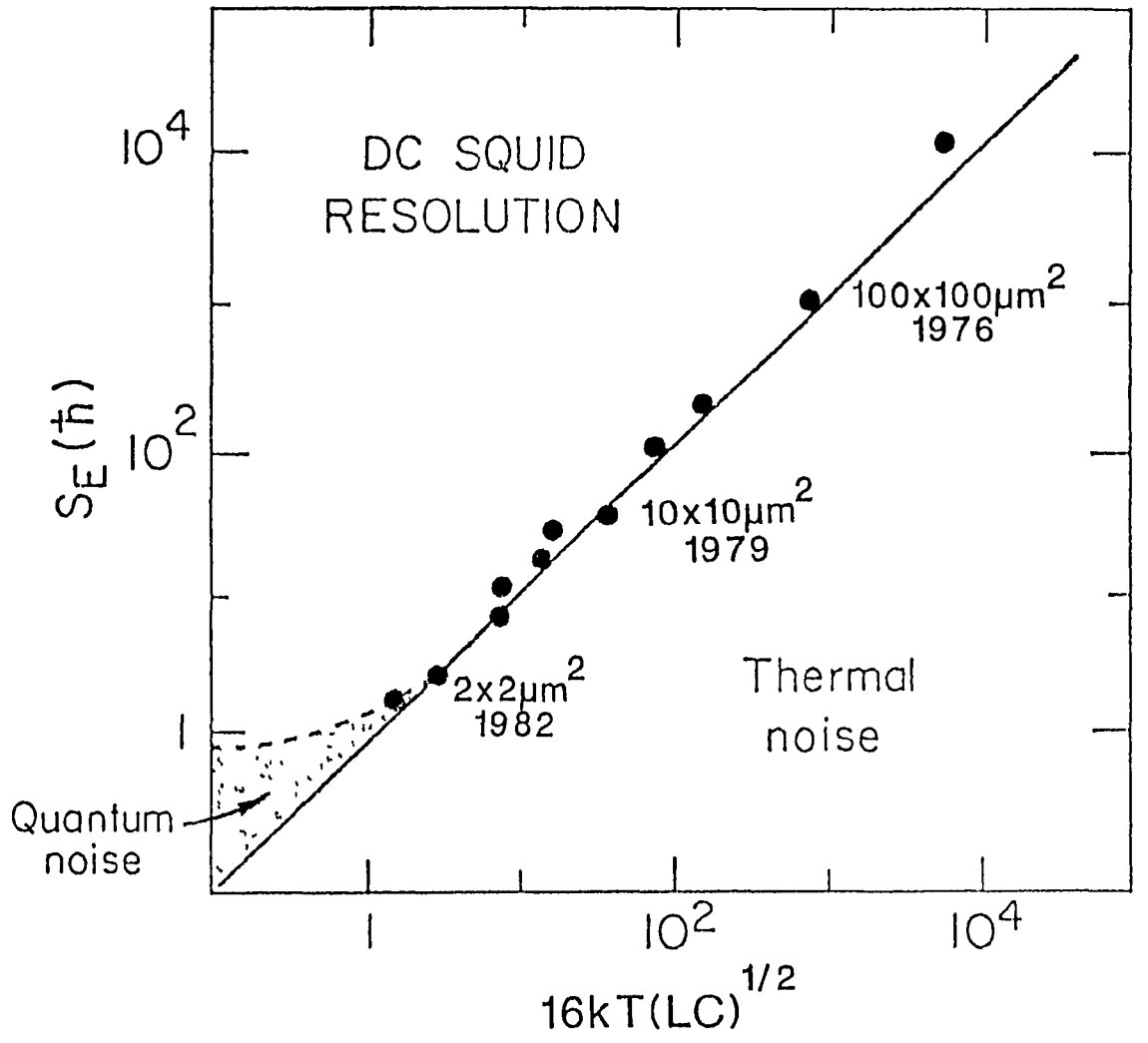

Figure 2.15 - Measured values of SQUID flux energy resolution versus the Tesche-Clarke thermal limit theory. Junction areas and year of publication are indicated for a few SQUIDs. These data are compiled from Clarke et al. (1976), Ketchen and Voss (1979), Voss et al. (1980), Voss et al. (1981), Cromar and Carelli (1981), and Van Harlingen et al. (1981).

α is the coupling efficiency. This is the figure of merit most commonly used for grading and comparing different SQUIDs, and it is the minimum flux energy that can be resolved in the input coil.

In the thermal limit, simulations performed by Tesche and Clarke (1977) find that S_E (α=1) is linear in temperature according to

$$S_E = 16kT(LC)^{\frac{1}{2}} \tag{2.31}$$

This result assumes that the SQUID parameters satisfy the optimization conditions

$$\beta \equiv 2LI_c/\Phi_o = 1 \tag{2.32}$$

and

$$\beta_c \equiv (2\pi/\Phi_o)\ I_c R^2 C = 1 \tag{2.33}$$

Prior to the Tesche-Clarke simulations, the parameter and bias condition dependence of SQUID performance was not well known. Their results served as an important guide for experimental studies and spurred a considerable effort aimed towards achieving the lowest flux energy resolution. Figure 2.15 summarizes the progress in dc SQUID technology. Plotted here are measured values of S_E are plotted versus the thermal limit prediction, (2.31). The data points represent a variety of SQUIDs measured by several different groups and the agreement with theory is clearly quite good. Within five years of the Tesche-Clarke theory, the flux energy resolution had improved by several orders of magnitude and speculation had begun over whether S_E would eventually exhibit a low temperature limit, and if so, at what value. In 1982, Koch, et al. (1981)

demonstrated that zero point fluctuations in the shunt resistors would cause S_E to approach a T=0 value of roughly $\hbar$. According to their simulations, the condition needed to observe quantum noise effects in the SQUID is the same as for the single junction: the SQUIDs must be composed of junctions which satisfy $\kappa>1$. This requirement is consistent with the trend (depicted in Figure 2.15) that much of the improvement in SQUID performance has resulted from the use of progressively smaller Josephson junctions through advances in fabrication technology. The best performance to date was measured by Van Harlingen et al. (1981) in a SQUID composed of $2x2\mu m^2$ junctions. Although this device is thought to be on the verge of the quantum limit of flux energy resolution, they were not able to see the flattening at low temperature which is the characteristic signature of quantum limited performance-- S_E was still decreasing nearly linearly with temperature in agreement with the thermal limit theory.

In principle, the flux energy resolution can be reduced by cooling the SQUID to lower temperatures, but this is not always possible or may be restricted by self-heating. Clearly, it would be desirable to improve the SQUID's intrinsic sensitivity by further optimizing device parameters. Recent advances in thin film technology have enabled the fabrication of ultrasmall-area ($<0.1\mu m^2$) edge junctions which may be ideal for this application. One further advantage of these junctions is that they allow the use of larger loop inductances which helps alleviate the problem of flux coupling to microfabricated SQUIDs. By incorporating edge junctions into a dc SQUID, it now becomes feasible to make a practical detector which can approach quantum-limited performance at

moderate (~1K) temperatures. This possibility provides the motivation for developing high resolution dc SQUIDs and studying their noise white properties as presented in the next two chapters.

Chapter 3

FABRICATION OF ULTRASMALL TUNNEL JUNCTIONS

3.1 Introduction

In large part, the motivation for this study is based on the promising potential of very small-area, high current-density edge junctions for dc SQUID applications. Because these devices are very difficult to make, much of the experimental work is necessarily fabrication intensive. This chapter comprises an introduction to the thin-film techniques which were used to develop a lead-alloy edge junction technology and discusses the advantages and fabrication of these devices. Let the casual reader be warned here that many of the details presented will not be of great interest except, perhaps, to the Josephson junction aficionados among you. But before dismissing the subject, one should recognize that microfabrication has become an invaluable tool in condensed matter physics which has spawned a variety of tailor-made microsystems as well as the ultrasensitive detectors required to probe them. Among the important new phenomena that have been observed are the fractional quantum Hall effect, the Aharonov-Bohm effect in normal metals rings, universal conductance fluctuations, electron localization, and macroscopic quantum tunneling. The trend toward greater reliance on microfabrication will doubtless continue in the future. This chapter provides an overview of this technology and should give the reader some idea of the power of these tools in the hands of a clever experimenter.

3.2 Microfabrication

3.2.1 Introduction

Josephson junction fabrication is an art, not a science. This view is doubtless shared by the vast majority of those who have struggled with the problem. In spite of the impressive "high-technology", many fabrication procedures are established through trial and error, using the results of previous work as a guide. Often, a process developed in one laboratory cannot be reproduced elsewhere or may require considerable modification of process parameters. This results from sensitivity to many factors which the fabricator is unaware of or cannot control. Still, the advantages of microfabrication far outweigh the added problems. With the right combination of patience, experience, and luck, moderately high device yields can be attained.

The requirements for making tunnel junctions include, at a minimum, the ability to deposit thin films and to form high quality tunneling barriers. This can be performed in an ordinary evaporator system using resistive heating to deposit low melting point materials and thermal oxidation to form the tunneling barrier. Although these simple procedures are still commonly used, more sophisticated thin-film processes are often employed to extend the capabilities of device fabrication. Among the techniques most important for this work are resist lithography and ion milling which are described below.

3.2.2 Photolithography

All of the steps in our junction fabrication require photoresist patterning which allows device dimensions to be reduced and accurately

controlled. Resist consists of long polymer chains dissolved in an organic casting solvent. Ultraviolet light or x-rays can be used to expose resist through a photomask in direct contact with the sample. A more sophisticated and versatile exposure method uses a finely focussed electron or ion beam to draw patterns in the resist. For positive photoresist, exposure to UV breaks bonds in the polymer chains. This lower molecular weight material is more soluble in the developer and is therefore selectively removed. For negative resist, the UV crosslinks the polymer chains so that the exposed material has higher molecular weight and is left behind after development. All photoresist processing is done in a microfabrication clean room with filtered yellow lighting to avoid inadvertent exposure. Obviously, another important purpose of a clean room is to provide a very clean, dust-free environment. A well-placed speck of dust can ruin most microcircuits.

The photoresists used for this work are AZ 4110 and Shipley 1450 which have similar properties. The four basic steps involved in photoresist processing are outlined here (see Figure 3.1): 1) a few drops of resist are placed on the substrate which is held by a vacuum chuck and spun (on a spinner) at about 5000 rpm for 30 seconds. This coats the substrate with about a 1μm layer of resist. The thickness can be varied by adjusting the spinning speed or the dilution of the resist. 2) The substrate is then baked at 70C for 20 minutes to drive off the casting solvent. 3) Alignment of the photomask is often a critical step in multilayer circuits. This is performed on an aligner which is essentially a glorified microscope with a mask holder and moveable sample stage. The mask and sample are held at small separation and can be very

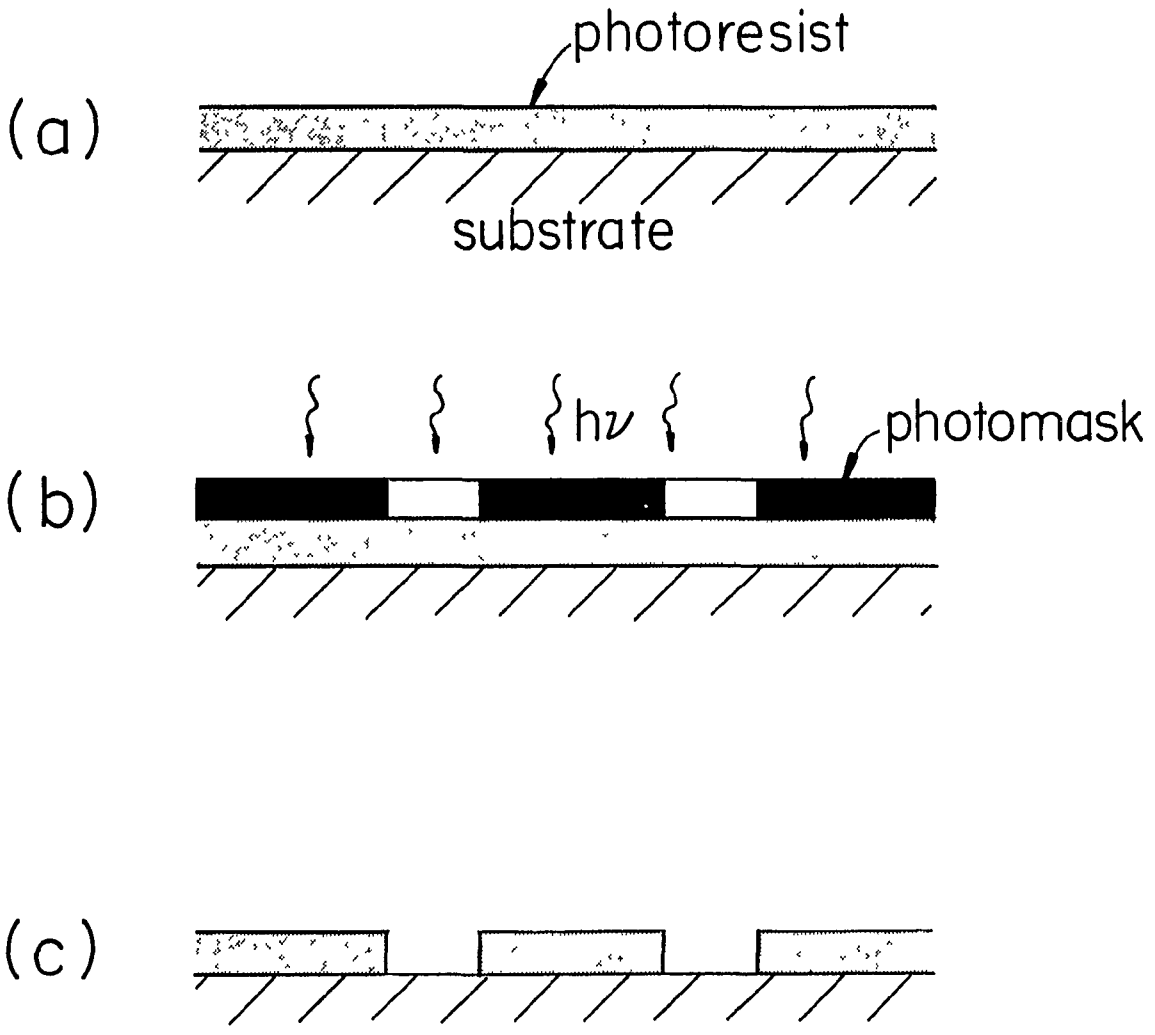

Figure 3.1 - Photoresist processing. (a) Spin on and bake resist. (b) Expose with UV through photomask. (c) Develop exposed areas.

precisely aligned by positioning the sample while viewing through the microscope. They are then brought in contact using mechanical pressure and forced air to push the sample against the mask. The aligner also houses the UV source and optics which expose the resist. A typical exposure time is 30 seconds. 4) In the last step, the substrate is immersed in a dilute developer solution (AZ 400K, Shipley 351) which dissolves away the exposed resist. After rinsing in deionized water, the substrate is blown dry with nitrogen gas and inspected with a high quality optical microscope to ensure that development is complete.

Photoresist patterning is usually followed by deposition and "lift-off" of a thin film, or by etching of existing layers. The resist process outlined above must often modified for each specific application. For instance, the resist walls should ideally be vertical for etching; but for proper lift-off of films, the resist profile must be slightly undercut. This separates the film deposited on the substrate surface from the material deposited on the resist which is to be removed during lift-off (Figure 3.2). Lift-off is achieved by immersing the substrate in acetone which removes the resist and the metal deposited on top of it. To produce an undercut, the substrate is soaked in chlorobenzene (~10 minutes) which penetrates into the resist and removes low molecular weight material. This hardens the surface layer so that it develops more slowly than the resist underneath. To first order, the degree of undercut is controlled by the amount of overdevelopment of the resist beneath the surface; however, it is also sensitive to many process parameters such as resist thickness, chlorobenzene temperature and soak time, developer temperature and strength, and the ambient room

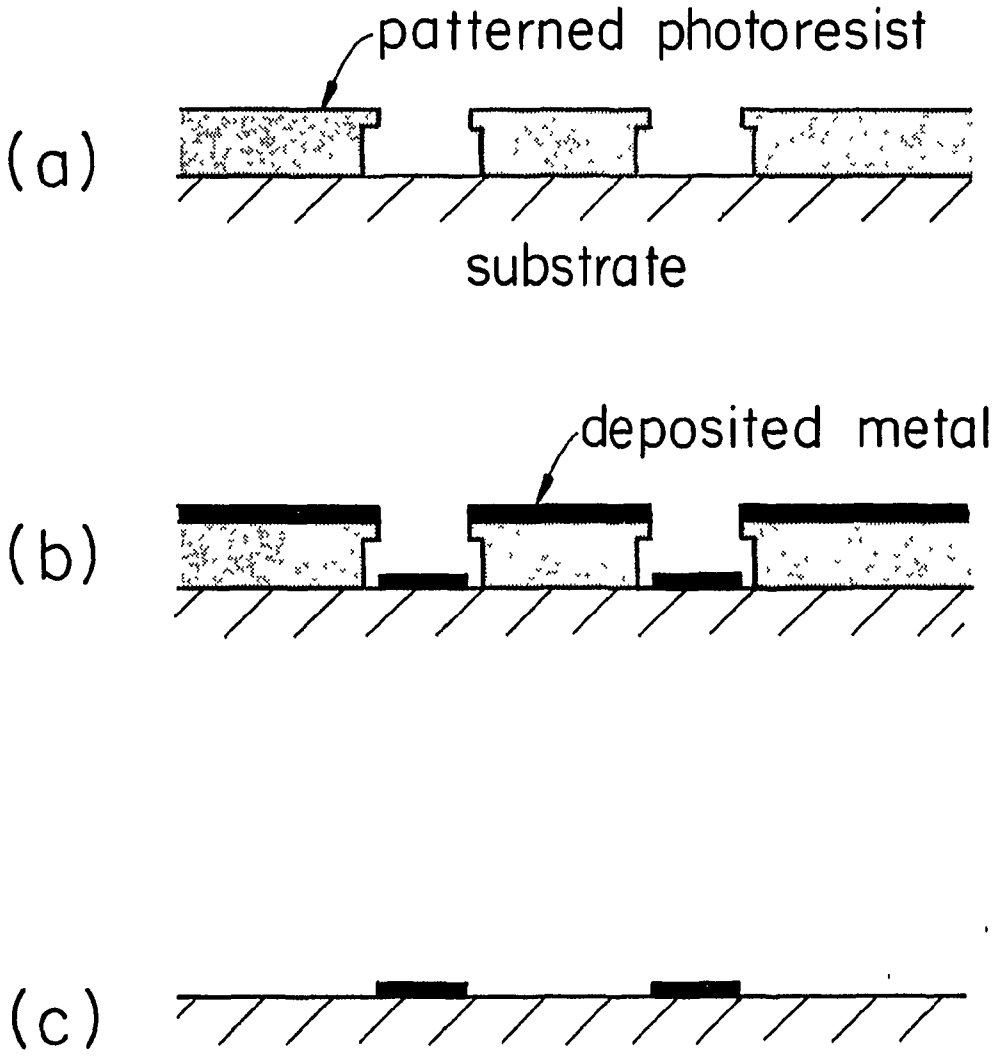

Figure 3.2 - Lift-off of thin film. (a) Undercut resist stencil. (b) Deposition of thin film material. (c) Lift-off of film by removal of resist.

temperature and humidity. The resist profile can only be seen by cleaving the sample and viewing the edge head-on with a scanning electron microscope (SEM); but for most practical purposes, good film lift-off is synonymous with good undercut.

3.2.3 Electron-beam lithography

For some applications, it is desirable to make microstructures as small as possible. The minimum linewidth achievable with conventional UV photolithography is about one micron. Below this, diffraction of the light passing through the photomask becomes a serious problem. A brute force improvement can be achieved by using x-rays; however, this requires extremely good contact between the x-ray mask and substrate, and commercial aligners with x-ray sources are not presently available. Electron-beam lithography is the present state-of-the-art in microfabrication technology. It uses a finely focussed electron beam to draw a pattern in the resist. Electron beams can be focussed to less than 100Å; however, the minimum linewidth achievable using a single layer resist is about 1000Å. The primary limitation is backscattering of electrons from the substrate surface which broadens the exposed region. Multilayer resist systems have been developed to help overcome this problem. The backscattering from the substrate occurs mostly within the lowest resist layer so that the top layer can have very high resolution. Linewidths of less than 200Å have been achieved with this technique (Mankiewich, 1986).

Although most photoresists can be exposed with electrons, e-beam resists, which are made to expose at higher energies, show much better

resolution and contrast. The most widely used e-beam resist is polymethylmethacralate or PMMA. Interestingly, this material is a widely used commercial plastic known as plexiglass. However, e-beam resists must be baked at temperatures above 160C and this often restricts their use. The thin films of many common soft metals (Pb, Bi, Cu) severely oxidize at these temperatures. Since our devices are made of a Pb alloy, AZ 1450J photoresist was used for e-beam exposure. Although the nominal resolution of this resist is stated to be about 0.5μm, linewidths of about 0.2μm were readily achieved. The intrinsic resolution of resist is determined by the length of the broken polymer chains after exposure.

In addition to finer linewidths, e-beam lithography provides a number of important advantages: 1) greater flexibility in device design. Since the beam writing system is computer controlled, pattern changes can be easily implemented in software. This even allows fine tuning of exposure parameters to compensate for variations in individual samples. 2) Precision alignment is usually easier with an e-beam system. The entire substrate can be imaged at low beam current and the writing field can be electronically rotated and shifted to high accuracy. Alignment marks are often used when very accurate pattern registration is required. 3) E-beam systems can generate photomasks starting from commercially available chrome blanks which consist of very flat squares (3"x3") of glass which are coated with chrome (1500Å) and resist. A pattern is exposed and developed in the resist in the usual way and then transferred to the chrome by chemical etching (Figure 3.3). Without this capability it would be necessary to have masks commercially made or to manually cut patterns into rubylith films which are then photographically reduced.

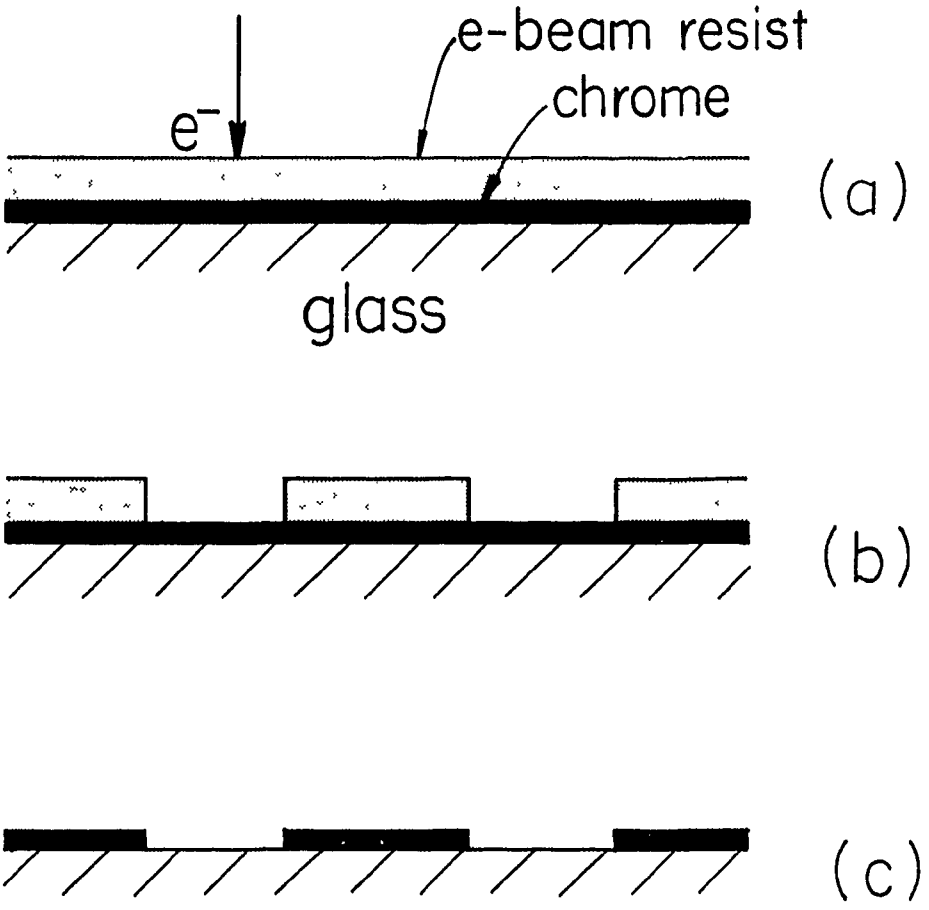

Figure 3.3 - Production of photomask. (a) Electron-beam exposure of chrome blank. (b) Development of resist. (c) Chemical etching of chrome.

3.2.4 Electron-beam lithography system

An electron-beam lithography system was made by building a computer-controlled pattern generator to direct the beam of an ordinary scanning electron microscope (SEM). The outputs (x and y) of the pattern generator plug into an external input of the SEM and override the raster scan used for normal imaging. The beam deflection is simply proportional to the x and y external input voltages. Our patterns are formed by piecing together rectangles and lines. Once the pattern is designed, the following information is entered for each box and stored on disc: 1) the coordinates of the box, 2) the exposure, 3) the direction of the raster (x or y), and 4) the corner in which to begin writing. When the pattern is executed, the computer sends data to the pattern generator which produces a raster to "color in" the boxes according to the specified instructions. The exposure is varied by changing the clock speed which controls the beam writing circuitry. This is very important for drawing small features in order to compensate for proximity effects which cause the actual beam dose to depend on the size of the feature and its proximity to other exposed areas.

The pattern generator hardware consists mostly of binary counters and comparators which produce a digital raster that is converted into an analog voltage using 14 bit digital-to-analog (D/A) converters and op amps to provide gain and offset control. The 14 bit output provides about 16,000 bits of resolution in each direction which is usually more than adequate for all but the most complex applications. The size of the writing field is determined by the SEM magnification setting and the gain controls of the pattern generator. Similarly, the position of the

writing field can be shifted using mechanical and electronic controls of the SEM or the offset adjustment of the pattern generator. The SEM electronic offset and rotate controls are essential for achieving good pattern registration and are accurate to much better than a micron at magnifications greater than 100x.

Typical beam dose for e-beam resist is $10^{-4}C/cm^2$ (C=coulomb). Unlike photoresists, some e-beam resists can be overexposed causing them to become fried onto the substrate. The exposure parameters are less sensitive to the beam voltage and normal imaging voltages (~20keV) can be used. For high resolution (<1μm) patterns, small currents (~25pA) are needed in order to maintain a small spot size. For writing over larger (~1 cm) areas, the beam current is increased to about 1nA to reduce the exposure time. The beam is focussed by imaging the edge of the substrate in order to avoid exposing the resist. Due to the large depth of field and the flatness of the substrates, the sample should remain in good focus over its entire area. The optimum spot size is about one fourth of the minimum feature to be written.

The SEM adapted for use in this work was a JEOL 35C. This instrument was reasonably well suited for our purposes but it has many limitations compared to commercial beam writing machines (costing over a million dollars) which can draw over very large field sizes (~$1cm^2$) with an absolute accuracy of about half a micron over the entire area. Some even have the capability to very precisely move the sample stage so that many fields can be stitched together with little loss of accuracy. Ordinary SEMs are made to scan over much smaller distances and suffer from a number of problems which cause distortions when large field sizes

are used. Chief among these are increased nonlinearity and a precipitous falloff in the beam current at large deflections. In addition, hysteresis in the magnetic deflection coils can also occur when the beam is forced to jump even moderately large (~100μm) distances. On the plus side, ordinary SEMs have smaller spot sizes (<100Å) than commercial beam writing machines and are therefore capable of achieving finer linewidths. Commercial beam writing machines compromise on spot size to obtain larger beam currents which allows faster device throughput. Although our homemade e-beam writing system is not well suited for making large, complex circuits, it is perfectly adequate for drawing the simple, but extremely fine patterns required for this work.

3.2.4 Ion beam techniques

The ion mill is now recognized as an indispensible component of the microfabrication laboratory. It produces a nearly uniform, monoenergetic ion beam which can be used for many purposes: 1) ion beam cleaning of substrates is performed prior to oxidation and deposition to insure that the sample surface is free of residues which can interfere with oxide growth or film adhesion, 2) ion beam etching has the advantage of being anisotropic (as opposed to chemical etches) which makes it useful for patterning very small features. In the presence of the proper reactive gases, it can selectively etch specific materials, 3) nearly any material can be deposited by ion beam sputtering and the resulting films often have superior mechanical properties, and 4) reactive ion-beam oxidation has shown promise as a technique for growing tunneling barriers for high current-density junctions (Kleinsasser, 1980). A review of this

technology has been written by Vossen and Kern (1977).

The body of the ion mill (Figure 3.4) is electrically insulated from its housing which is mounted to a vacuum system. Inside the body is a cylindrical anode with a tungsten filament cathode located at its center. Argon (at 10^{-4}torr) is introduced into this region and electrons are emitted from the filament by resistive heating. A bias (~50V) applied between the cathode and anode causes the electrons to accelerate towards the anode and collide with argon atoms along the way, producing a gaseous discharge. By applying a voltage (beam voltage) to the body, the discharge is created at a large potential with respect to ground so that ions leaving the mill acquire kinetic energy equal to the beam voltage as they accelerate towards the target. Two precisely aligned grids control the extraction of the ions from the discharge region. The screen grid is connected to the body and helps confine the discharge. The accelerating grid is biased to extract any ions which wander nearby. For most applications, the beam is neutralized by resistively heating a filament located in the beam path. This is particularly recommended when milling insulators, although the material sputtered from the neutralizer filament is a potential source of contamination. Maximum beam voltages and current densities achievable with our mill (Ion Tech- 2.5cm) are 2000V and 10mA/cm^2 over a one inch diameter area; typical parameters used for most of this work are about 500V and 250μA/cm^2.

The mill is incorporated into an ordinary evaporator system which has fixturing that enables samples to be positioned below the ion mill and then rotated above the evaporation boats. In addition, a water

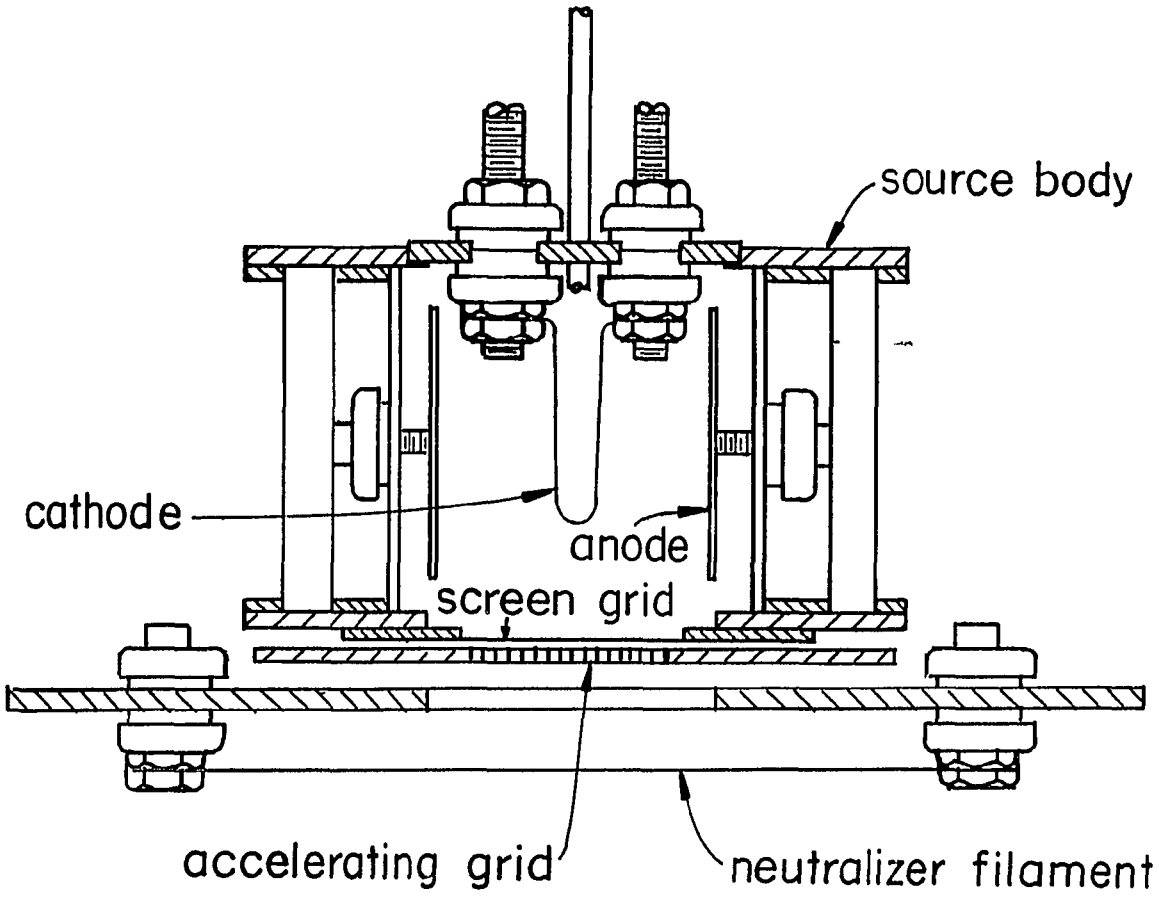

Figure 3.4 - Ion mill (Ion Tech- 2.5cm).

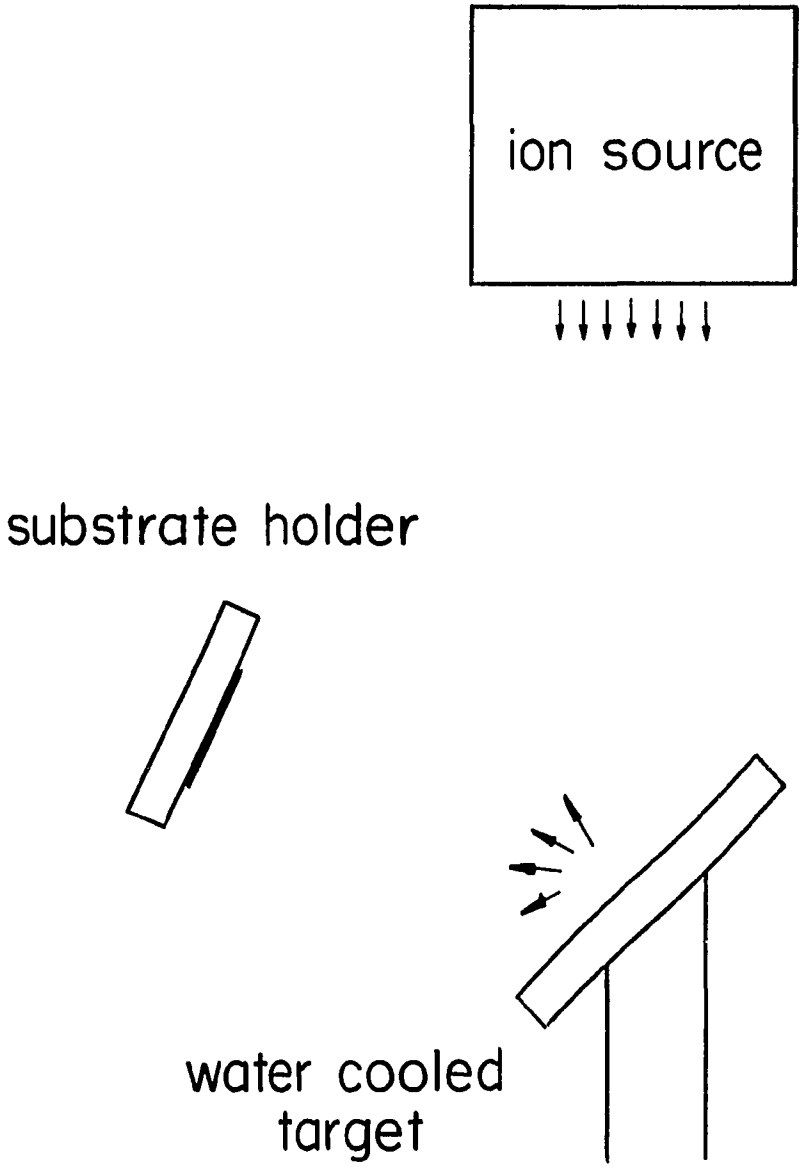

Figure 3.5 - Ion beam deposition.

cooled substrate holder is located directly below the mill for etching at large beam voltages and currents. Soft metal films and photoresist often deteriorate if no water cooling is used. The angle of the substrate holder can be adjusted to produce films with sloped edges as required for edge junction fabrication. Ion beam deposition can also be implemented with this setup by placing the target material on the substrate holder and positioning the sample in the path of sputtered atoms (Figure 3.5).

3.3 Tunnel junction materials

The material properties of the superconductors influence almost every aspect of the fabrication process. Perhaps the most fundamental property (at least from a theoretical standpoint) is the transition temperature, T_c. Since the electrodes of the junction must be superconducting, the T_c of any practical device should be at least 4.2K. The T_c also determines the important parameter I_cR_j which has the simple zero temperature form,

$$I_cR_j = (\pi/2)\ \Delta(0) \sim T_c \qquad (3.1)$$

where $\Delta(0)$ is the T=0 energy gap and R_j is the ohmic tunneling resistance of the junction when the electrodes are in the normal state. This relationship provides a simple understanding of the magnitude of the Josephson critical current, I_c: it is proportional to the amplitude of the superconducting order parameter, Δ, and it is inversely proportional to R_j which governs the coupling between the superconductors. Therefore, the Josephson critical current is essentially a measure of the superconductive coupling strength between the electrodes. In a simple rectangular barrier approximation, the tunneling conductance per area, g,

and therefore the critical current density, j_c, depend on the tunneling barrier height, U, and thickness, d, according to

$$g \sim j_c \sim \exp -[2(mU)^{\frac{1}{2}}d/\hbar] \qquad (3.2)$$

So for given electrode and barrier materials, the critical current density is controlled by varying the barrier thickness. In many applications, $\Delta(0)$ or I_cR_j determine the device characteristics in a fundamental way; however, if resistively shunted junctions are used, the important parameter becomes I_cR where the shunt resistance, R, is restricted by the hysteresis condition. But even in this case, I_cR_j sets an upper limit on the value of I_cR; therefore, large I_cR_j (i.e. high T_c) materials are still required to obtain high sensitivity.

In addition to T_c, the selection of starting materials is influenced by several more practical considerations: 1) the ease with which the material can be deposited, 2) the mechanical properties of the resulting thin films, 3) its resilience to the moderately high temperatures encountered during fabrication and to the very low temperatures required for operation, and most important of all 4) its ability to form a stable, uniform oxide to serve as a tunneling barrier. Of all the superconductors with moderately high T_c, only Pb (T_c= 7.2K) based or Nb (T_c=9.2K) based alloys satisfy the criteria listed above. Other, more exotic, high T_c compounds (Chevrel phase, A-15 compounds) have shown poor mechanical properties or are difficult to make into thin films. However, in the last few months, a new class of spectacularly high T_c (>90K) superconductors has appeared. Thin films have been made by several groups and IBM has even announced the fabrication of a rather

crude 68K thin-film dc SQUID. At these temperatures, thermal noise is likely to severely degrade the performance and it is not known how the device will compare to conventional SQUIDs at lower temperatures; but the overall outlook for commercial applications of this new technology is very promising to say the least.

The key to fabricating high quality Josephson junctions lies in forming a thin (~20Å), uniform tunneling barrier. The barrier characteristics (barrier height and thickness) must conform to very narrow tolerances in order to give the desired critical current density; and for practical devices, they must remain stable over long periods of time and withstand frequent thermal cycling. Most tunneling barriers consist of the native oxide of the base electrode metal. Although their growth can be influenced by oxidation conditions (oxygen partial pressure and temperature), the native oxides of most superconductors are too thick or unstable for the high current densities required in this work. Recently, much work has been devoted to making artificial barriers whose properties are ideally independent of the base electrode material. This is accomplished by depositing a very thin insulator or a thin metal which is then oxidized. Unfortunately, these barriers tend to exhibit large amounts of subgap ($V<2\Delta/e$) leakage currents when they are made very thin.

The vast majority of superconductor devices are made using Pb alloy or Nb films. They have high T_c, good tunneling characteristics and exhibit wide range of current densities for different oxidation methods. Nb devices are very rugged but are generally more difficult to make than Pb devices. Much of this fabrication technology was developed at IBM for use in large scale superconducting integrated circuits in an effort to

make a superconducting computer. Although their junctions were designed for moderate current density applications ($<10^4 A/cm^2$), many of the techniques developed by the IBM group (Greiner et al., 1980) were adopted with some modification to fabricate the high current-density edge junctions used in this work.

The devices reported in this work were all made of Pb alloy. Josephson junctions made of pure Pb films have long been used to study superconductive tunneling. They are fairly simple to make because Pb is easy to evaporate, its T_c is insensitive to impurities in the film, and it can be thermally oxidized (exposed to an oxygen atmosphere) to form high quality tunnelling barriers. However, Pb is a poor material for making practical devices because the films readily deteriorate during photoresist processing and they cannot withstand frequent thermal cycling. These problems are overcome by alloying Pb with indium (In) and gold (Au) to produce more stable, homogeneous films. Some of the indium migrates to the surface and forms a protective indium oxide coating so that photoresist processing can be used. In addition, the tunneling barrier of these junctions is composed of indium oxide which has excellent properties for high resolution SQUID applications: 1) very large critical current densities ($>10^5 A/cm^2$) can be achieved and 2) the specific capacitance of the junctions is very low (three times smaller than for Nb_2O_5 barriers, Greiner et al., 1980). Although rugged Nb junctions may be preferable for practical devices, Pb alloy technology yields very high quality, low capacitance junctions with relative ease which is especially advantageous for this work where the lithography is so demanding.

3.4 Edge junctions

The flux sensitivity and frequency response of a dc SQUID improve by using smaller junction areas. The size of conventional overlap junctions, formed by the simple overlap of two metal films, is restricted by the minimum linewidth achievable (~1μm) using lithography; however, a factor of ten improvement can be obtained by using a clever, yet simple technique to fabricate edge junctions (Figure 3.6). These are made (see section 3.5) by insulating the top surface of the base electrode film and leaving only the edge exposed to form the junction. Therefore, the thickness of the film, which can be made very small (<1000Å), becomes one of the junction dimensions. The other dimension is determined by the counterelectrode linewidth which can be patterned using electron-beam lithography. Areas of 0.01-0.10μm^2 are readily achieved. In addition, small area junctions allow the use of larger SQUID self-inductances and shunt resistances (β_c<1) which facilitates efficient flux coupling to an input coil and reduces self heating of the shunt.

As outlined in sections 2.6 and 2.8, quantum-limited SQUID performance requires low temperatures and junctions that have large critical current densities. In practice, nonequilibrium effects and excess leakage currents limit the current density, while self-heating of the shunt resistor or the junction itself restricts the minimum operating temperature. Conventional overlap junctions (formed by a simple overlap of two films) are particularly susceptible to these problems. Their electrodes are easily driven out equilibrium (Figure 3.7a) because the excess quasiparticles injected into the films cannot easily escape from

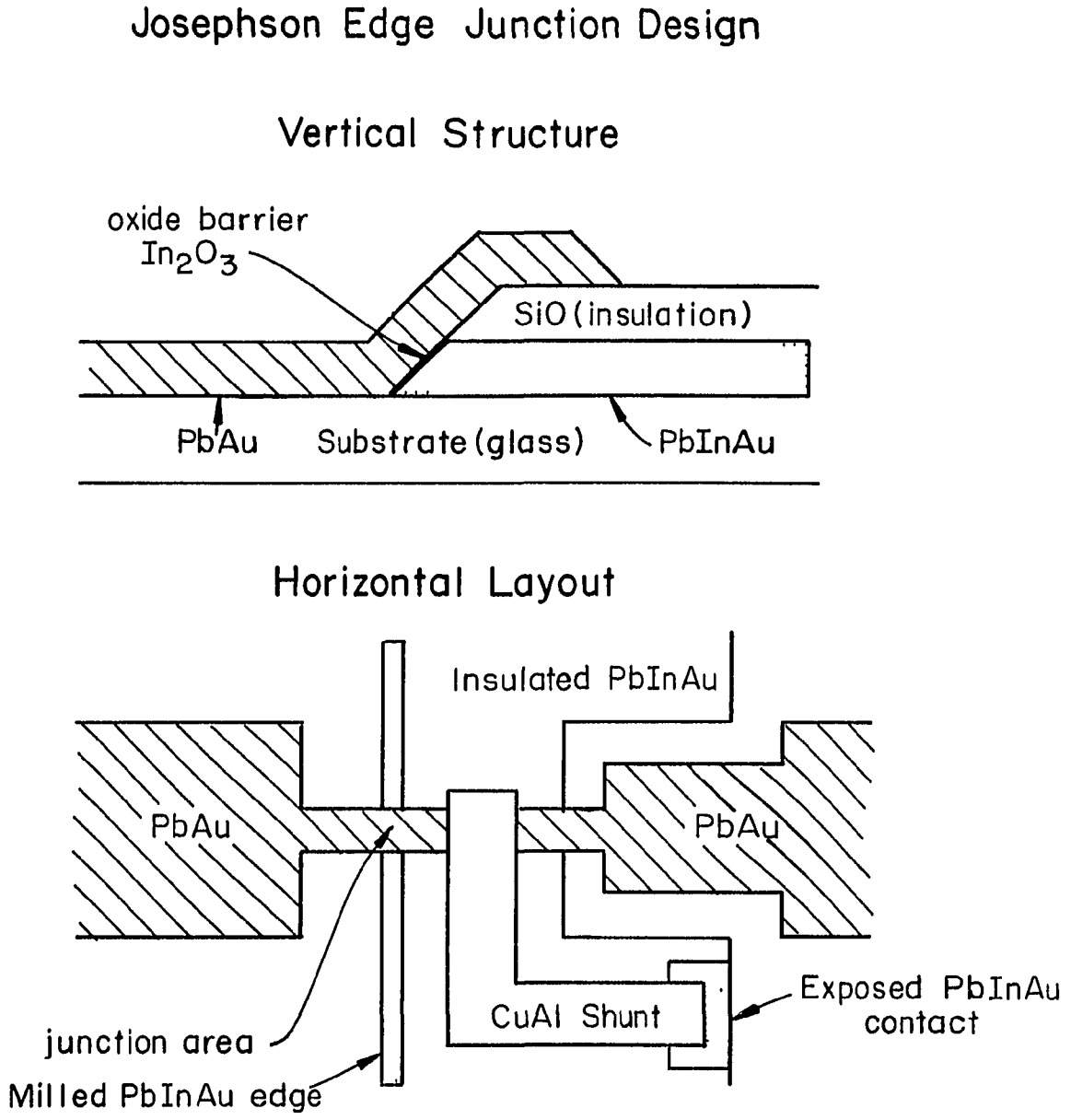

Figure 3.6 - Schematic of edge junction.

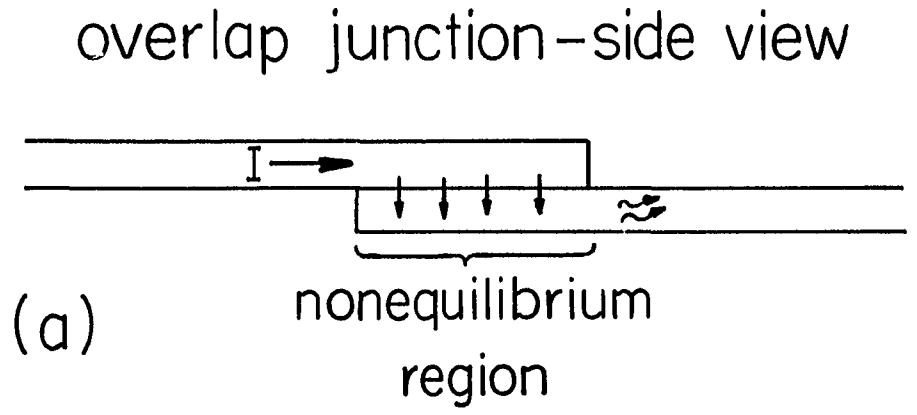

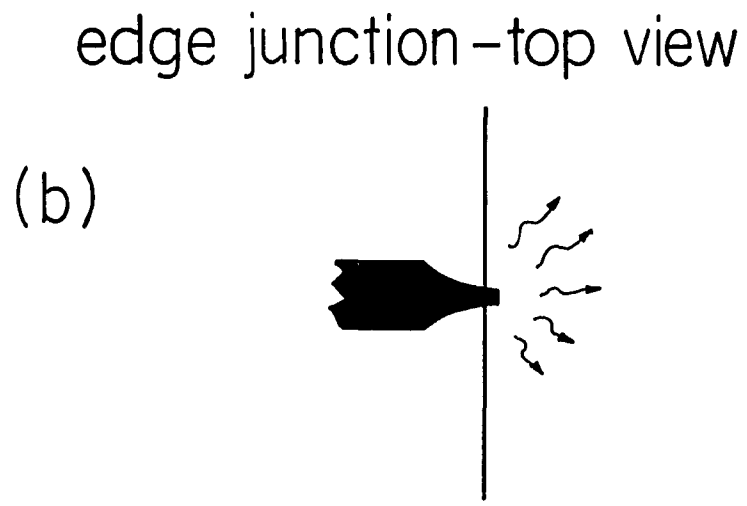

Figure 3.7 - (a) Side view of overlap junction showing nonequilibrium region caused by quasiparticle injection. (b) Top view of edge junction showing escape of heat and quasiparticles into base electrode.

the region near the junction. In contrast, small-area edge junctions have an ideal geometry which provides "two-dimensional cooling" by allowing heat and excess quasiparticles near the junction area to spread out into the base electrode (Figure 3.7b). Although heating and nonequilibrium effects are less severe for resistively-shunted devices like the SQUID, which are biased at low voltage, they become very important for the unshunted junctions studied in chapter 6. The fabrication process developed for making edge junctions is outlined below.

3.5 Edge junction fabrication

Edge junction fabrication (Figure 3.6 and 3.8) requires five processing steps which are each preceded by photoresist patterning: 1) Pb, In(15%), and Au(3%) are evaporated separately to form a 870Å base electrode layer. The metals easily interdiffuse at room temperature to form a homogeneous film containing small grains of AuIn which help stabilize the film. 2) The base electrode is partially covered with a 1400Å layer of evaporated SiO which serves as the ion-milling mask for defining the edge along which the junction is formed. The lithography for this step must be performed with care so that the edge will be very smooth on a one micron scale. 3) A layer of photoresist with a small window opening is used to expose only the edge to the ion beam. The base electrode is etched at a small (10 degree) angle on a water cooled substrate holder using a neutralized Ar^+ beam. Typical beam parameters are 500V, 450A/cm^2. 4) Resistive shunts of CuAl(5%) are evaporated. A thickness of 700Å gives the desired resistivity of about one ohm per

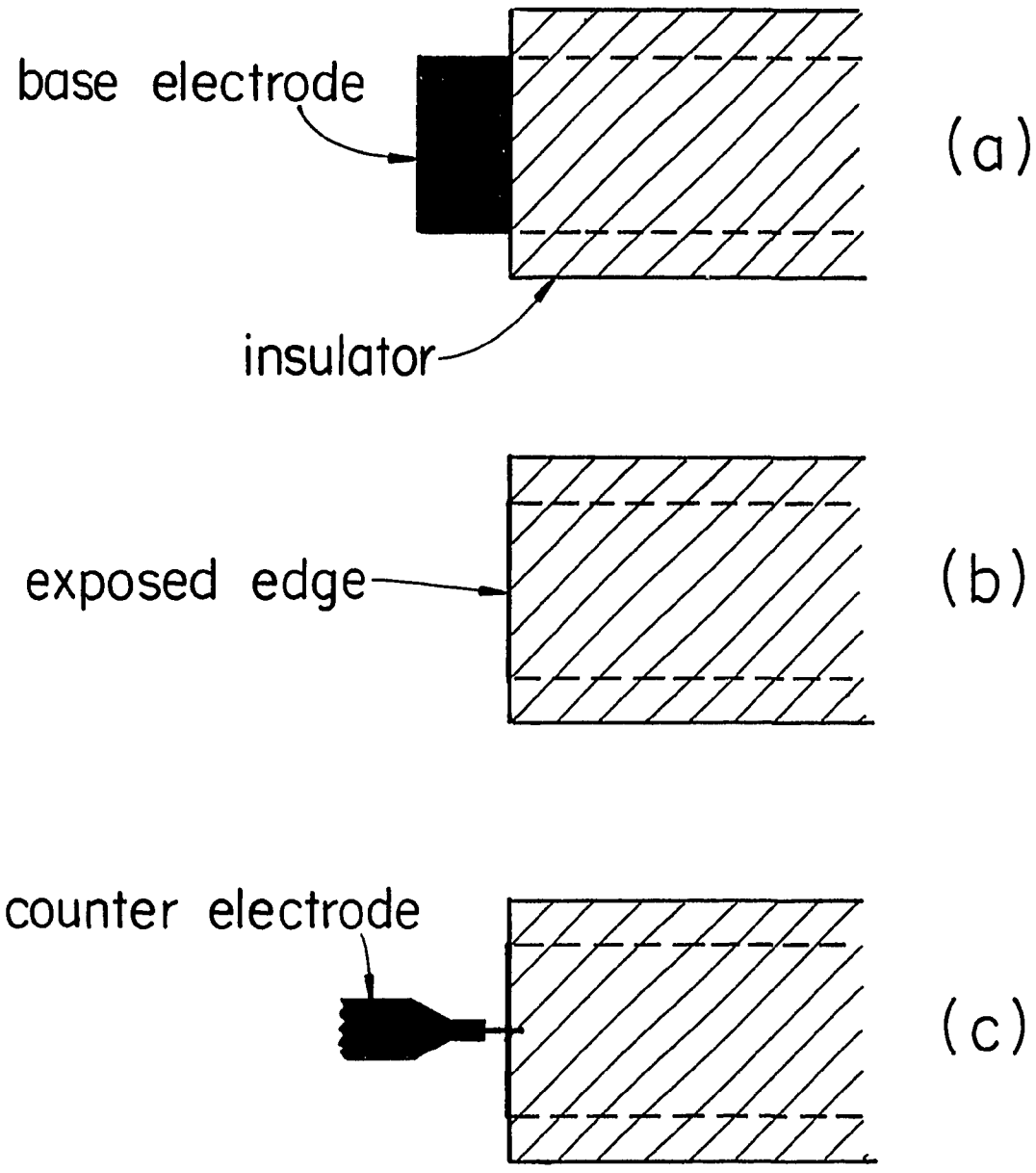

Figure 3.8 - Edge junction fabrication. (a) Base electrode is partially covered by an insulator. (b) An ion beam etches the unprotected base electrode. (c) The counterelectrode is deposited following formation of the tunneling barrier.

square. 5) Using electron-beam lithography, the counterelectrode is patterned with minimum line widths of 0.5-1.2μm. The base electrode is cleaned with the ion mill for 45 seconds at 300V, 250μA/cm^2 and then the tunneling barrier is grown by thermally oxidation at room temperature for 1-5 minutes in an oxygen atmosphere of 100-500μ. It should be cautioned that the contact to the copper shunt resistor also oxidizes during this process which can possibly produce an additional contact resistance. The device is completed by depositing a 3500Å counterelectrode film of Pb or PbAu(3%). The incorporation of edge junctions into a SQUID design is discussed in the next chapter.

Chapter 4

QUANTUM NOISE EFFECTS IN DC SQUIDS

4.1 Introduction

This chapter details the experimental aspects of dc SQUID noise measurement. The first section presents a discussion of SQUID design considerations, followed by a summary of device fabrication and characterization. The electronics and experimental techniques required for low-level noise measurements are then described. Our SQUIDs exhibit excellent signal properties and extremely high flux sensitivity. Their noise performance is in reasonable agreement with computer simulations and one device displays a flux energy resolution of $1.6\pm.5\hbar$, the lowest value yet reported; however, lower temperatures are still needed to conclusively demonstrate quantum-limited performance. The chapter concludes with some comments on fundamental limitations of edge junction technology and the outlook for practical detector applications.

4.2 dc SQUID design

The starting point for designing a quantum-limited SQUID is to determine the smallest junction area and the largest current density attainable in order to maximize the quantum noise parameter κ as discussed in section 2.6. In practice, minimum junction areas are largely determined by microlithography capabilities, while the critical current density is restricted by nonequilibrium effects and excess leakage currents as discussed above. An added consideration is the difficulty in reproducibly fabricating junctions with sufficient yield

and quality as device dimensions are reduced and critical current densities are increased. Using e-beam lithography and an edge junction geometry, we can reliably fabricate high quality junctions with areas of less than $0.1\mu m^2$ and critical current densities up to $10^5 A/cm^2$. Once the junction area and critical current density are known, the shunt resistance is determined from the hysteresis condition (2.9), $\beta_c<1$, and the SQUID self-inductance is chosen to satisfy the optimization condition $\beta \equiv 2LI_c \geq 1$.

Our SQUIDs are composed of edge junctions having areas of $0.05\text{-}0.12\mu m^2$, critical current densities up to $10^5 A/cm^2$, shunt resistances of 5-25Ω and junction capacitance of 10-20fF. Typical values of $\kappa \sim 7$ are obtained at 1.5K which implies that quantum noise effects should be significant. The SQUID self-inductance is 15-30pH. Although the junction capacitance cannot be measured directly, it can be fairly accurately deduced from the position of the LC resonance in the current-voltage characteristic of an unshunted (underdamped) SQUID, provided the loop inductance is known. The resonance appears as a small step in the I-V characteristic at about 0.75mV which corresponds to a frequency of about 365GHz. This implies that the $0.12\mu m^2$ junctions have a capacitance of 18fF which is substantially larger than the value C=10fF which would be estimated from the junction area alone. The most likely source of this discrepancy is the capacitance contributed by the portion of the counterelectrode which overlaps the top surface of the base electrode. This overlap is made somewhat larger than necessary so that extra contacts can be made to the arms of the counterelectrode.

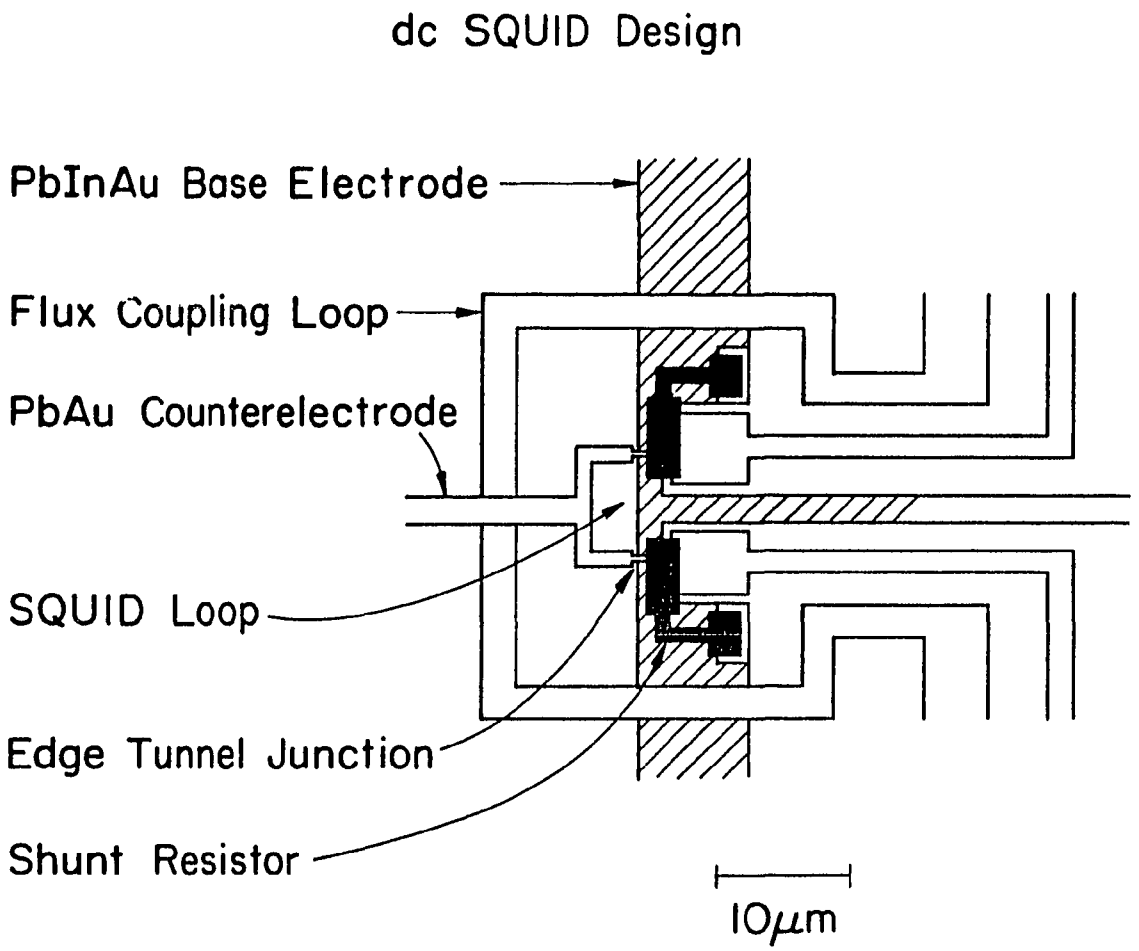

Figure 4.1 - Schematic of dc SQUID design.

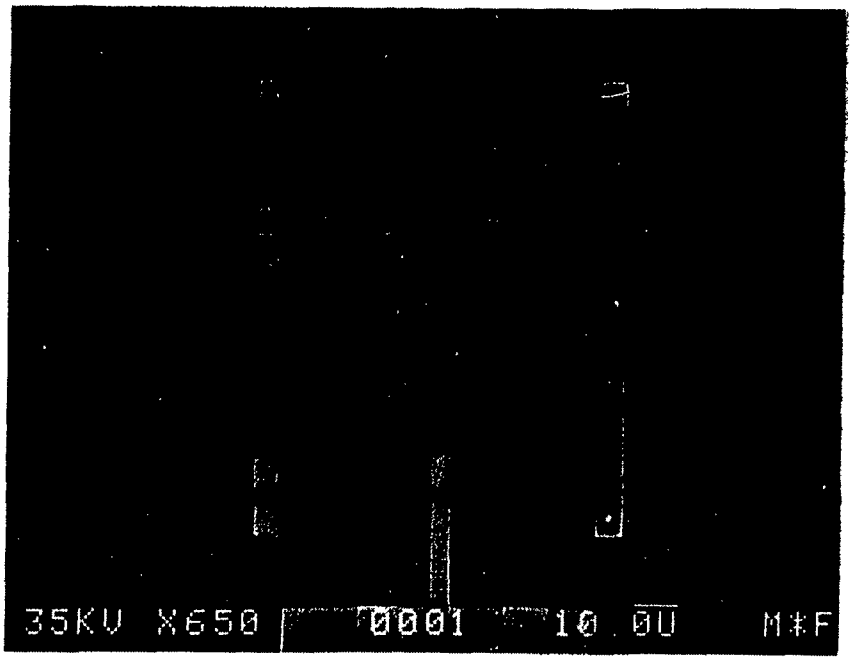

Figure 4.2 - Electron micrograph of dc SQUID.

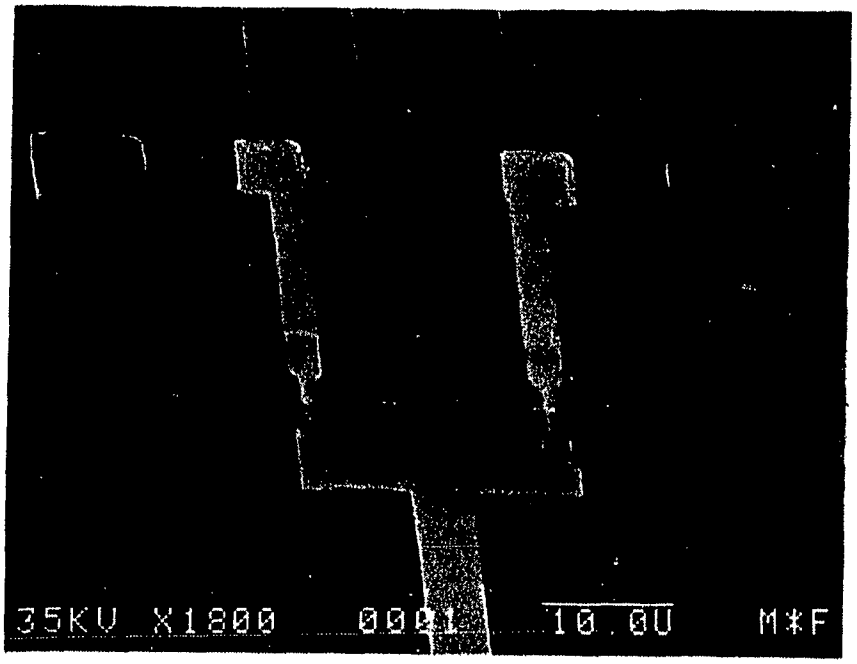

Figure 4.3 - Close-up view of SQUID loop.

These are used to accurately measure the SQUID self inductance as described below.

Our SQUID design is shown in Figure 4.1 along with electron micrographs of a finished device (Figures 4.2 and 4.3). Note that extra contacts are made to the U-shaped counterelectrode as well as to the base electrode strip which closes the SQUID loop. These contacts allow current to be forced around the SQUID loop so that the self-inductance can be accurately measured. The self inductance must be accurately known in order to make a good quantitative comparison of the results to theory. To eliminate resonances associated with parasitic inductance, the shunt resistors are ground-planed by the base electrode as much as possible. Lastly, some of our SQUIDs have an integrated thin film flux-coupling loop.

4.3 Device characteristics

Figure 4.4a shows the current-voltage (I-V) characteristic of one dc SQUID at flux biases of zero and $\Phi_0/2$. Device parameters for this SQUID are: junction area= $0.1\mu m^2$, C~ 15fF, L=20pH, R=7.6Ω, I_c= 100μA (at 1.25K), $j_c = 5x10^4 A/cm^2$. The critical current increases by about 20% from 4.2K to 1K and critical current modulation depth agrees well with computed values (Tesche and Clarke, 1977). Our SQUIDs show good signal properties as evidenced by the flux-voltage (V-Φ) characteristics plotted in Figure 4.4b for different values of the bias current. The curves are symmetric and large transfer functions, $\partial V/\partial \Phi$, (typically $25mV/\Phi_0$ at 1K) are attainable. To determine the transfer function, a small sinusoidal flux is applied to the SQUID and the output voltage is measured with a

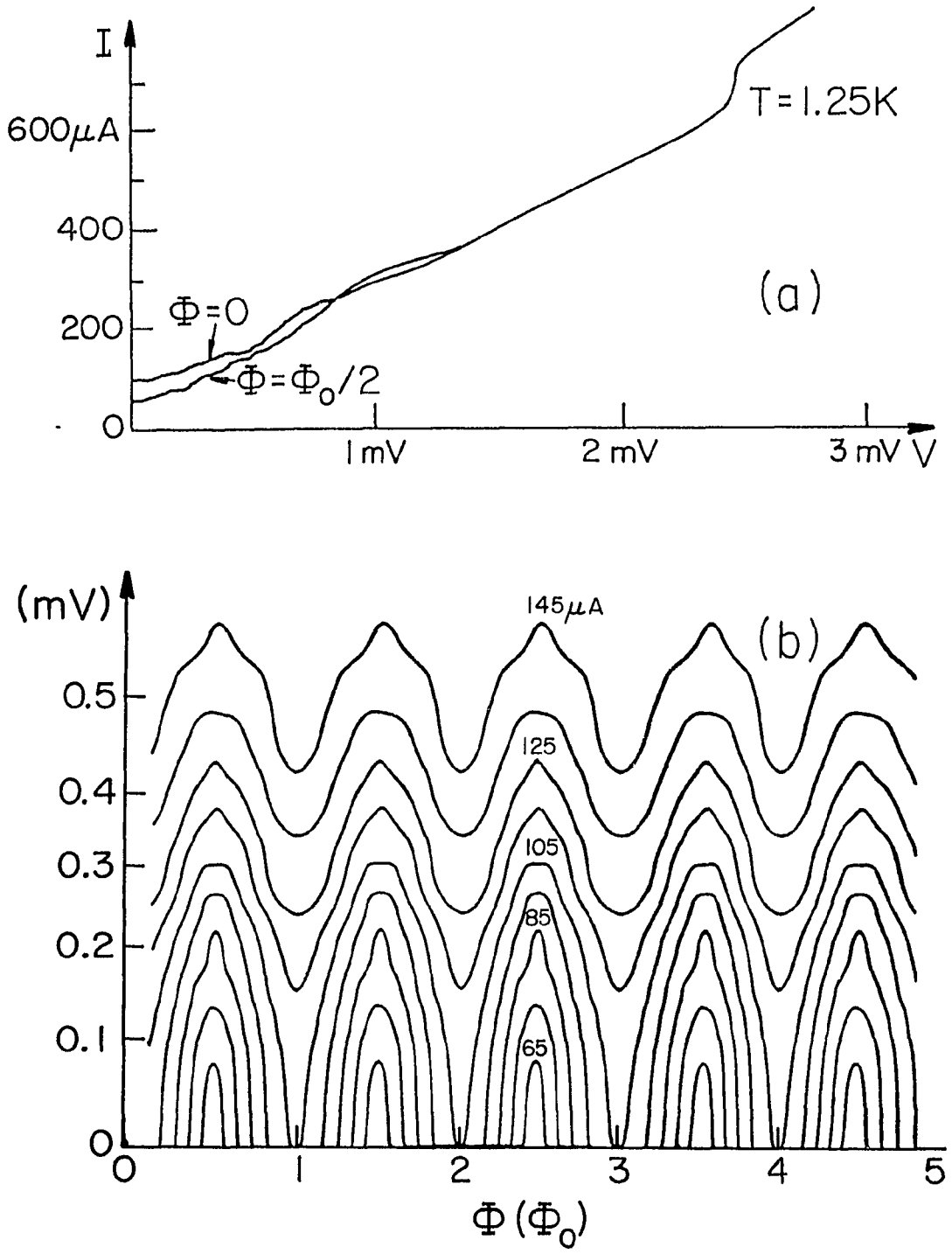

Figure 4.4 - SQUID signal properties. (a) Current-voltage characteristics for two values of applied flux. (b) Voltage-flux characteristics for different values of bias current.

lock-in amplifier. The periodicity of the V-Φ characteristic provides a convenient means for very accurately calibrating the applied flux. Very large transfer functions (up to 100mV/Φ_0) were measured in some SQUIDs. These devices show stronger asymmetry in V-Φ and more structure in the I-V characteristic. The ability to achieve such high flux sensitivity is most likely due to the low capacitance of our junctions. To eliminate hysteresis as a possible explanation, the flux-modulated voltage signal is observed on an oscilloscope and shows a smooth variation in amplitude as either the dc bias flux or bias current is varied. It is also observed that SQUIDs with integrated coupling loops have transfer functions about 50% smaller than for similar SQUIDs without them. The coupling loop is insulated from the SQUID but apparently contributes a significant parasitic capacitance and inductance which degrades the nonlinearity. The white noise measurements shown below are all for SQUIDs without coupling loops. Although we did not attempt to flux-lock our SQUIDs, the asymmetry and sharpness of the V-Φ characteristic may present some problems for SQUID operation in the usual mode; however, a clever readout scheme recently implemented by Foglietti et al. (1986) may be ideal for our devices.

4.4 Experimental methods

4.4.1 Cryostat design and shielding

The cryostat used for the measurements is relatively simple (Figure 4.5) although care must be taken to reduce interference from external sources of noise. The sample holder is made of a small block of plexiglass that has 16 wire-wrap pins pounded through it which are

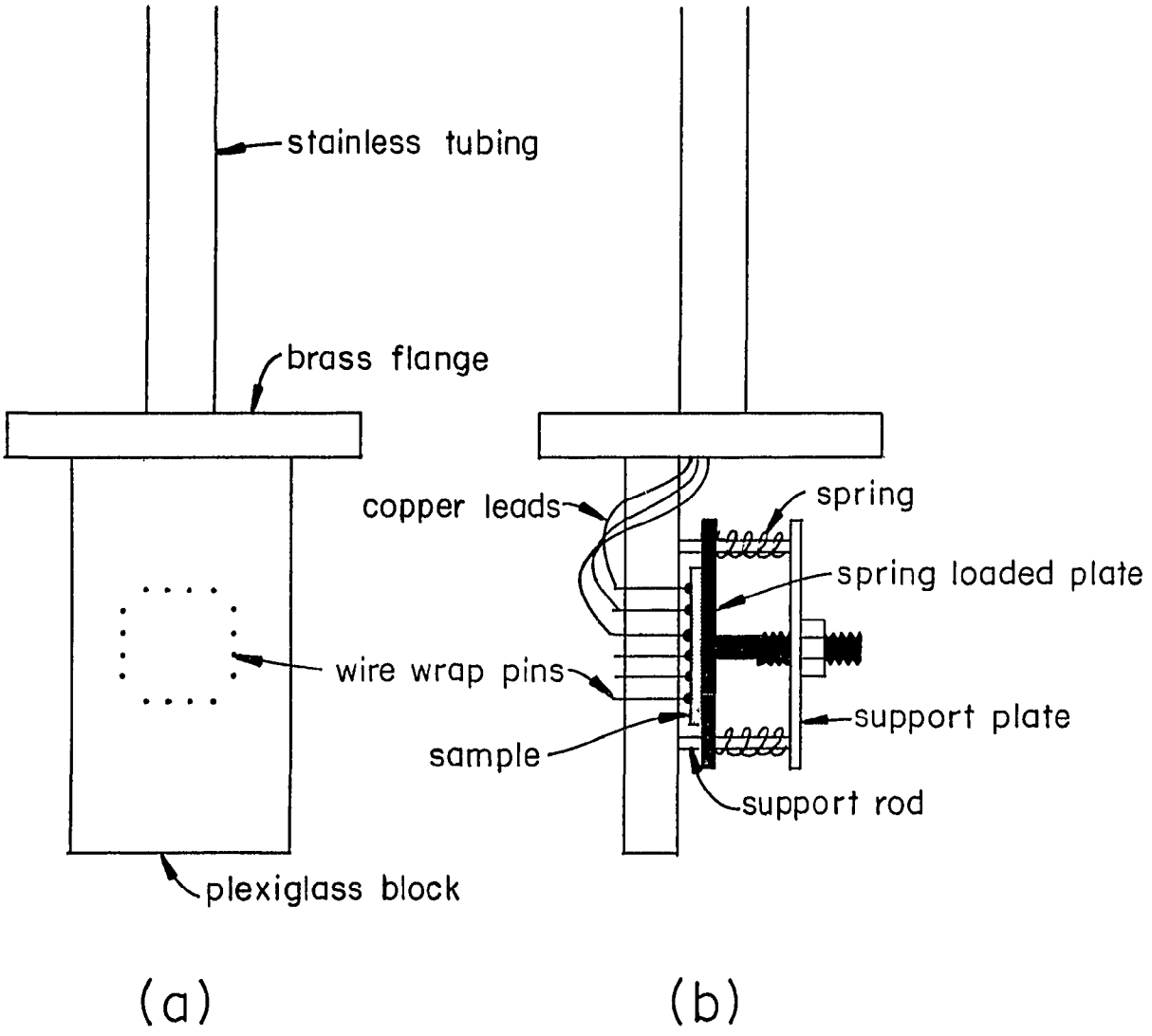

Figure 4.5 - Cryostat for noise measurements.

arranged in the same manner as the contact pads on the sample. Thin indium squares are placed on the contact pads and the sample is positioned so that the pads are aligned with the wire-wrap pins. A spring loaded plate pushes the sample against the plexiglass so that the pins sink into the indium squares and make electrical contact to the sample. A spring-loaded plate holds the sample in place. Copper leads are soldered to the wire-wrap pins on the opposite side of the plexiglass. They are routed through a stainless steel tube and enter a connector box at the top of the cryostat. To prevents pickup in the leads from reaching the sample, cooled resistors are used to form an RC filter with a room temperature capacitor. The signal leads for the noise measurements require coaxial cable (Lake Shore Cryogenics) because of the high frequencies involved (up to 5MHz) and the need for optimum shielding. They are routed separately from the other leads to minimize crosstalk. To reduce interference from external sources of noise, the sample space is enclosed within a brass can and a superconducting lead bag. Additional magnetic shielding is provided by a sheet of mu metal wrapped around the outside of the dewar. The entire experiment, except for some of the electronics, is located inside of an rf shielded enclosure (screen room). Despite the heavy shielding, our SQUIDs are still sensitive to 60 Hz noise so the power to the screen room must be turned off and all the electronics inside are run off of batteries.

4.4.2 Amplifier gain and noise calibration

White noise measurements of our SQUIDs pose formidable problems for the measurement electronics: 1) 'signal'-to-noise is low, 2) the dynamic

resistance is strongly temperature dependent which makes impedance matching difficult, 3) measurement frequencies of several megahertz are needed in order to circumvent the large amounts of 1/f noise and 4) the high non-linearity of our devices makes them susceptible to external noise which degrades flux sensitivity.

The most critical component of the measurement system is the preamplifier. The preamplifier, in conjunction with the impedance matching network (if one is used), dominates the overall performance of the measurement system. Selection of the preamp is largely determined by the measurement bandwidth. For low frequency applications (less than a megahertz), amplifiers with FET inputs are usually chosen. They have large input impedances (typically 1 MΩ) and optimum source resistances of 1-10kΩ. At higher frequencies, only low input impedance amplifiers are available which are designed to be matched to 50Ω sources.

The noise performance of an amplifier can be understood in terms of the model shown in Figure 4.6. The preamp input consists of a noiseless input impedance Z_i in parallel with a current noise (spectral density) S_I^{PA} and in series with a voltage noise S_V^{PA}. These noise sources are assumed to be independent, although at very high frequencies (>>10MHz) they can become correlated. The signal source has impedance Z_s and a voltage noise S_V. The voltage across Z_i is perfectly amplified by the preamp gain, G, to produce the output voltage $V_o = GV_i$. For the simplest example where the source is a simple resistor, R, the output voltage noise becomes:

$$S_o = [4kTR + S_V^{PA} + S_I^{PA}R^2] \left[\frac{GZ_i}{Z_i+R}\right]^2 \qquad (4.1)$$

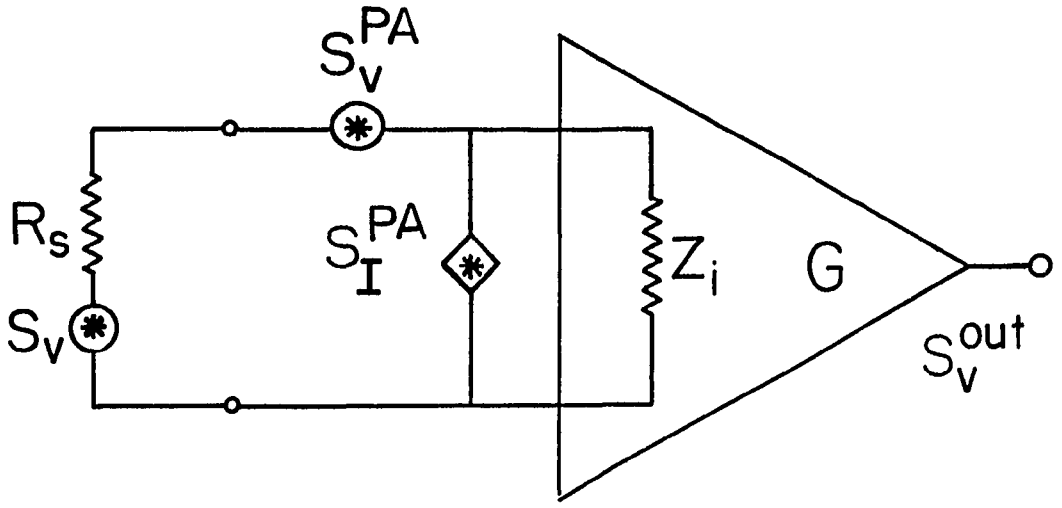

Figure 4.6 - Amplifier noise model.

In general, the parameters Z_i, S_V^{PA}, S_I^{PA}, and G are all frequency dependent and can even show some dependence on source impedance. Fortunately, it is not always necessary to know all these parameters accurately. Low frequency measurements can be particularly easy. If the source resistance is small ($<<1M\Omega$), the preamp does not load the signal source and the current noise can be neglected. The preamp voltage noise is determined by shorting the input and measuring the noise at the output (with a spectrum analyzer). The gain can be measured by applying a small calibrated signal and measuring the amplified output. Thermal noise of a resistor provides a convenient calibrated noise signal. To determine the noise of an unknown source, the preamp voltage noise is subtracted from the overall noise which is then divided by the gain.

Amplifier noise performance is a function of the source resistance. The best signal-to-noise is obtained for R_s equal to

$$R_{opt} = (S_V/S_I)^{\frac{1}{2}} \qquad (4.2)$$

For this source resistance, the amplifier current noise and voltage noise contribute equally. If $R_s<R_{opt}$, the voltage noise dominates and if $R_s>R_{opt}$, the current noise dominates. But in many cases, it is inconvenient or undesirable to vary the source resistance. In addition, the current noise is usually very difficult to measure, so that the final result is often more accurate if the source resistance is somewhat less than R_{opt}. When optimum impedance matching is required, a noiseless matching network such as a transformer or a tank circuit can be used. For the low frequency noise measurements performed in this work, adequate signal-to-noise was available without impedance matching.

High frequency noise measurements are considerable more difficult. The amplifiers are designed to be matched to 50Ω sources; therefore, the source resistance, the input impedance and the optimum source resistance are about the same. This complicates the analysis of the noise measurements, especially at high frequencies where the SQUID noise is small. Fortunately, there is a way to determine the overall preamp gain and noise contribution without measuring the amplifier parameters individually. This is accomplished by measuring the noise of a (metal film) resistor at different temperatures. The total noise of the preamp output (4.1) will be linear in temperature (Figure 4.7) with an effective gain determined from the slope (Figure 4.8a) and an overall background noise is given by the y-intercept (Figure 4.8b). Only three temperature points (295K, 77K, 4.2K) were measured, but this was sufficient for the accuracy required in this experiment (5%). Note from (4.1) that the loading of the source by the preamp is automatically folded into the gain and that the overall preamp noise contribution can be determined even though the individual (voltage, current) contributions are not known. As before, the net noise of the source is then determined by subtracting off background and dividing through by the gain. The drawback of this method is that the gain and noise must be determined for each value of source resistance. For many experiments, the source resistance does not vary, but such is not the case here. The gain and noise were measured for eight different source resistances in the range $25\Omega<R<400\Omega$ and a fitting routine was used to interpolate between points.

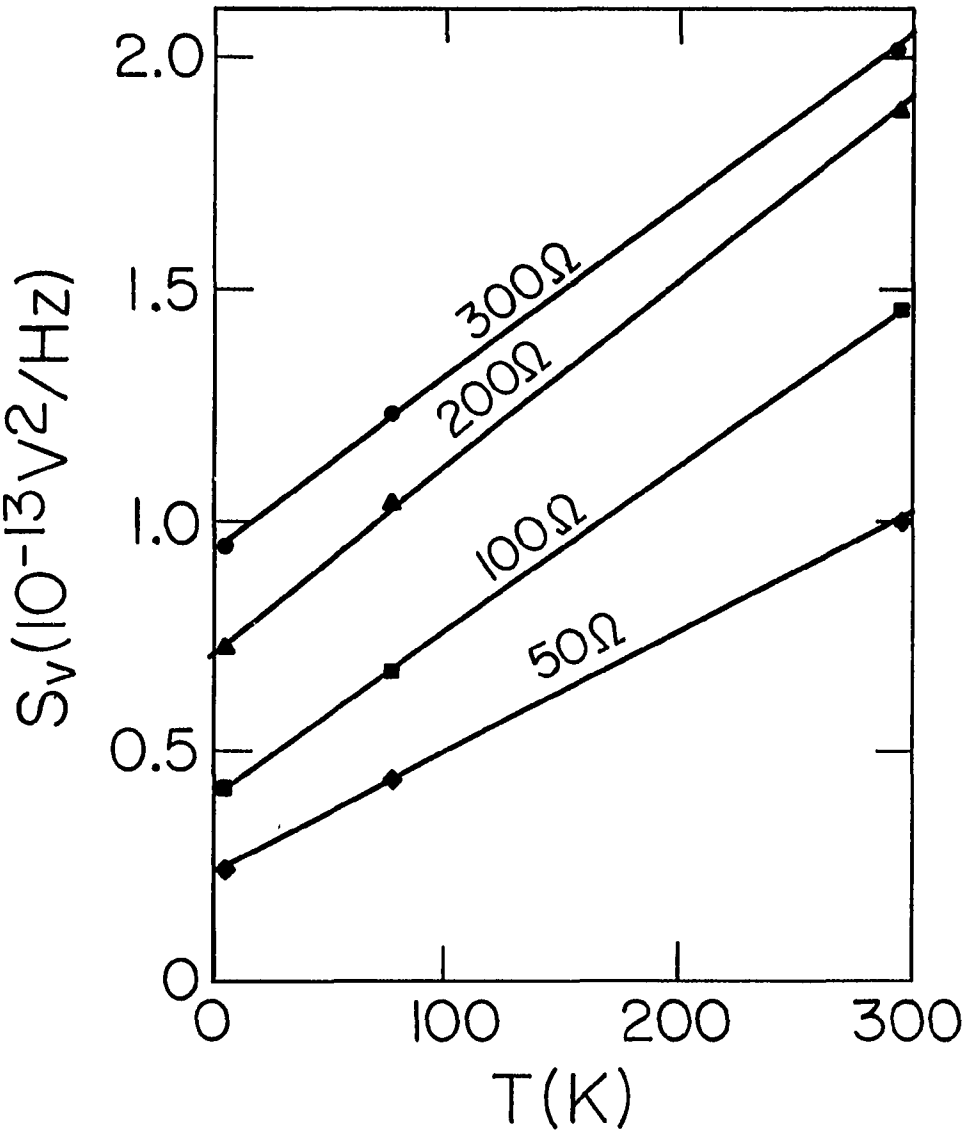

Figure 4.7 - Total preamp noise versus temperature for four values of source resistances.

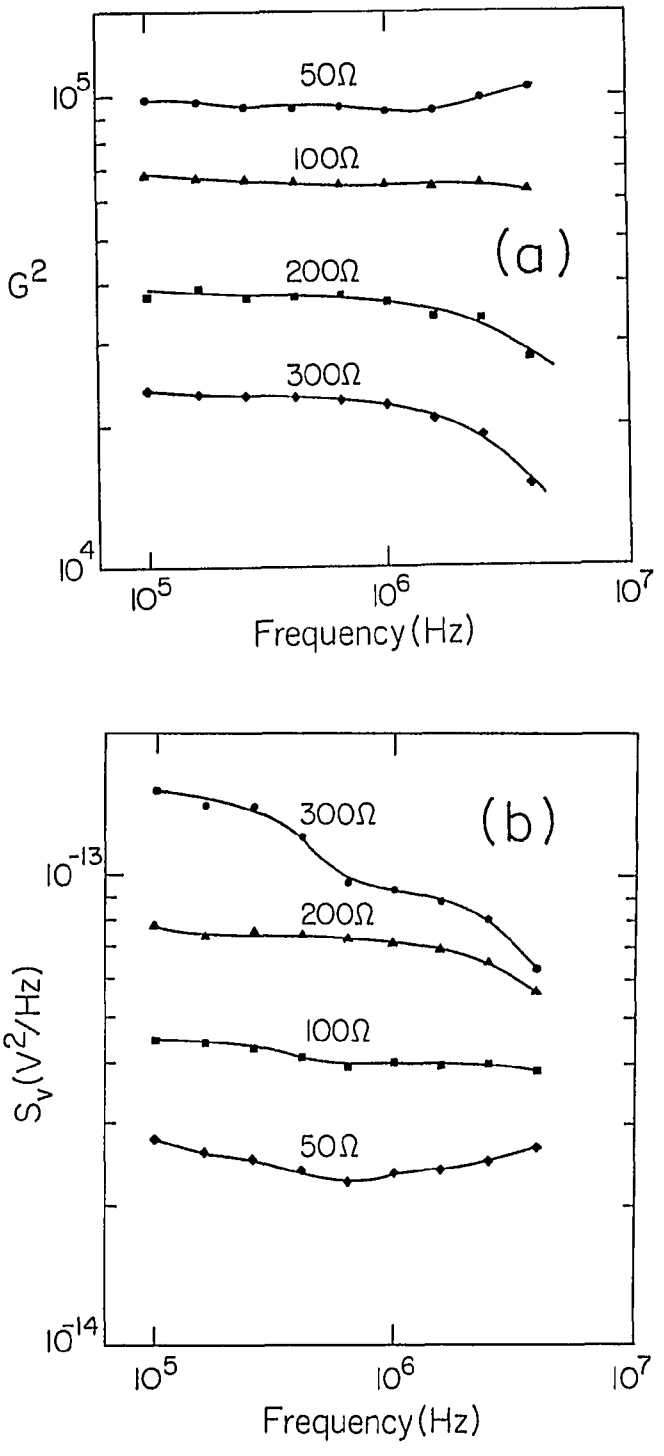

Figure 4.8 - Frequency dependence of preamp (a) effective gain and (b) effective noise for four values of source resistances.

4.4.3 Noise measurement system

A low input-impedance (~180Ω), 50MHz bandwidth amplifier (TRONTECH ATC-W50) with no impedance matching network is used for most of the measurements. This amplifier has nearly flat characteristics over the bandwidth of interest (100kHz-10MHz) for a source resistance of 50Ω. The amplified signal is then measured with a spectrum analyzer (Hewlett Packard 3585A). In principle, only a single (high) frequency measurement is sufficient; but since the uncertainties in the amplifier noise and gain increase with frequency (due to rolloffs) it is best to perform the measurement at a frequency just above the 1/f crossover. In our SQUIDs, the low frequency noise crossover extends out to about a megahertz. Measurements are made at nine logarithmically spaced frequencies between 100kHz and 4MHz, and the white noise level is deduced. Despite the low signal-to-noise (typically of order unity), the noise can in principle be determined to arbitrary precision by averaging for long times; however, amplifier drift still limits the overall accuracy. To minimize error due to drift, three sets of measurements are performed and prior to averaging, the results are inspected to insure that a systematic drift is not present. The spectrum analyzer is under computer control to facilitate the data acquisition.

4.5 White noise measurements and results

For white noise measurements, the SQUID is biased at maximum transfer function by adjusting the bias current and flux. The bias voltage is typically 50-90 μV and shows a slight decrease with temperature. When the transfer function is very high (>25mV/Φ_o), it is

observed that connecting the amplifier depresses the transfer function by up to 20% at the lowest temperatures, presumably due to increased noise rounding. This may well degrade the noise performance of the SQUID; however, the voltage noise should approximately scale with the transfer function so that S_E does not suffer appreciably from this effect. To reduce external noise, a cooled shunt capacitor limits the measurement bandwidth to about 10MHz.

In Figure 4.9, the flux energy resolution for a typical SQUID (SQUID A in Table 4.1) is shown as a function of frequency. Note here that the noise at low frequency does not display a simple 1/f behavior. This will be discussed at length in the next chapter. Above a few megahertz, the noise flattens out and the white noise levels can be deduced. In Figure 4.10, the limiting high frequency values of S_E are plotted versus temperature for three SQUIDs. Device parameters are listed in Table 4.1. The largest sources of error come from the measurement of the SQUID voltage noise and from the extrapolation of the white noise level from the spectrum. The other quantities contained in S_E -- the SQUID self inductance, L, and the transfer function, $\partial V/\partial \Phi$-- are much more accurately known (~5%). Depending on signal-to-noise and source resistance, the overall uncertainty in S_E is about 20-35% which is typical for this kind of noise measurement.

According to the Tesche-Clarke theory, S_E should roughly scale with $(LC)^{\frac{1}{2}}$ for an optimized device. But in practice, the optimization condition $\beta_c=1$ is only approximately satisfied since the critical current is difficult to control and the nonhysteresis condition $\beta_c<1$ must also be observed. The parameter $\kappa \equiv eI_cR/kT$ which scales with the flux sensitivity

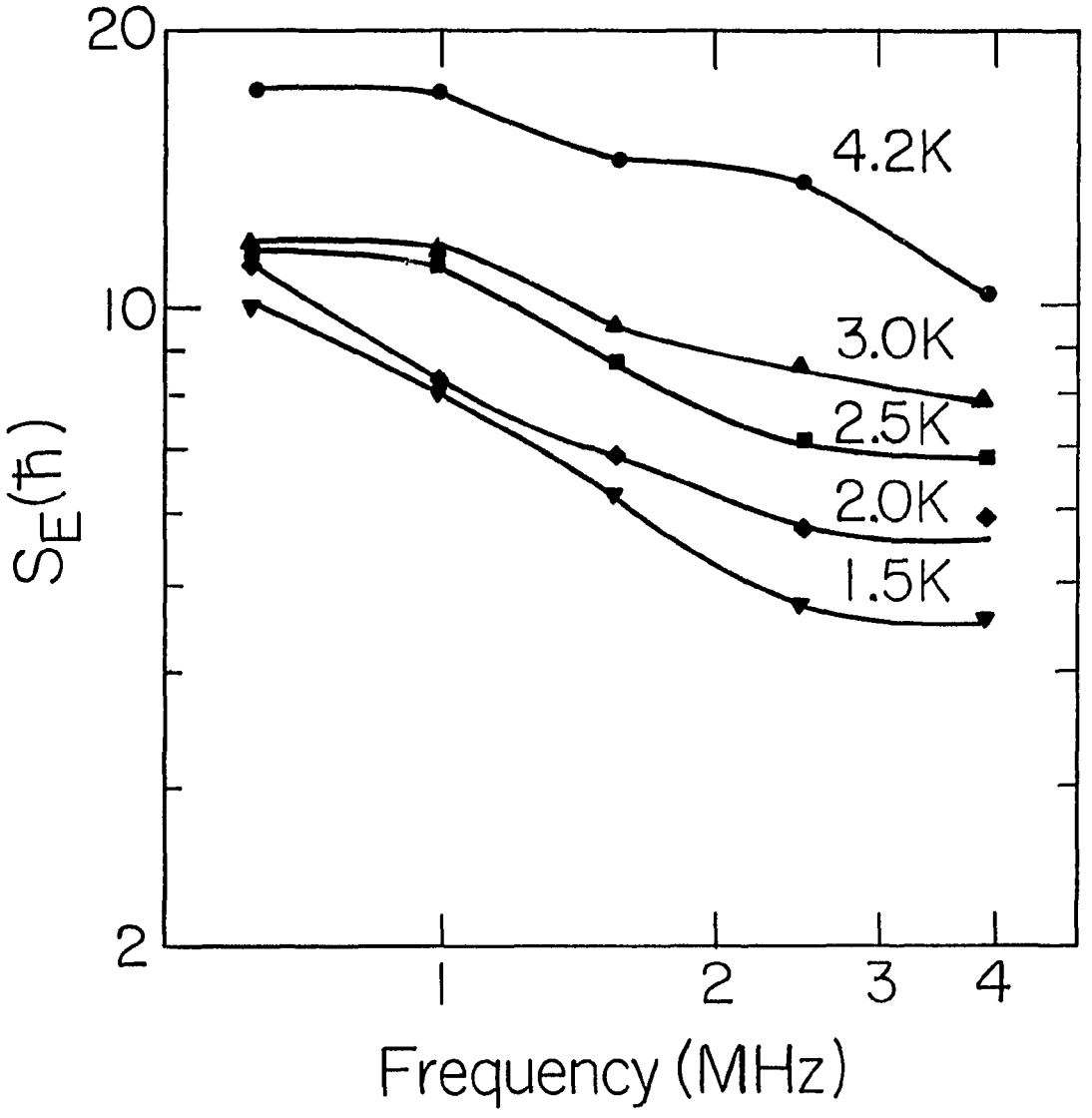

Figure 4.9 - Flux energy resolution versus frequency for SQUID A.

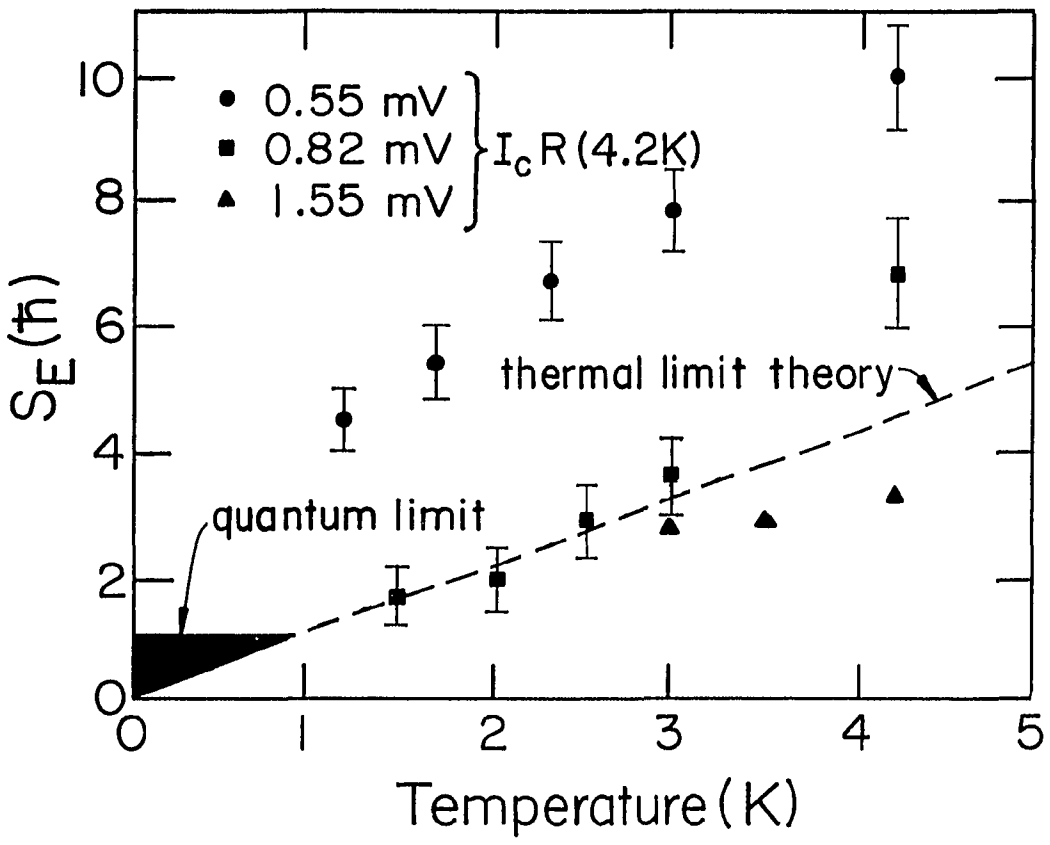

Figure 4.10 - Limiting values of flux energy resolution versus temperature for three SQUIDs.

	SQUID A	SQUID B	SQUID C
L	17.7pH	15.6pH	15.6pH
I_c	92.2μA	137μA	258μA
R	12Ω	12Ω	12Ω
C	15fF	15fF	
$(\partial V/\partial \Phi)$ at 4.2K	3.5mV/Φ_o	7.3mV/Φ_o	7.6mV/Φ_o
$(\partial V/\partial \Phi)$ at 1.5K	19.6mV/Φ_o	64.6mV/Φ_o	----

Table 4.1 - SQUID parameter value for devices shown in Figure 4.10.

and measures the importance of quantum noise effects provides a more appropriate measure of SQUID performance. This is consistent with the measurements in Figure 4.10 which show that devices with larger values of $I_c R$ perform better as expected. SQUID A shows behavior typical of several devices that were measured. Although these SQUIDs have very good (symmetric) signal properties, their performance is inferior to devices with larger values of $I_c R$ which show more nonideal behavior. SQUID C displays the best performance at high temperatures but becomes hysteretic below about 3K. For many practical applications where operation is restricted to 4K, this would be an ideal device. SQUID B had the best sensitivity and performance of all the devices that remained nonhysteretic at the lowest temperatures. The dashed line in Fig. 2 shows the theoretical thermal limit prediction for SQUID B which is in reasonable agreement with the data. Although quantum-limited performance is not observed, the minimum S_E of $1.6\pm.5\hbar$ obtained at 1.5K is the lowest measured value yet reported.

The only other SQUID of comparable performance was studied by Van Harlingen et al. (1982) who measured $S_E = 3\hbar$ at T=1.4K, f=200kHz and deduced an extrapolated white noise level of less than $2\hbar$. However, the high flux sensitivity of their SQUID is achieved at the expense of small self inductance (L=2pH). To achieve good flux coupling, most planar SQUIDs are designed with L~100pH; hence, their device is not well suited for use as a practical detector. Our SQUIDs have both larger self inductance (20pH) and higher critical current density ($5\times10^4 A/cm^2$). By reducing the current density to about $10^4 A/cm^2$, the self inductance could be increased to 100pH while maintaining excellent flux sensitivity. A

lower current density would also make fabrication easier and improve the stability of the device characteristics. Another study that deserves mention was reported by Wellstood et al. (1986) who measured the noise of several large inductance (>100pH) planar SQUIDs in a dilution refrigerator. Despite the need for lower temperatures, these are the only SQUIDs that have been studied below 1K. The junctions have areas of $2x2\mu m^2$ and critical current densities on the order of $10^2 A/cm^2$. At about 200mK, the noise begins to flatten out with temperature and approach a limiting value of $S_E \approx 12\hbar$. However, this flattening is not believed to be a quantum effect; rather, it is attributed to self heating in the shunt resistor. For our devices, heating is also expected to be a problem below a few tenths of a degree; however, it can be reduced by enlarging the surface area of the shunt resistors subject to the restrictions outlined below.

4.6 Limitations of edge junction technology

Future improvements in SQUID performance are likely to be difficult to attain. The technology has now reached the stage where a new set of rather fundamental problems must be encountered. The main obstacle to using lower temperatures-- self-heating of the shunt resistor-- has already been mentioned. Since the heating scales with the power dissipation per unit area, it can be reduced be enlarging the area of the resistor; but only at the expense of increasing the parasitic capacitance of the shunt. Similarly, the shape of the resistor must compromise between minimizing parasitic inductance and obtaining the large resistances which are needed for maximum device sensitivity. Therefore,

the shunt must be carefully designed in order to take these considerations into account. These constraints become more difficult to satisfy as the junction area is made smaller and the operating frequency and shunt resistance increase. Another limitation concerns the maximum value of shunt resistance that can be used. In the C=0 limit, the hysteresis condition will be satisfied for arbitrarily large resistances; however, as the shunt resistance is increased, at some point it will no longer dominate the conductance from other sources as assumed by the RSJ model. This is particularly a problem at high current densities where the I-V characteristic exhibits nonideal structure due to increased leakage currents, parasitic resonances and subharmonic pairbreaking. If excess conductance or parasitic circuit impedances cause significant deviations from an ideal RSJ model, the signal and noise properties can be seriously degraded. Lastly, the usefulness of these devices may be somewhat diminished as the low frequency crossover extends out to higher frequencies. Although the low frequency noise performance of our SQUIDs is quite good, the primary purpose of making these ultrasmall devices is to take full advantage of their outstanding white noise properties. Fortunately, there are many applications for SQUID amplifiers with bandwidths of 100MHz or more in conjunction with rf detection and high frequency mixing. The next section summarizes the progress in constructing practical SQUID detectors including recent work on rf amplifiers incorporating microfabricated planar dc SQUIDs similar to ours.

4.7 SQUID amplifiers

It should be emphasized that while this work is concerned with the intrinsic noise properties of isolated dc SQUIDs, most practical SQUID detectors are operated with a superconducting input coil which couples flux from the signal source into the SQUID loop. Although the SQUID is a flux-to-voltage transducer, it can be used to measure any signal which induces current to flow through the input coil. SQUIDs have been configured to measure voltage, current, magnetic fields, field gradients, etc. through proper design of the input circuit. The overall performance of these devices is determined by many factors such as the design of the input circuit, the coupling efficiency of the pickup and input coils, the noise of the feedback electronics, and the intrinsic noise of the SQUID itself. In addition, the coupling between the SQUID and the input circuit through the mutual inductance and stray capacitance can alter the properties of the SQUID itself in a way which is very difficult to model. Hence, the achievement of quantum-limited flux energy resolution in an isolated dc SQUID would represent only a first step (albeit a very important one) towards the ultimate goal of attaining an ideal quantum-limited linear amplifier.

The first dc SQUID amplifiers were constructed on cylindrical quartz substrates using fairly crude fabrication techniques (Clarke et al., 1976). The cylindrical geometry was ideal for efficient flux coupling, but the ultimate performance of these devices suffered from a relatively high level of intrinsic SQUID noise. With the adoption of thin-film microfabrication techniques came a new generation of planar dc SQUIDs with vastly improved sensitivity, but reduced coupling efficiency.

Recent studies have focused on microfabricated SQUID amplifiers with planar, multi-turn input coils (Ketchen et al., 1982, Hilbert et al., 1985a). The behavior of these devices is very complicated but is now becoming better understood. They appear to suffer more strongly from parasitic capacitance and interaction with the input circuit; however, their overall performance is very promising and they have already been adapted for use in nuclear magnetic quadrapole (Hilbert et al., 1985b) and magnetic resonance measurements (Freeman et al., 1986).

Chapter 5

LOW FREQUENCY NOISE AND ELECTRON TRAPPING IN DC SQUIDS

5.1 Introduction

Although the initial goal of this research was to study the white noise properties our SQUIDs, the low frequency noise exhibits very surprising and interesting behavior. For example, the noise spectra display striking differences from what is most often observed in other systems: the average spectral slope is unusually flat (-2/3) and prominent Lorentzian-like bumps are often present. Yet much of the data is consistent with recent measurements reported in small area tunnel junctions. In particular, there is strong evidence that the noise arises from the trapping of electronic charge into localized defect states within the tunneling barrier. The use of submicron area junctions allows us to directly observe these trapping events and conclusively identify the resulting critical current fluctuations as the dominant source of the low frequency noise in our SQUIDs.

The first section of this chapter reviews the important theoretical model of Dutta, Dimon, and Horn which provides a framework for much of the discussion. The wide range of low frequency noise behavior observed in previous studies of dc SQUIDs is then summarized. Our results are then compared to recent measurements of small-area single junctions, and the direct observation of individual electron trapping events is demonstrated. Finally, the failure of the Dutta, Dimon, Horn model to explain the weak temperature dependence of our data suggests that the noise in this low temperature system displays tunneling rather than

thermally-activated kinetics. The material presented here is largely based on papers by Wakai and Van Harlingen (1985 and 1986).

4.2 The Dutta-Dimon-Horn model

Although 1/f noise has been studied for several decades, much of our understanding has come just within the last few years. In retrospect, this may seem rather surprising given the ubiquity of the phenomenon and its proclivity to appear in even the simplest of systems. Accordingly, many early theories attempted to explain 1/f noise in terms of universal properties of solids. The limited success of these theories was a first sign that the origin of the noise was very system dependent. In addition, experimental efforts to characterize the noise were frustrated by several factors: 1) the inability to reproduce measurements in different laboratories and 2) the paucity of information which can be extracted from ordinary power spectrum measurements. The situation began to change when a number of carefully controlled experiments provided evidence that the 1/f noise was caused by different types of microscopic defects in each system. Soon afterwards, a major breakthrough was achieved with the Dutta, Dimon, and Horn (DDH) model which forms the basis for our present understanding of 1/f noise. This will be discussed below in some detail even though it may not apply at the low temperatures used in our experiments. A much broader discussion of 1/f noise can be found the recent review article of Weissman (1987).

Many simple random processes exhibit fluctuations which decay exponentially with a characteristic time τ

$$\langle x(t)x(0)\rangle \sim \exp-(t/\tau) \qquad (5.1)$$

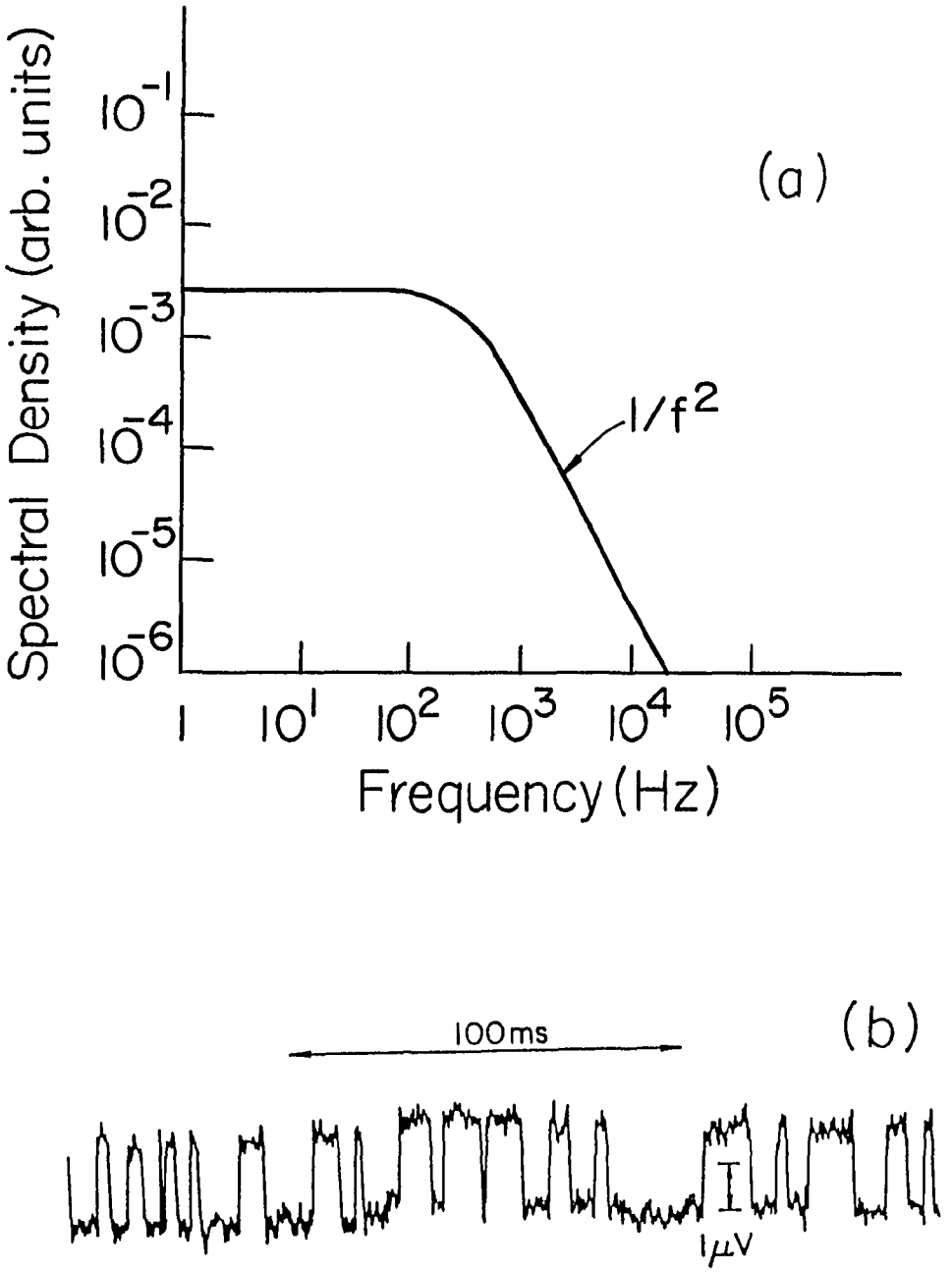

Figure 5.1 - (a) Debye-Lorentzian power spectrum. (b) Random telegraph signal.

The power spectrum of these fluctuations has a Debye-Lorentzian or Lorentzian form (Figure 5.1a)

$$S \sim \tau/(1+\omega^2\tau^2) \tag{5.2}$$

with a "corner frequency" $1/\tau$. In general, the fluctuating quantity can assume a continuous range of values, but interest has mainly focussed on the simplest case where the fluctuators can be modeled as two-level systems (TLS). The signal from a single TLS is often described as a random telegraph signal (Figure 5.1b) which is characterized by two mean lifetimes. Its power spectrum is Lorentzian with a characteristic time determined by the sum of the two individual rates (Machlup, 1956)

$$1/\tau_{eff} = 1/\tau_1 + 1/\tau_2 \tag{5.3}$$

A simple example of a TLS is an ion which moves between two metastable positions and affects the conductivity differently in each state. Another example more relevant to the present work is the trapping and untrapping of an electron at a localized defect site. Most current models assume that the overall low frequency noise arises from a superposition of many such fluctuators which each add a Lorentzian contribution to the overall power spectrum

$$S(\omega) \sim \int \frac{\tau}{\omega^2\tau^2 + 1} \, D(\tau)d\tau \tag{5.4}$$

If the distribution of characteristic times D(t) is proportional to $1/\tau$, the resulting power spectrum will vary as 1/f over many frequency decades as illustrated in Figure 5.2. However, it is clear that nearly any spectral shape can be accounted for from this kind of construction. The

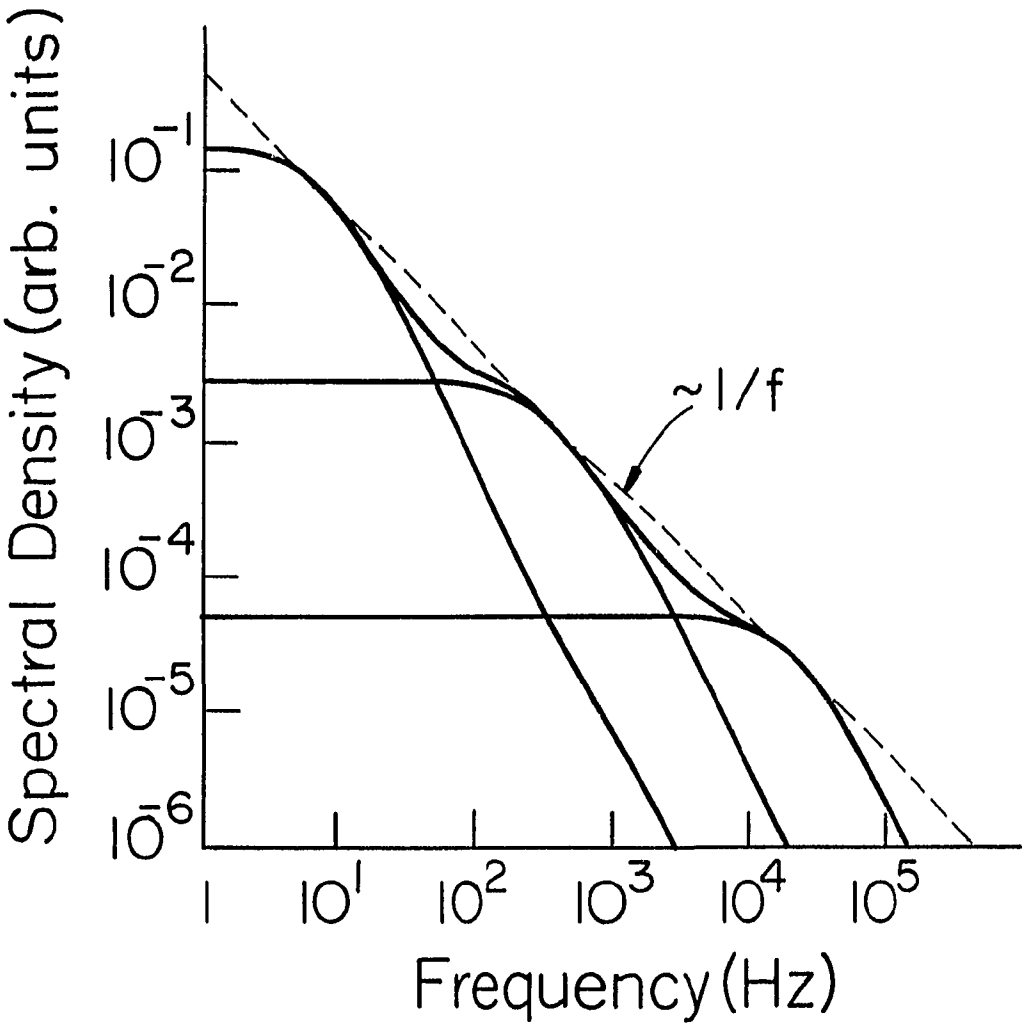

Figure 5.2 - Superposition of Lorentzian spectra which approximate 1/f noise.

task is now to justify the $1/\tau$ distribution of times and, if possible, devise experimental tests to verify the essential details of the model. This was accomplished by DDH for the case of thermally-activated noise kinetics where the characteristics times have the form

$$1/\tau = 1/\tau_0 \exp-(E_a/kT) \qquad (5.5)$$

where $1/\tau_0$ is the attempt frequency and E_a is the activation energy. The results are not sensitive to the exact value of the prefactor (attempt frequency) and it is taken to be a constant on the order of a typical phonon frequency. These assumptions introduce temperature dependence into the problem and parametrize the frequencies in terms of an activation energy E_a. A simple change of variables ($f \rightarrow E_a$) shows that a 1/f power spectrum will result if the distribution of activation energies, D(E), is constant. Unfortunately, this condition will not often be satisfied in solid state systems because the noise processes tend to have characteristic energies. This apparent shortcoming led many to doubt the efficacy of the model until, in 1981, DDH demonstrated that the condition could be somewhat relaxed. As long as D(E) is slowly varying on the scale of kT, the spectrum will show only small deviations from 1/f as is often observed in real systems. They show that the power spectrum can then be expressed very simply in terms of D(E)

$$S(\omega) \sim (kT/\omega)\, D(E^*) \qquad (5.6)$$

where $E^* = -kT \ln(\omega\tau_0)$. In addition, they derive a relationship between the slope of the spectrum, $\alpha = \partial S/\partial\omega$, and the temperature dependence of the noise magnitude

$$\alpha(\omega,T) = 1 - \frac{1}{\ln(\omega\tau_o)} \left[\frac{\partial \ln S(\omega,T)}{\partial \ln T} - 1 \right] \qquad (5.7)$$

This result was of great importance because it provided a means for testing the essential correctness of the model by very accurately measuring the temperature dependence of the noise slope and magnitude. The gist of (5.7) is that the temperature dependence of the noise magnitude becomes stronger as the spectral slope deviates from unity. DDH found good qualitative agreement between (5.7) and noise measurements in metal films.

Some insight into the DDH model can be gained by multiplying the power spectrum by frequency so that the individual Lorentzians appear as broad peaks which dominate the noise at their characteristic frequency $1/\tau$. A 1/f spectrum now appears as a line of zero slope (Figure 5.3) so that small deviations from 1/f are more easily seem. If the spectral features arise from thermally activated processes, then increasing the temperature will simply cause them to shift to higher frequency according to (5.5). As a result, changes in the noise magnitude with frequency and temperature are related. This leads to the DDH relation (5.6) which is valid in the limit of many fluctuators. In addition, (5.8) shows that f*S(f) is essentially the distribution of activation energies, $D(E^*)$. Although the range of E^* available from most spectra is small, in some cases, a peak in the distribution has been observed. This defines a characteristic energy for the activated processes which provides an important clue as to the microscopic origin of the noise.

The DDH model provides a useful framework for understanding 1/f noise; however, good quantitative agreement with (5.6) is not observed

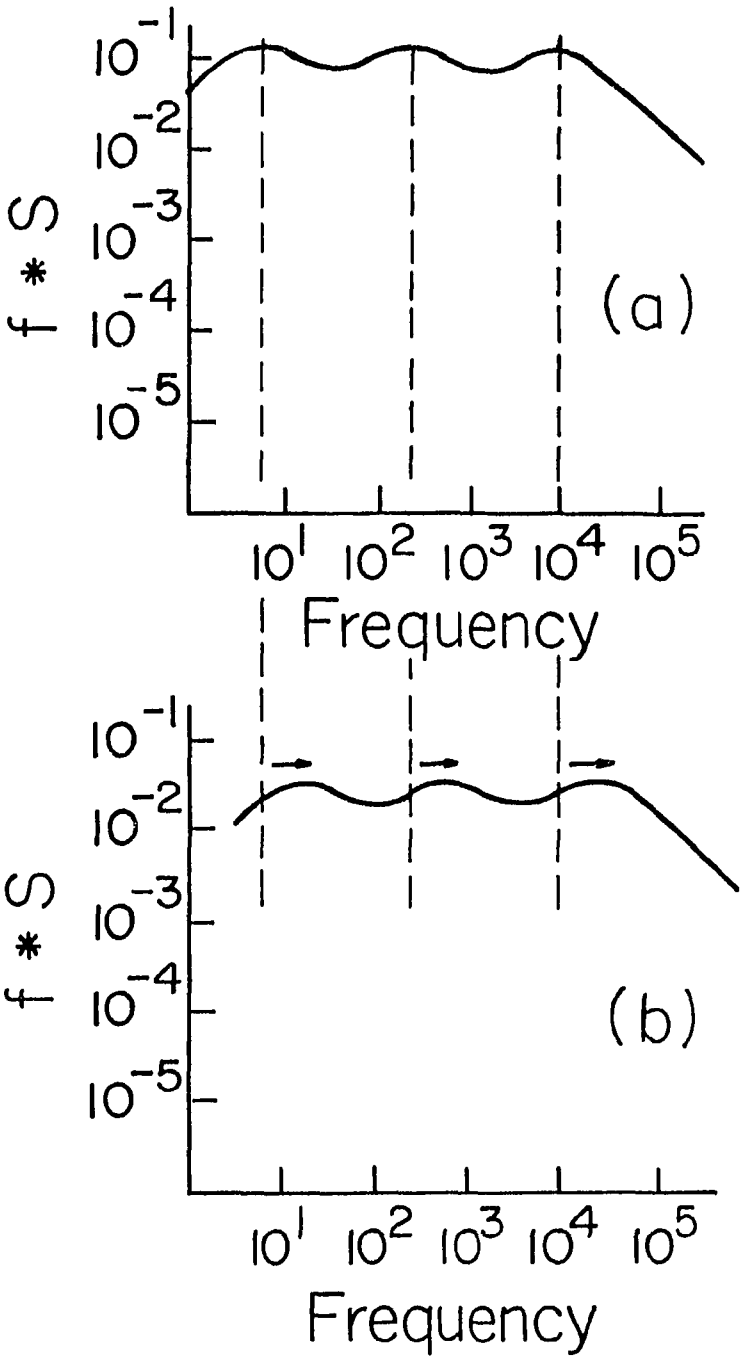

Figure 5.3 - (a) f*S(f) versus frequency for a superposition of three Lorentzian spectra. (b) At higher temperature.

because several simplifying approximations are used. More importantly, the model is only valid for thermally activated noise kinetics. At low temperatures where quantum tunneling is important, the model is not expected to apply. Note that even in the absence of thermal activation, a 1/f spectrum is not that difficult to obtain. It only requires that the characteristic times vary exponentially in some parameter which has a broad distribution. In these cases, the temperature dependence of the noise is likely to be quite different and should therefore provide an important clue as to the origin of the noise.

5.3 Low frequency noise in dc SQUIDs

Despite its practical importance, low-frequency noise in dc SQUIDs has not been well characterized and its origins are not fully understood. The observed voltage noise can be caused by a real flux noise coupling through the SQUID loop or by critical current fluctuations within the individual junctions. A survey of results reported by various groups reveals that a wide range of behaviors is observed between different SQUIDs. The first extensive study of SQUID 1/f noise was performed by Koch et al (1983). They measured SQUIDs with a wide range of geometries and device parameters and found that the 1/f noise was due to an apparent flux noise of unknown origin which was remarkably similar in magnitude for all the SQUIDs studied; i.e. the noise did not scale with device parameters (e.g. the inductance) as expected. In contrast, Tesche et al. (1985) reported a very low 1/f noise arising mostly from critical current fluctuations. And recently, Wellstood, et.al. (1986) have identified several types of low frequency SQUID noise over the temperature range

22mK-4.2K: above 1K, the 1/f noise arises from critical current fluctuations in SQUIDs with Pb alloy loops, but it appears to be a flux noise when the loops are made of Nb. Below 1K, a flux noise with an $\sim f^{-2/3}$ spectral density is always observed, regardless of loop composition. Despite much progress in our understanding of low frequency noise, the origin of flux noise in SQUIDs remains obscure. In addition, the temperature dependence of the noise does not always agree with predictions of the Dutta-Dimon-Horn model. For these reasons, low frequency SQUID noise remains of considerable scientific and technological interest.

5.4 Low frequency noise measurements

The dc SQUIDs studied here are very similar and if not identical to the devices described in the last chapter. The current and flux bias are adjusted to give maximum transfer function as for the white noise measurements. Below 50kHz, the voltage is first amplified with an ultralow noise FET preamp (Brookdeal 5004) and the spectral density is obtained by sampling and fast Fourier transforming the voltage noise with a DEC LSI-11/23 minicomputer. Above 50kHz, the noise is amplified by a low input impedance preamplifier and measured with a spectrum amplifier as described in section 4.5.

Figure 5.4 shows the equivalent input flux noise, S_Φ, for two SQUIDs measured over a wide frequency range at T=4.2K and T=1.5K. Below the onset of the white noise regime, about 1MHz, the noise spectrum exhibits considerable structure as a function of frequency and is clearly not well described by a simple power law. The most notable features are (1) the

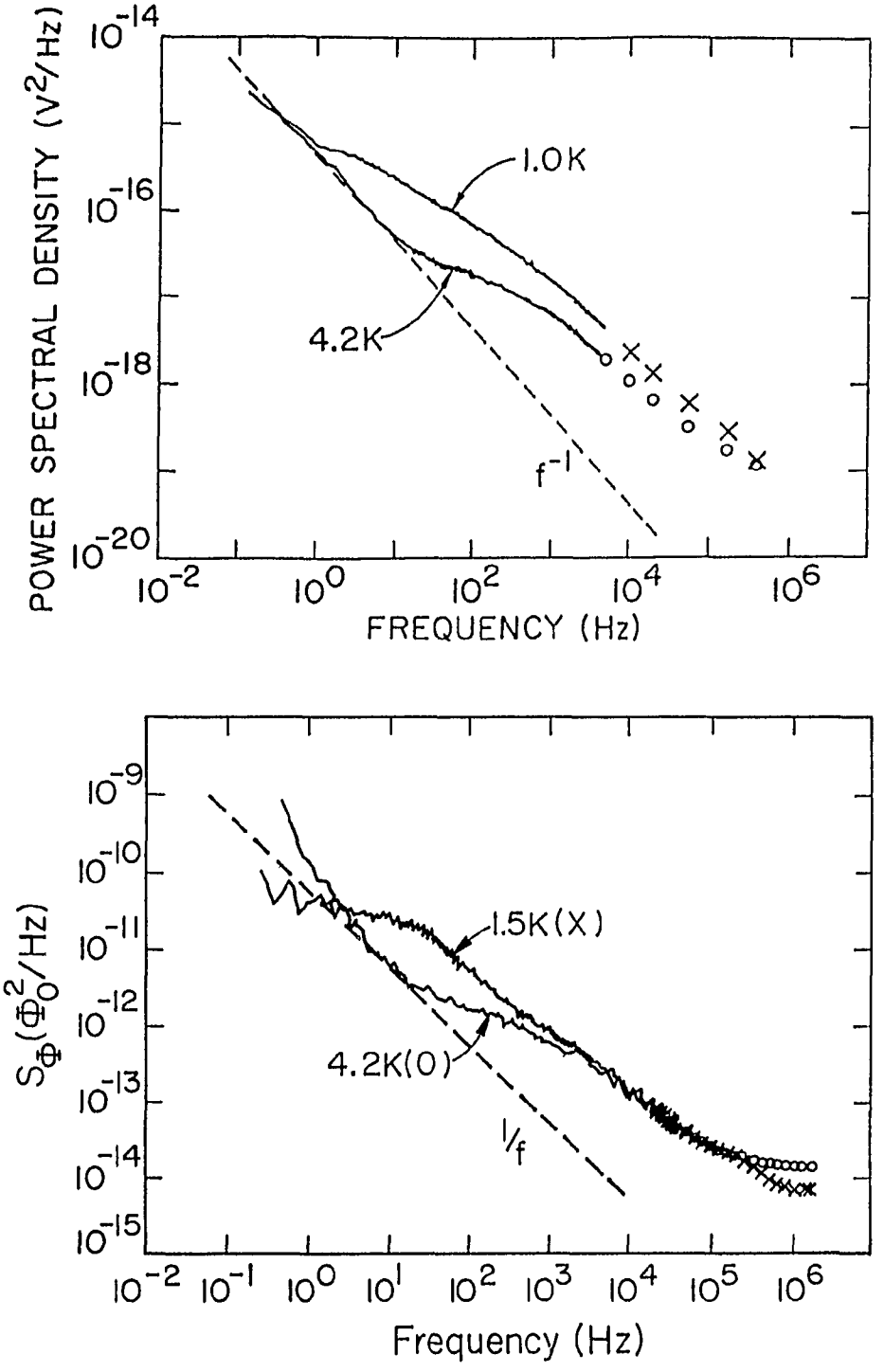

Figure 5.4 - Equivalent input flux noise versus frequency for two SQUIDs.

presence of broad Lorentzian-like bumps, (2) the flatness of the average slope ($S \sim f^{-2/3}$) of the spectrum, and (3) the weak temperature dependence of the average slope and overall magnitude of the noise. All of our SQUIDs show this same general behavior; yet, the detailed shape of the spectra, i.e. the position and strength of features, are different in each device. We have also observed similar noise spectra (Figure 5.5) in single resistively-shunted edge junctions which strongly implies that the SQUID noise properties arise mainly from the junctions themselves and are not due to an external source of flux noise.

Similar bumps in the noise spectrum are observed by Rogers and Buhrman in normal metal junctions of comparable size to ours. In fact they show that their spectra at low temperatures are well approximated by a small number of Lorentzian contributions whose origin they attribute to conductance fluctuations caused by the trapping and untrapping of single electrons into localized defect states residing within the tunneling barrier. In contrast, our SQUID spectra cannot be so simply described. Although single Lorentzian features are usually present, some portions of the spectra are nearly linear or slowly curving. Furthermore, we observe a nearly $f^{-2/3}$ background spectra at all temperatures (4-1K). This behavior is unusual compared to the ~1/f spectra most often observed in dc SQUIDs and other electronic devices, although noise spectra flatter than 1/f have previously been reported in dc SQUIDs having much larger junction areas (Wellstood et al., 1986, Carelli and Foglietti, 1983, Ketchen and Jaycox, 1982). We have not yet determined whether all of the observed background noise comes from a superposition of the same type of electron trapping events responsible for the distinct Lorentzian

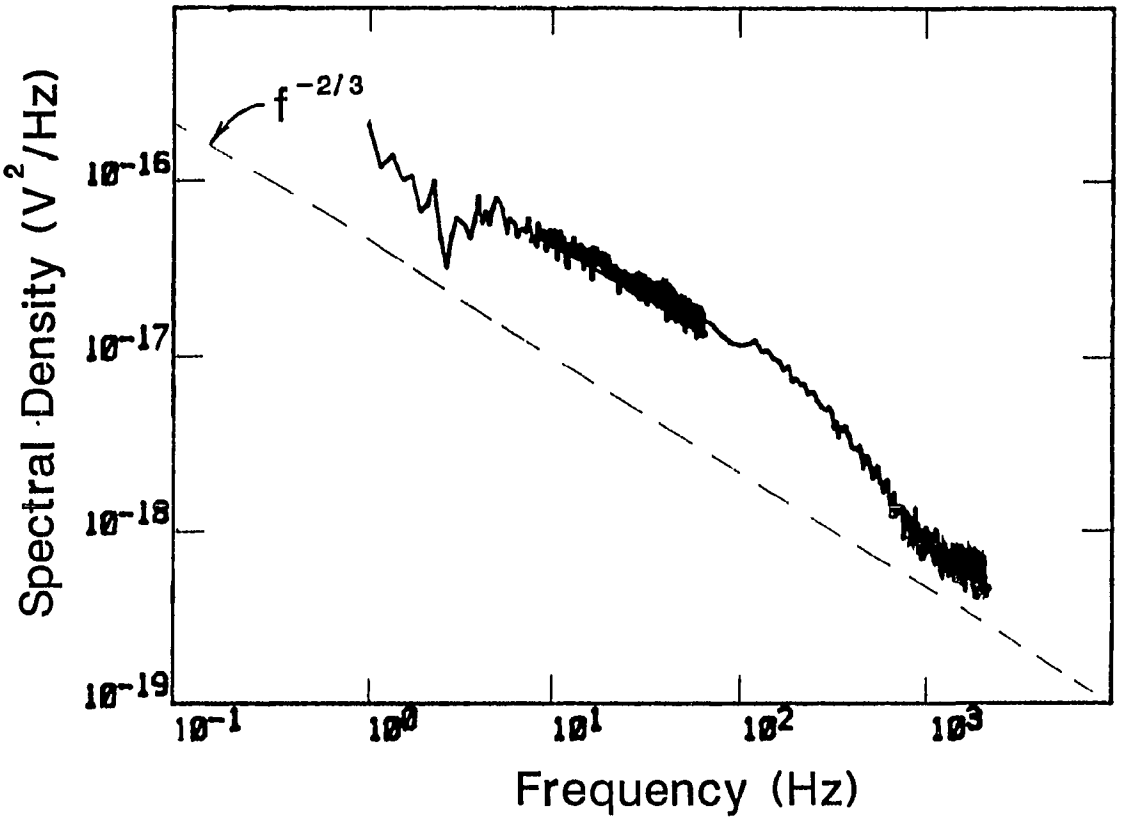

Figure 5.5 - Voltage noise spectrum of an RSJ.

features, but there is strong evidence that it does arise from the junctions.

5.5 Direct observation of single electron trapping

When the Lorentzian features are most prominent, the real-time voltage noise across the SQUID shows discrete switching behavior (Figure 5.6a) which we attribute to single electron trapping and untrapping events. In most cases, the switching is superimposed on a meandering 1/f-like background voltage; but in some instances, it completely dominates the noise. The dependence of the switching amplitude on SQUID parameters, bias conditions and location within the barrier is discussed below, while the microscopic nature of the trapping site is considered in section 6.4. Similar voltage switching due to electron trapping has been reported in 1-d MOSFETs (Ralls et al., 1984) as well as in small area tunnel junctions (Tesche et al., 1985, Rogers and Buhrman, 1985). In a 1-d MOSFET, the charging and uncharging of the interface trap can drastically alter the scattering of the electrons moving through the narrow conduction channel, while in a normal metal tunnel junction, the charged trap blocks conduction through a small region about the trapping site. In a Josephson junction, the dominant effect of the charge trapping is to raise the local barrier for pair tunneling which lowers the junction critical current. Our junctions are small enough that the fractional change in critical current, which varies inversely with junction area, results in an easily observable change in voltage. A fluctuation ΔI_c in the critical current of one junction produces a sizable change in voltage across the SQUID given by

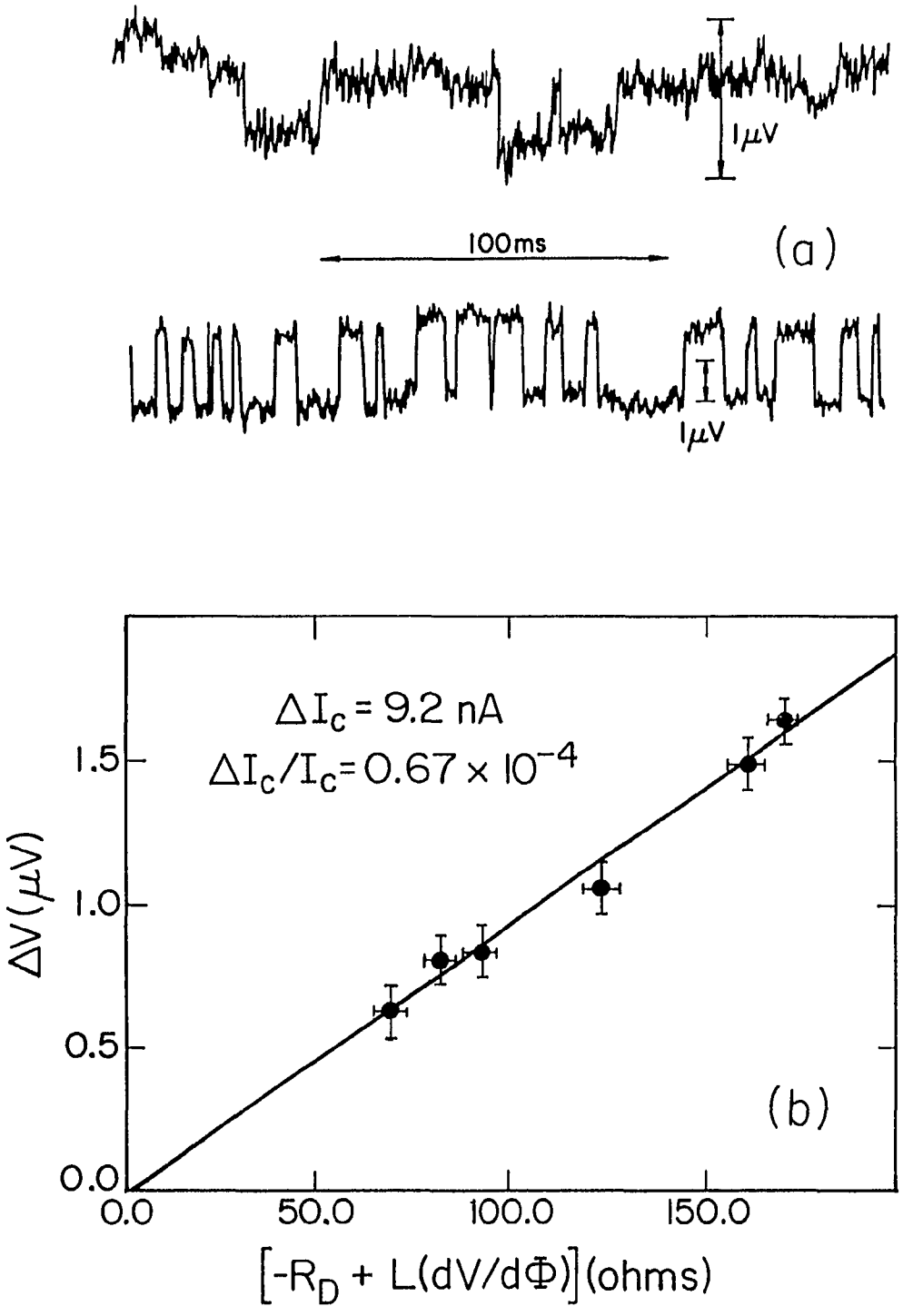

Figure 5.6 - (a) Real-time SQUID voltage noise showing discrete switching events. (b) Amplitude of voltage switching as a function of SQUID bias.

$$\Delta V = \left[\left(\frac{\partial V}{\partial I_c}\right) + \frac{1}{2I_c}\left(\frac{\partial V}{\partial \alpha}\right)\right] \Delta I_c$$

$$\approx \left[-R_D + L\left(\frac{\partial V}{\partial \Phi}\right)\right] \Delta I_c \qquad (5.8)$$

where $\alpha = (I_{c1} - I_{c2})/2I_c$ is the asymmetry in the critical currents of the two junctions. The first term results from the change in total critical current and scales with the dynamic resistance R_D; the second term arises because the change in critical current of one junction unbalances the distribution of applied bias current, linking a flux through the SQUID loop which produces a voltage change proportional to the transfer function $\partial V/\partial \Phi$. By measuring the voltage pulse height, ΔV, for different bias conditions (Figure 5.6b), the change in junction critical current can be determined. For most of the points, the two terms in (5.8) contribute nearly equally because the dynamic resistance and the transfer function scale together so that $R_D \approx L(\partial V/\partial \Phi)$ is satisfied. To insure that the switching is not proportional to R_D or $(\partial V/\partial \Phi)$ alone (i.e. a real flux noise), a few of the measurements were performed far from optimum bias where only one of the terms was large. A more dramatic effect of the bias dependence can be observed by noting that R_D is an even function of the bias flux while $(\partial V/\partial \Phi)$ is odd. Therefore, the bias flux can be readjusted so that R_D remains the same but $(\partial V/\partial \Phi)$ becomes opposite in sign. The two terms in (5.8) then cancel and the switching is seen to completely disappear. It is even possible to determine which of the junctions the trap is located in by this method. Hence, the large phase space of bias conditions allows one to conclusively identify the voltage switching as arising from critical current fluctuations. In

addition, the total change in critical current obtained from Figure 5.6b yields an estimate of the trap size. Assuming that the fractional change in critical current is proportional to the effective area of the charged trap, we find effective trap areas of up to $30x30A^2$, consistent with the Coulomb screening length of the barrier dielectric In_2O_3.

When the switching events dominate the background noise, the voltage forms a complete time record of the trapping behavior. By measuring the time spent in the up and down voltage state and plotting the distribution of these times, we can accurately determine the lifetimes of the two trap states. This technique provides a very precise probe of the trapping kinetics, but a detailed discussion of this topic is reserved for Chapter 6 where measurements of single unshunted junctions will also be presented. The dc SQUID is not an ideal system for such investigations because the discrete switching can only be observed over a somewhat restricted range of temperature and bias conditions where the SQUID signal dominates the system noise. This difficulty is illustrated in Figure 5.7. At maximum transfer function ($V=47\mu V$), the switching completely dominates the noise, but at $255\mu V$ where the transfer function vanishes, the switching cannot be seen in the voltage and only a small bump appears in the noise spectrum. This problem becomes even worse at higher temperatures where the transfer function is smaller.

In some respects, it is surprising that the voltage switching from a single trap can dominate the noise when a large number of similar traps undoubtedly reside within the barrier. One possible explanation is that a small number of well placed traps can cause unusually large voltage switching. If a trap is located in a region where the tunneling barrier

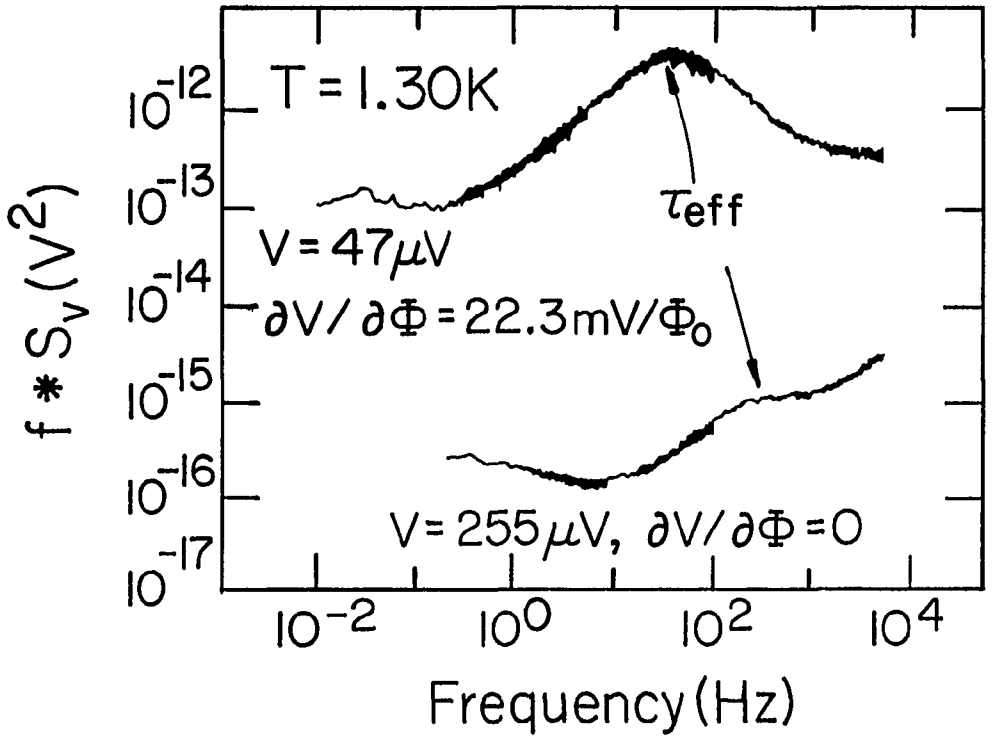

Figure 5.7 - SQUID noise spectrum multiplied by frequency at maximum and zero transfer function.

is thin, the relative conductance change due to charge trapping will be much larger. A variation in barrier thickness of just a few angstroms can produce an order of magnitude variation in local tunneling conductance. Even the depth of the trap in the thin oxide affects the deformation of the tunneling barrier caused by the trapped charge (Schmidlin, 1959). It is therefore possible that the overall noise is dominated by just a few of these strategically located traps. In addition, the noise power is largest when the duty cycle of the switching is 50% (i.e. when the characteristic times are equal). But because the trapping involves a change in net charge, this condition will likely be satisfied in only a few rare instances. Lastly, it should be remembered that the measurement bandwidth is only about two frequency decades. Only when both characteristic times lie within this relatively narrow bandwidth does the discrete switching dominate the noise.

One final comment concerns the effect of thermal annealing on the switching behavior. The switching behavior is stable as long as the SQUID remains at LHe4 temperatures, but warming to room temperature or even 77K can produce dramatic changes even though there are no discernable changes in any of the SQUID parameters. Figure 5.8 (before annealing) shows the nearly ideal Lorentzian noise spectrum of the two-level trap whose voltage noise is shown in the lower time trace of Figure 5.6a. The annealed spectrum was measured under the same bias conditions after warming overnight to 77K. It is not surprising that thermally-activated atomic diffusion can alter or passivate an active trapping site.

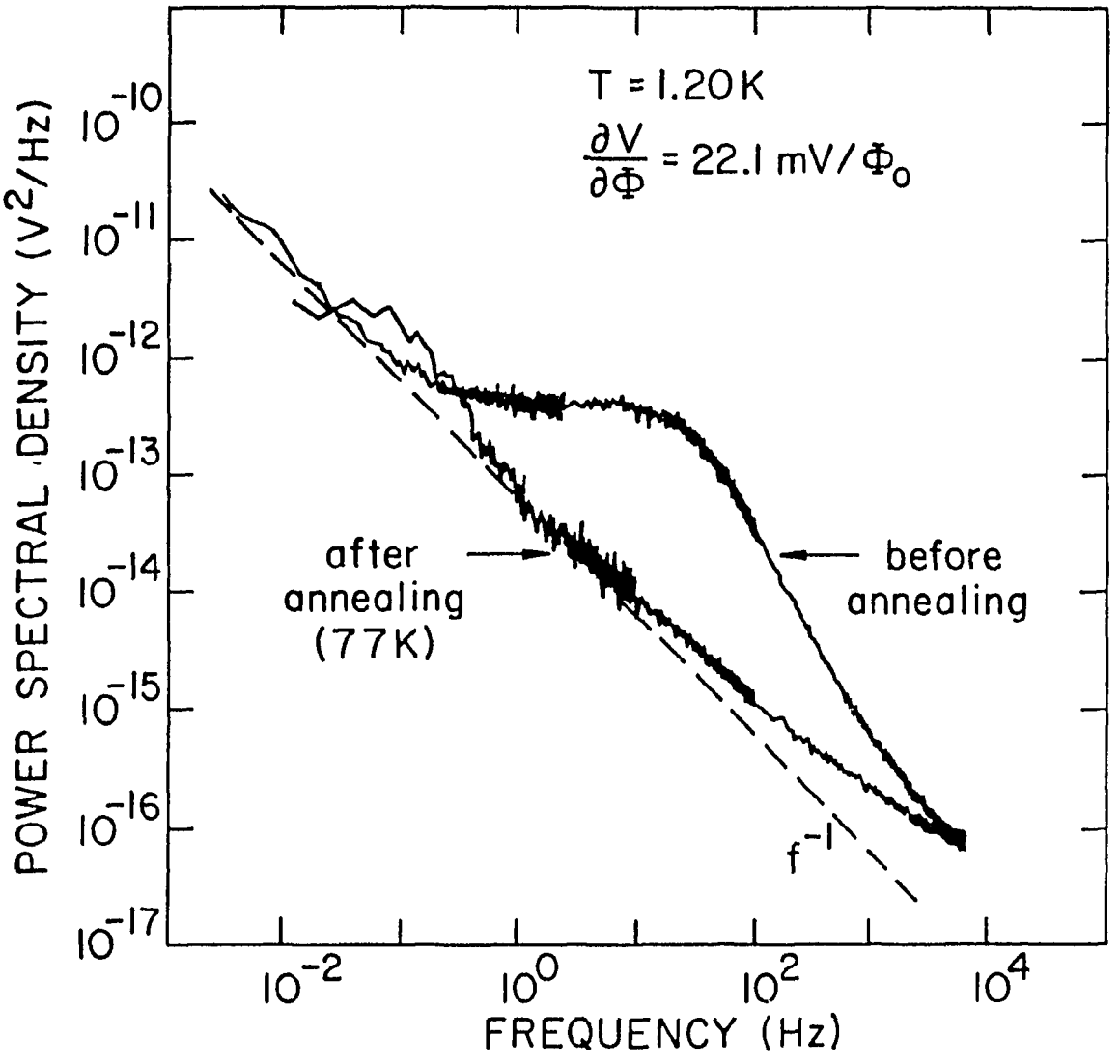

Figure 5.8 - Effect of annealing on discrete voltage switching. The nearly ideal Lorentzian feature disappears upon annealing at 77K.

5.6 $f^{-2/3}$ noise

The question still remains as to the origin of the unusual $f^{-2/3}$ background noise spectrum. The preceding discussion suggests that this background may well be due to charge trapping of lesser amplitude or lesser duty cycle. Another possibility is the motion of microscopic dipole defects in the barrier which can alter the tunneling conductance in a similar way. In addition, flux noise is known to be important in many SQUIDs and can even have a -2/3 spectral slope (Wellstood et al., 1986).

Although the Lorentzian features in our SQUID spectra undoubtedly arise from critical current fluctuations, it is not obvious that the $f^{-2/3}$ background also comes from the junctions. We therefore studied several single junctions and found that their spectra indeed display similar properties. Furthermore, the magnitude of the critical current noise deduced from the junction measurements is sufficient to account for at least half of the observed SQUID noise. The SQUID noise due to critical fluctuations alone can be approximated by

$$S_\Phi(f) = \frac{1}{2}\left[\left[\frac{\partial V}{\partial I_c}\right]_I^2 + \frac{1}{I_c^2}\left[\frac{\partial V}{\partial \alpha}\right]_I^2\right] \frac{S_{I_c}(f)}{(\partial V/\partial \Phi)^2} \qquad (5.9)$$

where S_{I_c} is the critical current noise of a single junction. This predicts a SQUID flux noise of slightly under $2\times10^{-11}A^2/Hz$ at 1 Hz while the observed flux noise is 1×10^{-11}-$6\times10^{-11}\Phi_o^2/Hz$. These observations strongly suggest that our SQUIDs are dominated by critical current fluctuations; however, we cannot rule out the possibility of a significant flux noise component. Although the junction spectra tend to

be flatter than 1/f, they often display stronger frequency dependence than the SQUID spectra and show more regions where the noise is nearly 1/f.

Power spectrum measurements do not provide much direct evidence for the microscopic origin of the noise, but the DDH model can sometimes be applied to extract useful information. Figure 5.9 shows the flux noise, S_Φ, for one SQUID at several temperatures. Strong Lorentzian features are absent from this particular device which allows the background noise to be studied. The spectrum is multiplied by $f^{-.60}$ so that changes in slope as well as magnitude can be readily seen. Because the slope is always much flatter than 1/f, the DDH relation (5.7) predicts that the magnitude of the noise should increase sharply ($\sim T^{-6}$ or stronger) at low temperatures. This may seem counterintuitive, but the extreme flatness of the spectrum implies (in the DDH picture) that there are many more fluctuators at high frequency which will move to lower frequency and strongly increase the noise as the temperature is lowered. The observed weak temperature dependence of the noise slope and magnitude over a relatively wide temperature range suggests that the basic assumption of the DDH model-- thermally-activated kinetics-- does not hold here; instead, it is likely that at these temperatures the fluctuations obey tunneling kinetics. This is consistent with the conclusions of Rogers and Buhrman (1986) who observed a transition from thermally-activated to tunneling kinetics in their junctions at ~15K. It is noteworthy that an $f^{-2/3}$ noise spectrum has been observed in several dc SQUIDs and in spin glasses below 4K (Reim et al., 1986); yet such a flat spectrum is rarely seen at higher temperatures. Although a general tunneling kinetics model

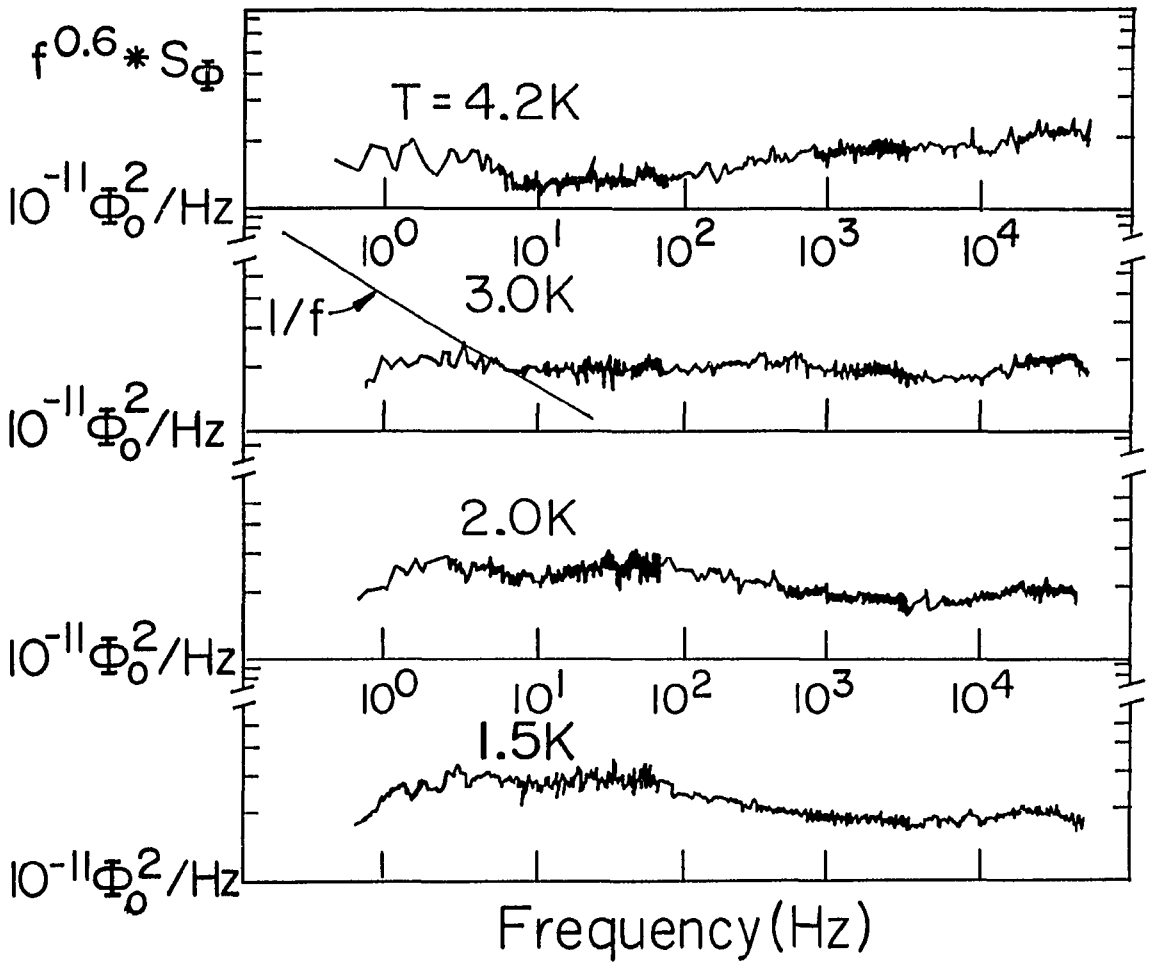

Figure 5.9 - Frequency dependence of the quantity $f^{0.6}*S_{\Phi}$ at four temperatures. Note that the slope is much less than 1/f everywhere.

of low frequency noise does not exist, it would be very interesting if flat noise spectra were intrinsic to such a model, at least in these specific systems.

5.7 Consequences for practical devices

Although small-area tunnel junction SQUIDs have proven to be such interesting systems for studying 1/f noise, the consequences of these results for practical devices should not be overlooked. We have determined that the noise in our SQUIDs arises predominantly from an $\sim f^{-2/3}$ critical current fluctuation due to electron trapping within the tunneling barrier. This knowledge can be used to improve the low frequency performance in several ways: 1) the properties of the barrier can be improved so that the noise as well as the signal properties are optimized. In particular, the density of active electron traps can be reduced by growing more perfect barriers or by adding contaminants that passivate the trapping sites. Epitaxially grown barriers have not yet shown promising results, but the very low 1/f noise in some IBM SQUIDs (Tesche et al., 1986) has been attributed to passivation of the electron traps by trace amounts of carbon in the Nb_2O_5 barriers. 2) A clever bias modulation scheme implemented by Foglietti et al. (1986) can be used to suppress noise due to critical current fluctuations. The principle behind this technique is related to the bias dependence of the discrete voltage switching described in section 5.5 where the voltage switching can be made to disappear by reversing the polarity of the bias flux. A factor of three improvement in performance was obtained using SQUIDs which were very low noise to begin with. This technique can also be used

to estimate the individual contributions due to flux noise and critical current noise.

The primary consequence of the $f^{-2/3}$ frequency dependence is that the low frequency crossover to the white noise regime extends out to about 1 MHz which is considerably higher than for any other SQUID. To realize the full sensitivity of the device, it must be operated above the crossover which makes operation in feedback mode more difficult. On the other hand, the noise at very low frequencies is quite good. Many SQUIDs show a flux noise of about $10^{-10}\Phi_o^2$/Hz at 1 Hz, while our SQUIDs are typically three times quieter than this. This is unlike most electronic devices (e.g. a transistor) where the low frequency performance is seriously degraded as device dimensions are reduced. In a SQUID, the increased noise is compensated by improved flux sensitivity, although eventually, the sensitivity may itself become limited by intrinsic quantum processes (e.g. zero point noise rounding of the I-V (Koch et al., 1981)) at low enough temperatures.

Chapter 6

KINETICS OF SINGLE ELECTRON TRAPPING IN DC SQUIDS AND JOSEPHSON JUNCTIONS

6.1 Introduction

The low frequency noise properties of small area tunnel junctions have recently attracted much attention (Rogers and Buhrman, 1984 and 1985, Wakai and Van Harlingen, 1985 and 1986, Tesche, 1985). Unlike larger systems where the low-frequency noise exhibits a rather featureless 1/f power spectrum, tunnel junctions can be made so small that the discrete nature of the underlying microscopic processes becomes apparent in the noise. This was first demonstrated by Rogers and Buhrman (1984) who showed that the noise power spectra of their junctions were dominated by a small number of Lorentzian features arising from the trapping and untrapping of single electrons into localized defect states within the tunneling barrier. The trapped electron alters the junction conductance by charging a small region about the trapping site, thereby blocking conduction through this channel; hence, the voltage noise contributed by one such trap displays a series of discrete switching events, resembling a random telegraph signal, characterized by electron emission and capture times. Because the trapping couples to the junction voltage in such a simple, distinctive fashion, it is possible under certain favorable conditions to directly observe the switching behavior of one or several of these traps. This affords the rare opportunity to study the behavior of a single fluctuator in great detail.

This chapter presents very precise lifetime measurements of charged defect states in very small area Josephson junctions under various temperature and voltage bias conditions. The lifetimes show a weak temperature dependence (below 4K) consistent with previous findings that the trapping process displays tunneling kinetics at low temperatures. In contrast, the emission and capture rates are both enhanced by increasing the voltage bias, regardless of polarity. We propose a simple model to explain this behavior. In addition, the noise does not always exhibit a simple superposition of random telegraph switching when several traps are active at the same time; instead, interactions between the traps can conspire to produce a voltage noise that displays series kinetics. These observations show that the low-frequency noise of this and perhaps other ultra-small systems cannot always be described by a simple parallel kinetics model. The results described here represent a fuller account of a paper by Wakai and Van Harlingen (1987).

6.2 Kinetics of single electron trapping derived from power spectra

This section reviews the experimental results of Rogers and Buhrman (1984, 1985) who studied the charge trapping in their junctions by following the movement of the Lorentzian spectral features over a wide range of temperature and bias conditions. Much of their analysis is based on a simple model where the transitions between the two trap states are assumed to be governed by the double well potential shown in Figure 6.1. The transition rates between the wells, $1/\tau_1$ and $1/\tau_2$, are deduced from the effective rate, $1/\tau_{eff}$, and the total integrated power, S_1, derived from the spectrum.

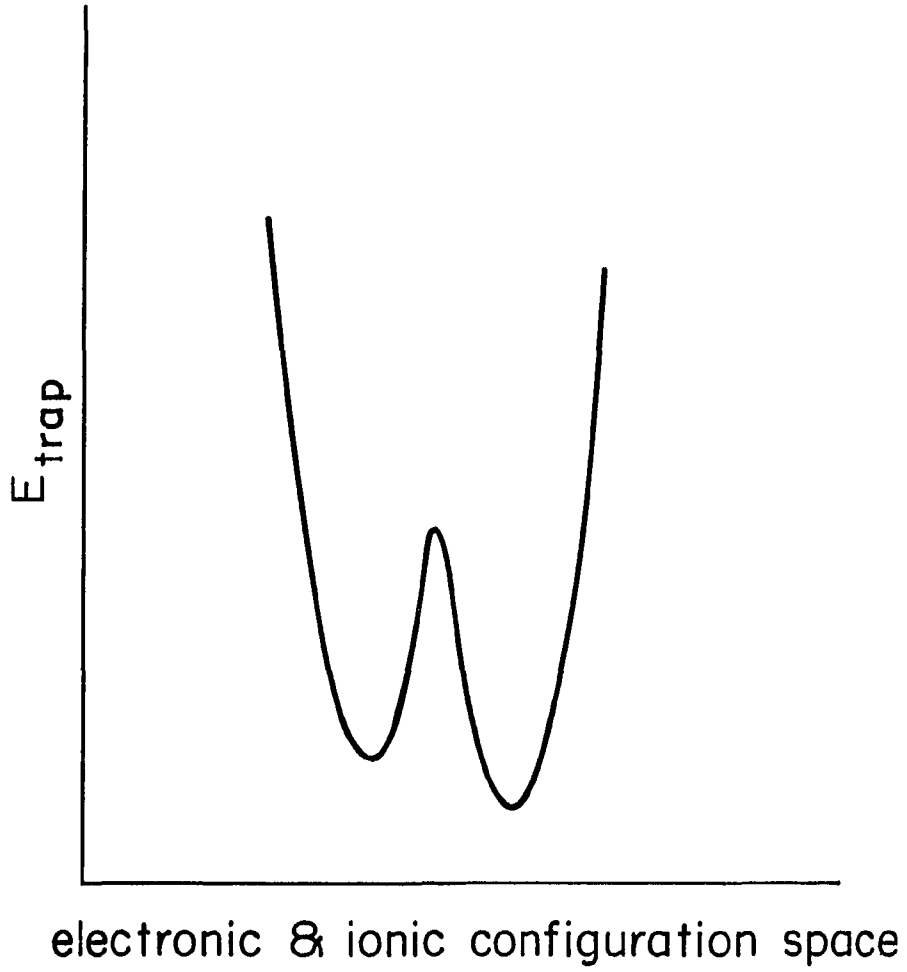

FIgure 6.1 - Double well potential energy model of a two-level trap.

$$1/\tau_{eff} = 1/\tau_1 + 1/\tau_2 \qquad (6.1)$$

$$S_1 = S_o\ \tau_{eff}/(\tau_1 + \tau_2)$$

where S_o is the square of the change in resistance between the two states. The noise is measured as a function of temperature and bias voltage, and the rates, $1/\tau_1$ and $1/\tau_2$, are fit to the sum of a thermally-activated term and a parallel WKB tunneling term

$$1/\tau_i = 1/\tau_{act} + 1/\tau_{tun} \qquad (6.2)$$

where

$$1/\tau_{tun} = 1/\tau_o\ [1 + C(kT/eV)^2]\ \exp -[2(2mE_B/\hbar^2)^{\frac{1}{2}}d(1-\gamma_t eV)] \qquad (6.3a)$$

and

$$1/\tau_{act} = 1/\tau_o\ \exp -[(E_B-\gamma_a eV)/kT] \qquad (6.3b)$$

E_B is the potential barrier height and the rates are assumed to have an exponential bias dependence described by γ_t and γ_a. In equation (6.3a), d is the tunneling distance between the wells and m is the mass of the tunneling particle.

Several important features of the fluctuation kinetics were established: 1) at high temperatures, the kinetics are thermally activated with attempt frequencies, $1/\tau_o$, in the range 10^9-10^{13} s^{-1} and activation energies of 10-150meV, 2) below 15K, the kinetics show a weak temperature dependence consistent with WKB tunneling, 3) the bias dependence is weak in the thermally-activated regime but becomes much stronger at low temperatures, and 4) the parameter $m^{\frac{1}{2}}d$ is consistent with an ionic mass and a tunneling distance of a few angstroms which implies

that ionic motion is important in the trapping.

A Bell Labs group (Ralls et al., 1984, Howard et al., 1985) studying interface traps in very narrow channel MOSFETs arrive at similar conclusions. The trap lifetimes are thermally activated (T>20K) and they show that the kinetics are more sensitive to the temperature of the lattice than the electrons.

6.3 Fabrication of ultrasmall Josephson junctions

Unshunted (underdamped) Josephson junctions are used for most of the measurements reported in this chapter. When the junction is biased at $V>2\Delta/e$, the observed voltage switching is due to fluctuations in the quasiparticle or normal resistance (Figure 6.2a) as opposed to critical current fluctuations. The charge trapping affects the quasiparticle as well as the pair tunneling by increasing the normal resistance and lowering the junction critical current in such a way that the parameter I_cR remains constant (section 3.3). Unlike voltage switching in SQUIDs, the switching amplitude is insensitive to temperature and it increases linearly with the bias current; this allows the trapping to be studied over a wide range of temperature and bias conditions. But because of the hysteresis below $V= 2\Delta/e$, SQUIDs and RSJs must still be used to study the low voltage regime (Figure 6.2b). A simple model for the bias dependence presented in section 6.7 predicts that the noise will show important differences for biases above and below $2\Delta/e$.

The junctions are fabricated with the same materials and techniques as described in chapter 3. Optimum device parameters are determined by the following considerations: 1) the relative contribution of a single

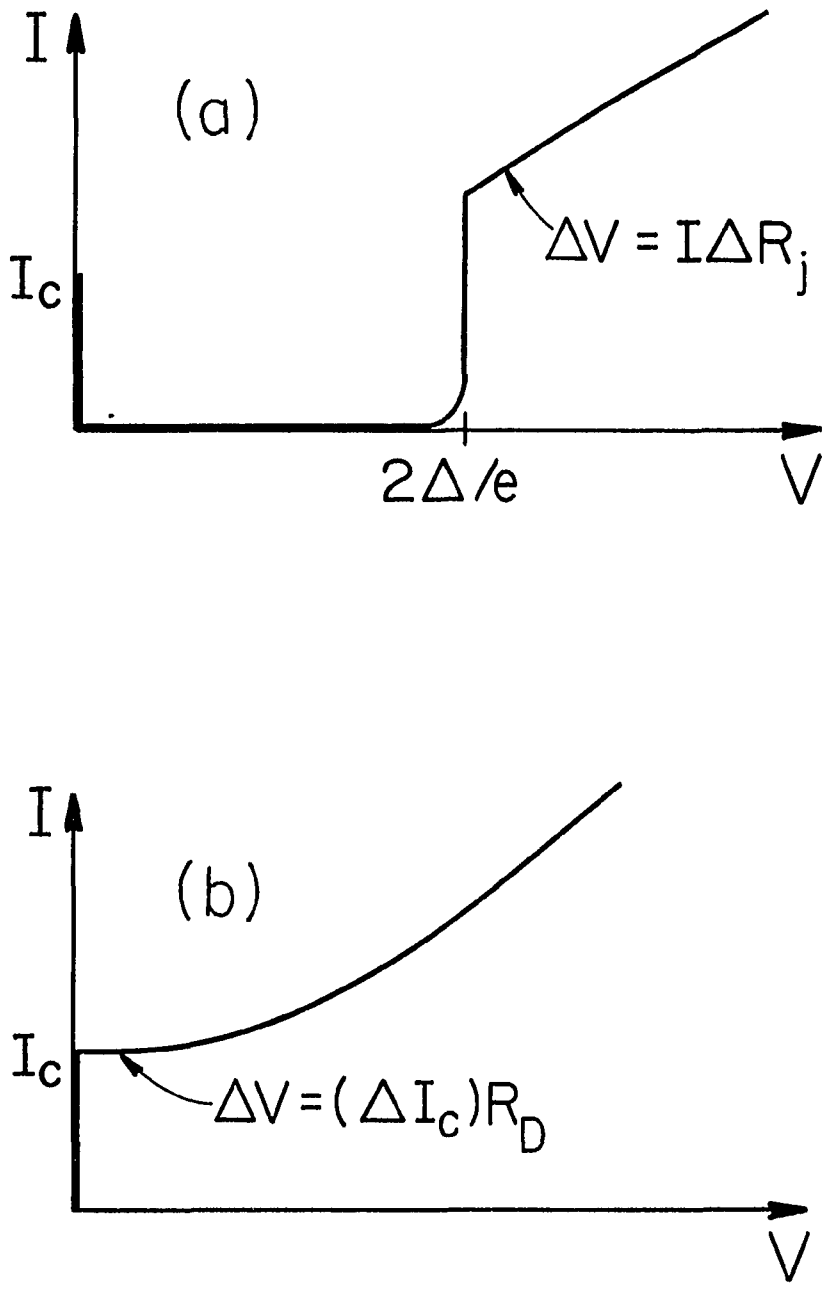

Figure 6.2 - Current-voltage characteristic of (a) unshunted and (b) resistively-shunted junctions showing typical bias points.

trap varies inversely with junction area, so very small areas are needed to resolve individual traps and 2) the overall signal scales with the junction resistance so large resistances help overcome the system noise. The Pb alloy junctions studied have areas of $<0.05\ \mu m^2$ and normal state resistances on the order of 1kΩ. Fabrication of single junctions is much easier than SQUIDs for which very precise control of device parameters is required in order to match the junctions and satisfy the optimization conditions.

6.4 Nature of the trapping site

There is strong evidence (Magerlein, 1981) that the tunneling barrier of Pb-alloy junctions is a Schottky barrier formed at the interface of the degenerate semiconductor In_2O_3 and the Pb counterelectrode. The barrier shape is approximately trapezoidal in contrast to the rectangular barrier of most junctions. Although we cannot determine the microscopic origin of the traps from our measurements, a few observations are worth noting: 1) it is often assumed that the trapping site is neutral and therefore the high resistance state of the junction results when the electron becomes trapped; however, we cannot rule out that the trapping site has a net positive charge which is neutralized by electron capture. 2) The trap energy must be near the Fermi energy, otherwise it will always be either filled or empty and switching will not occur; therefore, we are observing a deep level trap of some sort, most likely a structural defect. A good candidate often found in In_2O_3 barriers is an oxygen vacancy. 3) Nearly every characteristic of the barrier-- its composition, structural and

electrical properties-- is expected to influence the nature and density of the traps present as well as their switching behavior. The dielectric screening will be particularly important in stabilizing the charged state of the trap and in determining the interactions between neighboring traps. Even the surface properties of the base electrode will influence the growth and microscopic structure of the barrier. 4) In spite of this complex picture, charge trapping has been observed in several types of junctions, in 1-d MOSFETs, and even in silicon surface states using scanning tunneling microscopy (Koch and Hamers, 1987). Furthermore, many aspects of the trapping kinetics appear to be similar in all these systems even though the detailed nature of the defects present is certainly different. A likely explanation for this is that the experiments observe only the small subset of defect traps which can be accurately modeled by the simple double well potential described above and which have a particular range of model parameters.

6.5 Direct lifetime measurements

When the discrete switching events due to electron trapping dominate the low-frequency noise, the real-time voltage forms a complete time record of the trapping behavior. In order to further study the trapping, we have developed a technique to detect the occurrence of a switching event and measure its amplitude and duration. The voltage is digitally sampled and the following algorithm is used to detect and record switching events: each new voltage is compared to a moving average of the last (to be definite) eight points. If the difference exceeds a specified threshold voltage, then a voltage switching event has likely

occurred. The average of the eight points before and after the event are then compared to determine the height of the voltage switch. The height must exceed a second threshold level in order to be counted as a valid switching event. If it does, then the step height and the time since the last event is recorded. This cycle is repeated until sufficient data (~5000 events) is collected. The real-time voltage, V(t), is continuously displayed on a storage monitor and each recorded switching event is designated by a marker which appears on the monitor and allows the experimenter to verify that the switches are being properly detected. The threshold voltages are set large enough to discriminate against the background noise, but small enough to allow the switching events to be detected. This method is found to work reasonably well even when the background noise is comparable to the switching height.

Since the algorithm described above runs in real time, the voltage sampling frequency is limited to about 7kHz. To obtain higher rates, we use a fast digital-to-analog converter (200kHz) which can DMA (direct memory access) the data into memory. About 48,000 voltages are first stored and then analyzed using a similar algorithm to the one described above.

By plotting a histogram of the recorded times (Figure 6.3), we find that the times are exponentially distributed which implies a time-independent transition probability out of each trap state; the characteristic lifetime of each state can then be determined from the histogram slope. As seen in Figure 6.4, a variety of behavior is observed. The histogram in Figure 6.4a corresponds to the simplest case where a single trap is active. The times spent in each state are

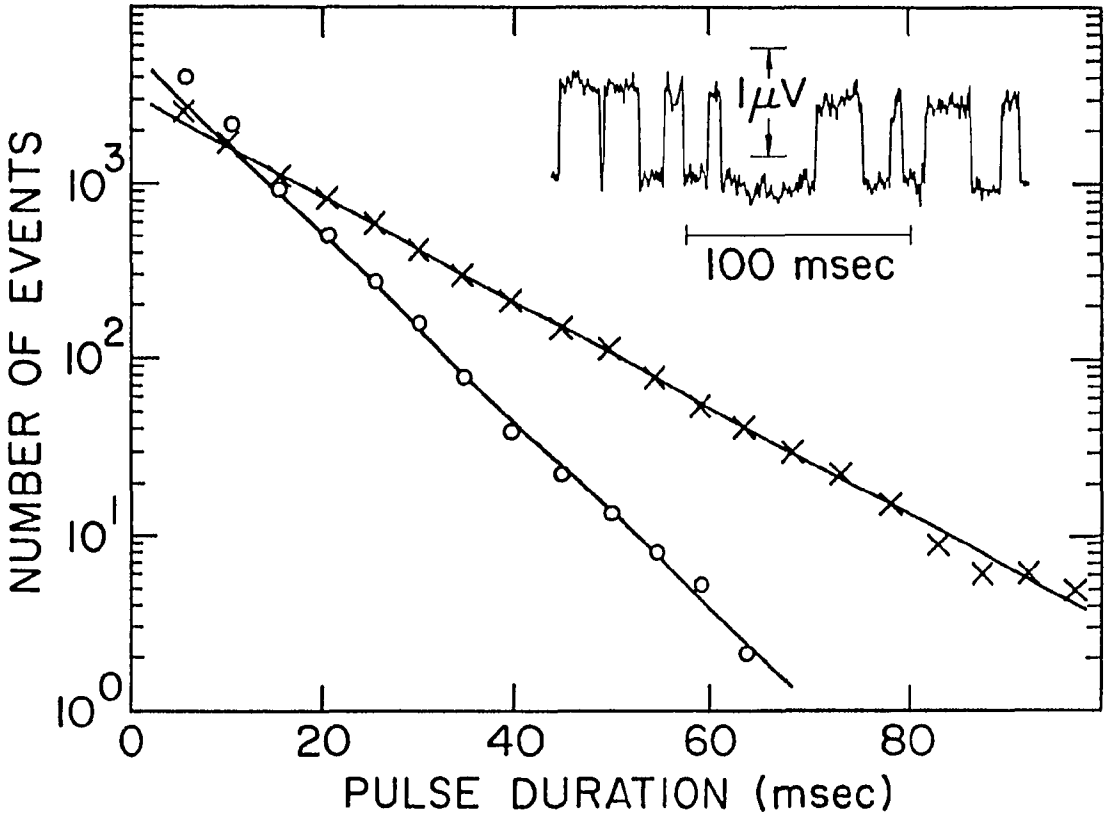

Figure 6.3 - Histogram of times spent in up and down voltage state for a two-level trap.

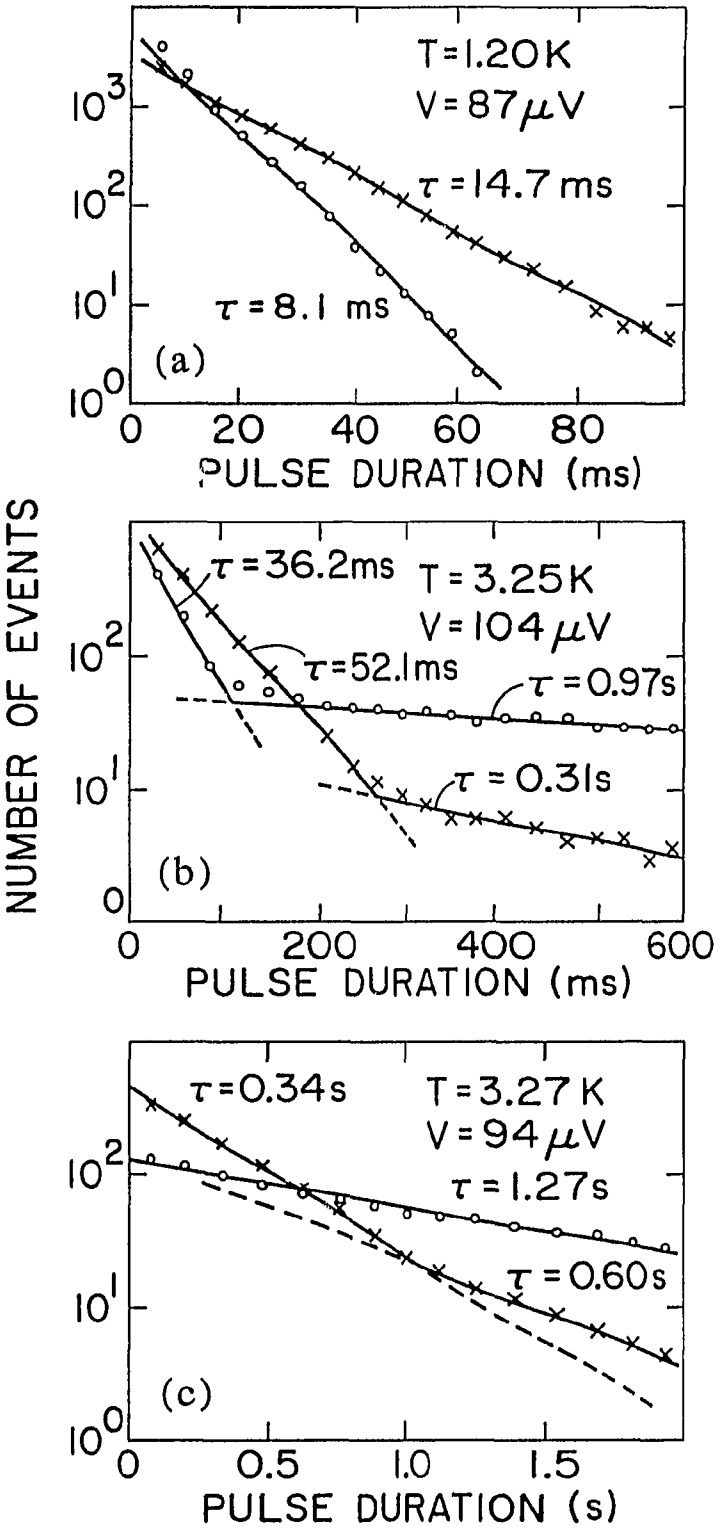

Figure 6.4 - Examples of switching behavior seen in histograms.
(a) Single trap active. (b) Two traps active. (c) A three state system.

exponentially distributed with lifetimes of 8.1ms and 14.7ms for the up and down state respectively. We have observed traps with lifetimes throughout the range over which we can measure them (1ms-10s) and having a wide range of duty cycles, $\tau_u/(\tau_u+\tau_d)$ (u= up state, d= down state) . Often, more than one trap is present as in Figure 6.4b. The lifetimes for each trap can still be resolved from the histogram, provided they are not too similar. More complicated switching has also been observed in some samples. Figure 6.4c shows a histogram indicative of an active three-level system, having one lifetime in the up state and two characteristic times in the down state. This can occur either if a single trapping site has three distinct ionic configurations, or, for example, if a trapped electron has a slow interaction with another two-level system resulting in two characteristic times for the trapped state. Direct evidence for trap interactions is presented in section 6.9.

In the next two sections, the population kinetics of individual two-level traps are studied as a function of temperature and bias conditions. For these measurements, the voltage switching is dominated by just the one trap under study as in Figure 6.3. When switching from two or more traps is superimposed, it is necessary to distinguish events from different traps which is often difficult or impossible to do. Interpretation of the switching is particularly ambiguous when interactions are present between traps as discussed in section 6.9. Statistical analysis may be useful for extracting information for these more complicated cases. The presence of simple two-level switching can usually be established by inspection of the voltage; however, some data

analysis can be performed to improve the accuracy of the results. For a single two-level trap, the sequence of switches should simply follow: up, down, up, down, etc. Events which violate this pattern are rejected. Most violations occur because some of the times are too short to be detected even though the sampling rate is always set much faster than the characteristic switching frequency. For the best data, less than 2% of the events are rejected, but 2%-10% is typical. We estimate the uncertainty in the lifetimes to be about 5%. In contrast, the lifetimes determined from spectra are not nearly as accurate. Only the parallel rate, $1/\tau_{eff} = 1/\tau_1 + 1/\tau_2$, is directly measured and the individual rates are deduced from the bias dependence of the integrated noise power.

6.6 Temperature dependence of the lifetimes

Figure 6.5a shows the temperature dependence (below 4K) of lifetimes for a typical trap at two different bias voltages. Below about 2.5K, the times are nearly constant, indicating that the transitions between the two states occur by tunneling. At higher temperatures, it is expected that the transitions will become thermally-activated and the times should then decrease as $\tau \sim \exp-(E_a/kT)$ where E_a is the activation energy. Note that the up time at 7mV shows a slight increase with temperature above 2.5K. This behavior is less often observed and we do not expect it to persist at higher temperatures. Figure 6.5b shows the temperature dependence of the quantity τ_u/τ_d derived from the times in Fig. 6.5a. The flattening below 2.5K implies that the trap remains active even as the system approaches zero temperature. Above 2.5K, the temperature is effective in changing the duty cycle of the trapping. The simplest and

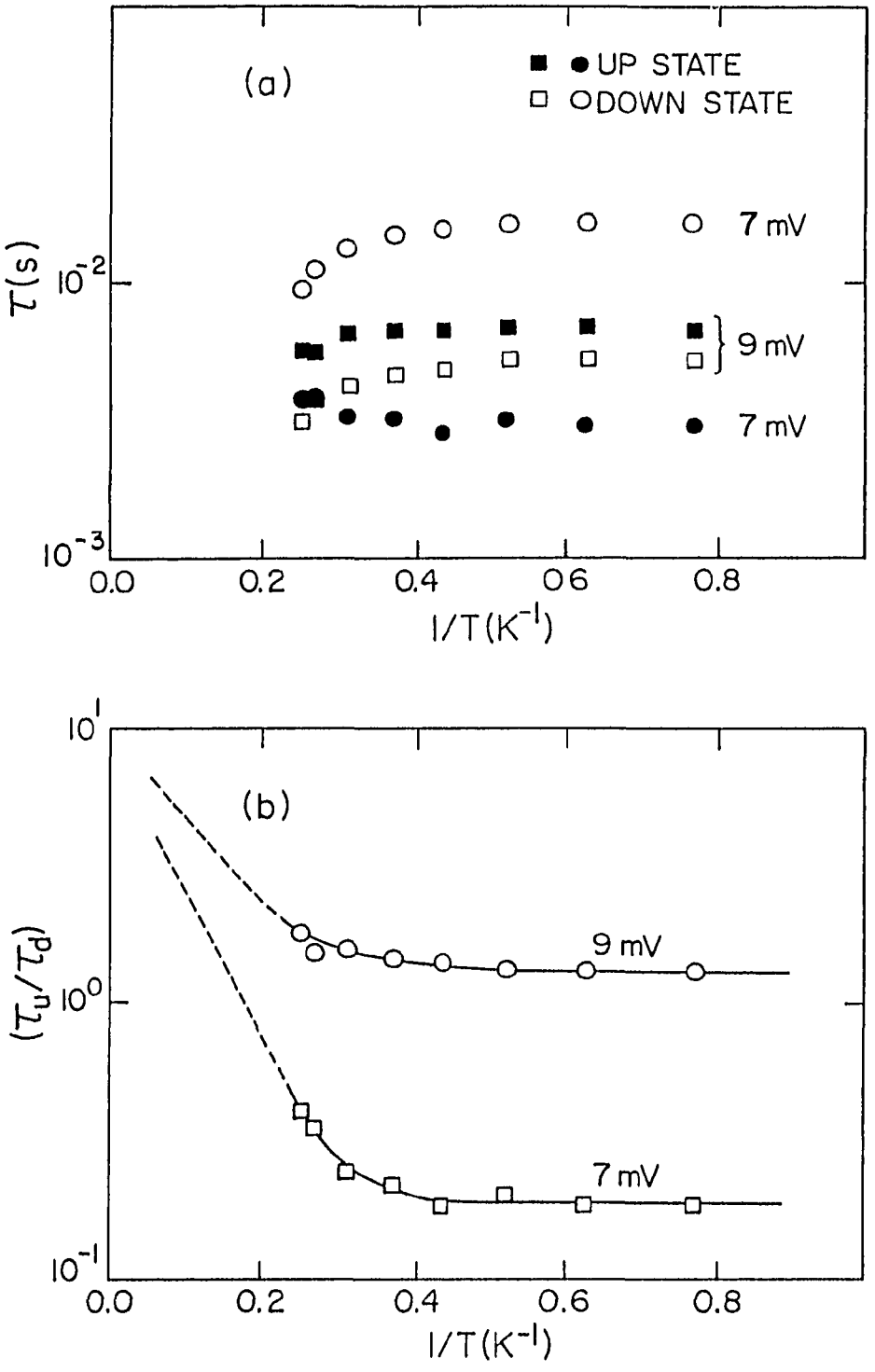

Figure 6.5 - (a) Trap lifetimes versus temperature at two bias voltages. (b) Ratio of the lifetimes versus temperature.

most general model for describing the trap thermodynamics is a double-well potential in which the wells represent two distinct electronic-ionic configurations. In the thermal regime, the model predicts

$$\tau_u/\tau_d = (N_u/N_d)\ \exp[(E_u-E_d)/kT] \qquad (6.4)$$

where E_u, E_d are the energies of the two wells and N_u, N_d are the degeneracies which are related to the entropies of each state. Although we have insufficient high temperature data to accurately determine the quantities N_u/N_d and E_u-E_d, it is clear that an extrapolation of the measurements to high temperature predicts $N_u/N_d>1$; therefore, the trap spends more time in the up (charged) state than in the down (uncharged) state as the temperature increases. This conflicts with our expectation that $N_u/N_d \to 1$ as $T \to \infty$ (the large degeneracy of the conduction electrons should dominate both states) and suggests that a more complex model of the trap system may be required. In particular, we present evidence in the next section that a nonequilibrium model is needed to adequately describe the trapping behavior at large voltages.

Because of the large bias voltages used for these measuremenis, it is also important to consider possible effects due to self-heating. Accordingly, the following precautions were taken: 1) the normal resistance of the junctions was made as large as possible (~1kΩ) and the and the power dissipation was limited to about 100W/cm^2, 2) the substrate is immersed in a helium bath in order to obtain as much cooling of the films as possible, and 3) edge junctions are used to provide efficient removal of heat and excess quasiparticles from the junction

area as discussed in section 3.4. A rough estimate of the heating implies that it will be significant in conventional overlap junctions, but is inconclusive for the case of an edge junction. Unfortunately, it is difficult to directly determine if heating is present; however, we observe that the temperature dependence of the lifetimes does not show a strong dependence on the level of power dissipation. Although it does become weaker at larger biases, the behavior is quite consistent with the WKB tunneling prediction (see section 6.8). We also note that the Kapitza resistance (thermal boundary resistance to the liquid helium) increases by four orders of magnitude below the superfluid transition (~2.1K), yet we do not see any change in the lifetimes upon passing through the lambda point as expected if heating were present.

6.7 Bias voltage dependence of the lifetimes

Figure 6.6 shows the voltage bias dependence of the lifetimes for three different traps which display a wide range of behavior. Several general trends are noted: 1) the times are approximately exponential in the bias voltage, 2) most often, the lifetimes decrease as the bias increases in magnitude (i.e. the bias dependence is roughly an even function), 3) no sharp structure is ever observed on a semilog plot; the times often show a slight curve or a small abrupt change in slope, but the bias dependence is monotonic within experimental accuracy, 4) the bias is often effective in changing the duty cycle of the trapping, and 5) the strength of the bias dependence varies widely between traps, although lifetimes which increase with increasing bias typically show

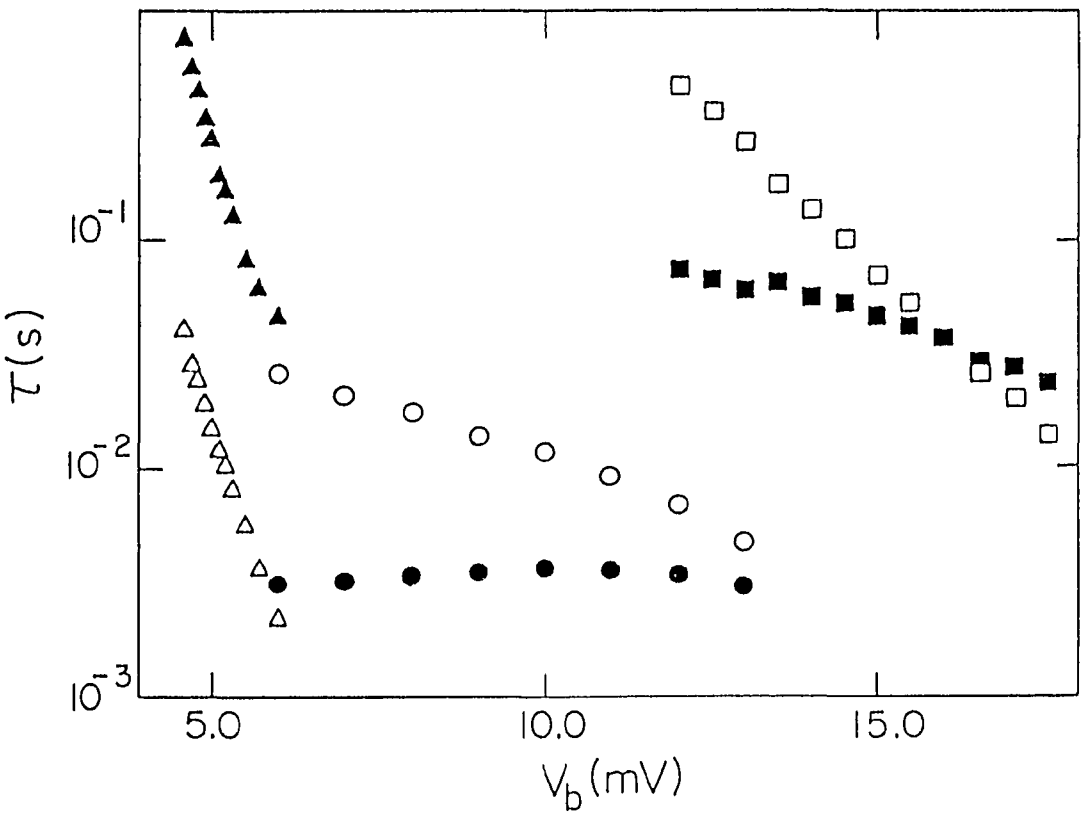

Figure 6.6 - Voltage bias dependence of the up (solid symbols) and down (open symbols) for three traps at 4.2K

only a weak increase. In order to extract quantitative information from the data, it is necessary to model how the bias affects the trap. Since the times generally decrease as the magnitude of the bias increases, this suggests that the dominant effect is to simply shift the energy of the trap by an amount proportional to the distance of the trap from the interface. A semiconductor representation of the junction is shown in Figure 6.7. When a large bias is applied, the trap lies below the Fermi energy of the right electrode, but above the Fermi energy of the left electrode. More electrons are now available on the right to fill the trap and more holes on the left can empty the trap; hence, the emission and capture times both decrease. This implies that the electrons predominantly tunnel into the trap from one side of the barrier and exit out the opposite side, in violation of detailed balance. If the bias is reversed, the trap sees more holes on the left and more electrons on the right. The times are generally different for the two polarities, but in both cases are less than the zero bias times. It is significant that both electrons and holes are available to the trap at all temperatures; this allows the trap to remain active even at zero temperature. Therefore, the very weak temperature dependence of the lifetimes may be (at least in part) due to a nonequilibrium effect as opposed to a quantum effect. In contrast, Ralls, et.al. (1984) observe (in MOSFETs) a strong decrease in emission time and a strong increase in capture time as the bias is increased (Figure 6.8). This qualitatively different behavior results because the interface trap must both fill from and empty into the inversion layer. Changing the bias can increase the number of electrons

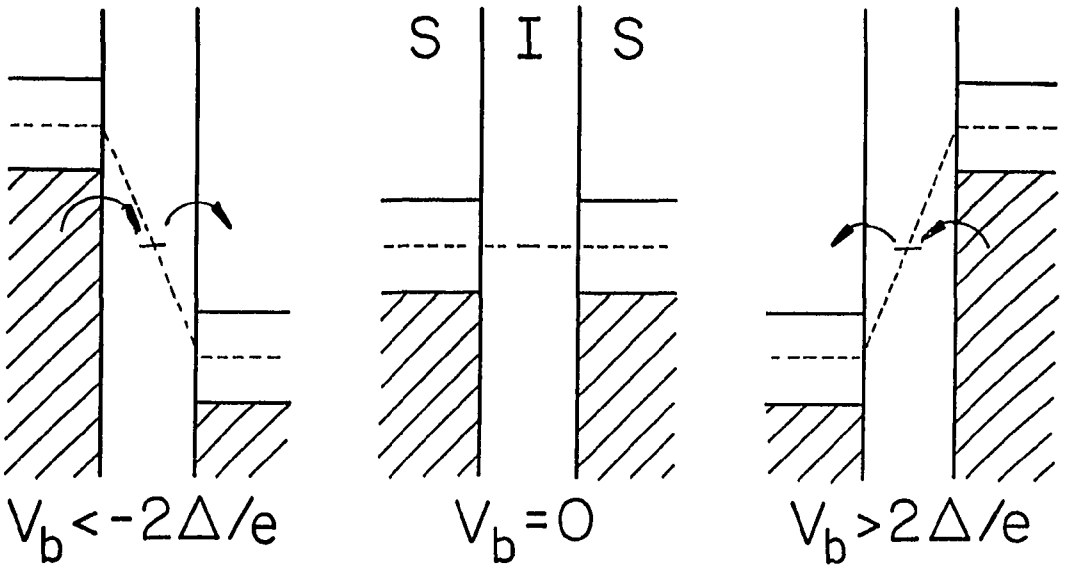

Figure 6.7 - Semiconductor representation of the junction showing the filled states and the trap energy level near the Fermi energy. For small bias voltages, the trap lies within the energy gaps of the electrodes, but a large bias greatly increases the number of available states to the trap.

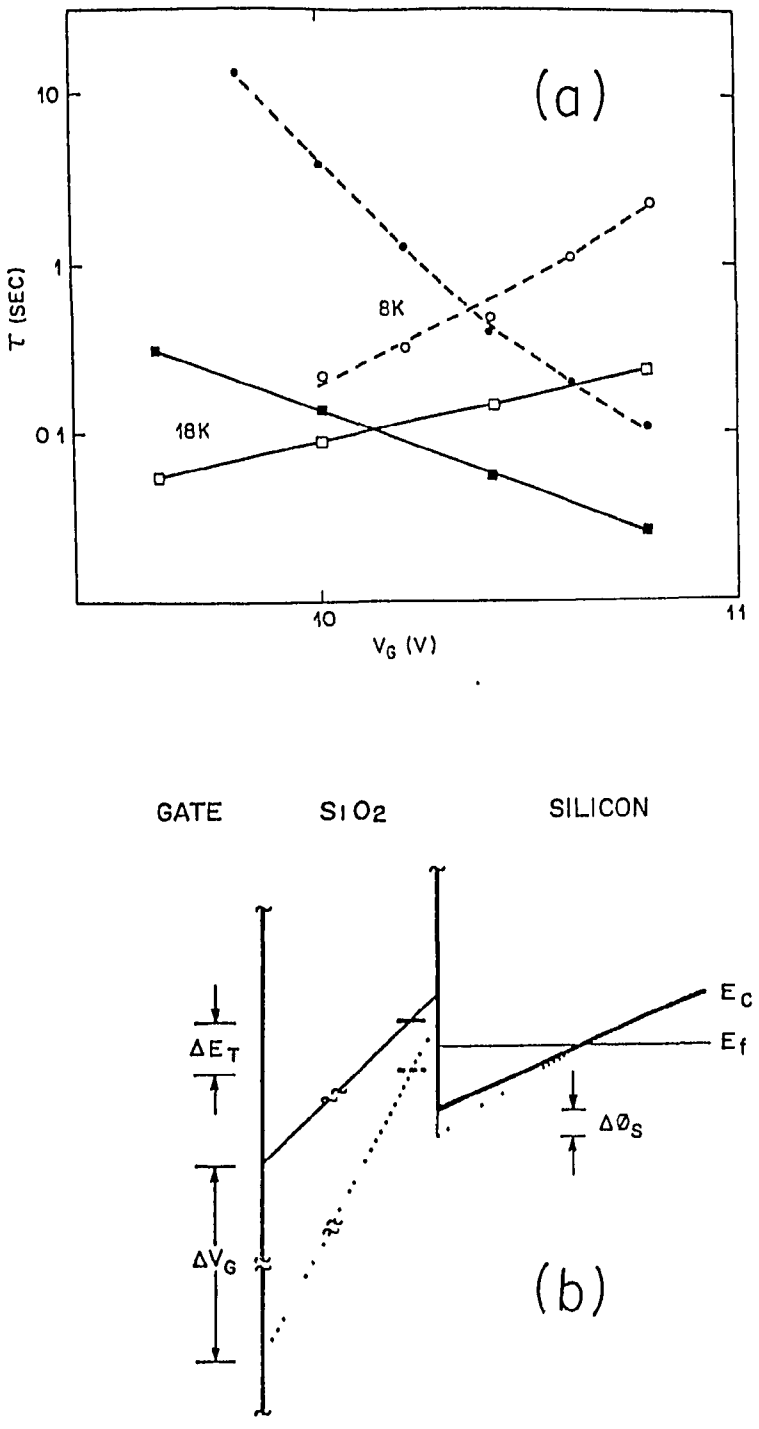

Figure 6.8 - (a) Gate voltage dependence of interface trap lifetimes in 1-d silicon MOSFETs (Ralls et al., 1984). (b) Schematic energy diagram showing the silicon inversion layer, the interface trap energy level, and the effect of the gate voltage.

available to the trap, but only at the expense of depleting the number ofavailable holes.

Evidence for the presence of the superconducting energy gap has also been observed: in some instances, the switching suddenly vanishes below a particular bias voltage, V^*. This can occur if the voltage is decreased so that the energy of the trap lies within the gap of one of the electrodes and the number of states available to the trap would then abruptly decrease. The value of V^* was observed to increase at lower temperatures in a manner consistent with a gap effect. Also note that, in the absence of a gap, both the filling and emptying of traps located near the oxide-electrode interface will be dominated by only one of the electrodes and should therefore display a bias voltage dependence similar to the interface traps of Ralls et al.; yet this behavior is never observed. The presence of the gap prevents this situation from occurring because traps located near an interface will always lie within the gap of the electrode.

It should be noted that although the tunneling events depicted in the semiconductor representation are in one-to-one correspondence with the events in a Josephson junction (and therefore reproduce the correct results), they do not provide an accurate physical description of the tunneling processes. In the Josephson representation (Figure 6.9), the pairs have E= μ (μ=chemical potential) and all the quasiparticle states empty at T=0) are higher in energy. The trap fills via pairbreaking which creates an extra quasiparticle in the electrode. Similarly, the emptying of the trap occurs by recombination of the trapped electron with a quasiparticle to reform a pair. In addition to gap effects, the

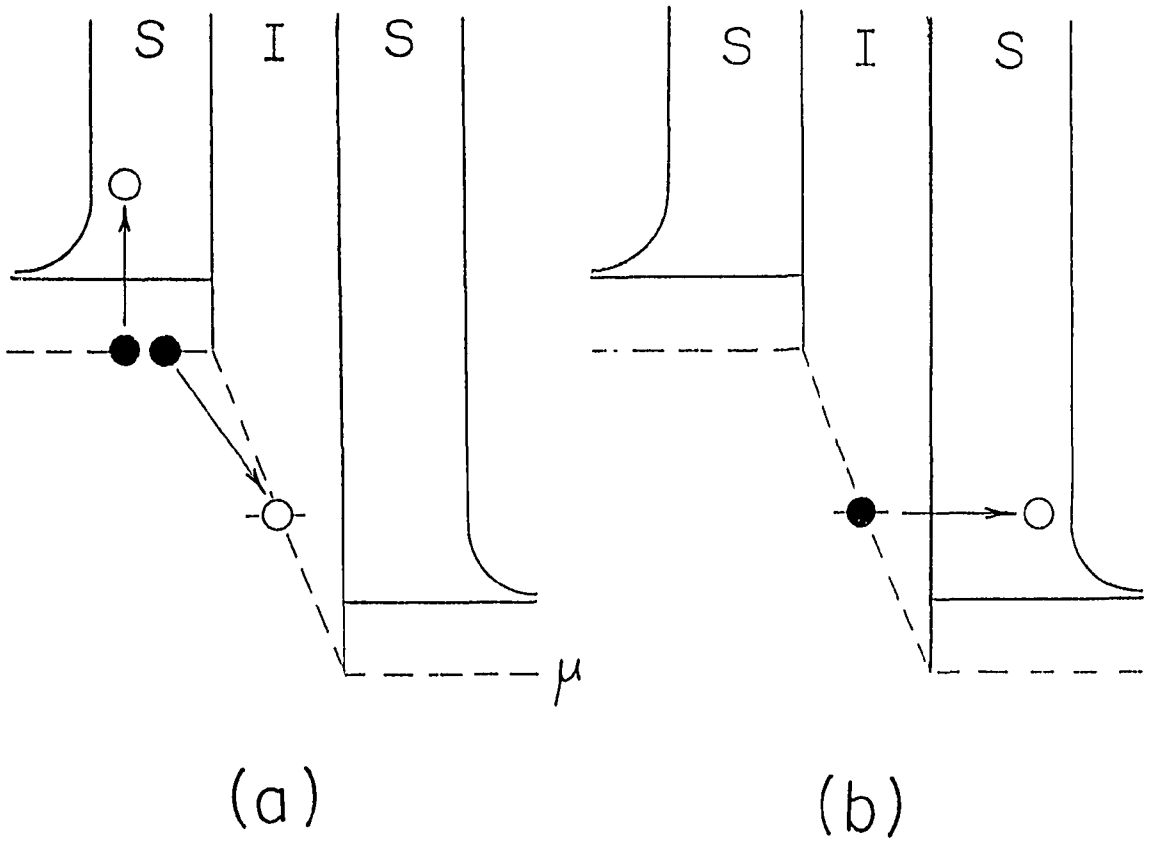

Figure 6.9 - Josephson representation of junction showing Cooper pairs at the chemical potential and quasiparticle states with $E>\Delta$. (a) Trap fills via pairbreaking and (b) empties via tunneling of the electron.

superconducting properties of the electrodes may well play other important roles in the trapping kinetics; however, a microscopic theory of the trapping process is presently lacking.

6.8 Electron trapping above and below V=2Δ/e

This section compares the electron trapping in dc SQUIDs and unshunted Josephson junctions. The key distinction between the two systems is that the SQUID is biased at voltages (<100μV) well below 2Δ/e= 2.4mV, while the junction is always biased at voltages above 2Δ/e, limited only by self-heating. Our simple model for the voltage bias dependence of the lifetimes suggests that the trapping kinetics may be very different in the SQUID where the energy level of the trap lies within the gap of both electrodes (Figure 6.7). Because of the energy gap, there are no states available to fill or empty the trap by direct tunneling. Instead, thermally-excited quasiparticles tunnel into the barrier and fall into the trap via phonon emission. The trap can only empty by a reverse process involving phonon absorption.

We observe several important differences between the junction and SQUID noise: 1) the unshunted junctions all display a typical 1/f power spectrum (Figure 6.10) while the SQUID noise exhibits an unusual $f^{-2/3}$ frequency dependence as discussed in chapter 4. 2) The trap lifetimes measured in the SQUID show a stronger temperature dependence (Figure 6.11); however, the observed behavior is still in good agreement with the WKB tunneling result

$$\tau \sim 1 + C(kT/eV)^2 \qquad (6.5)$$

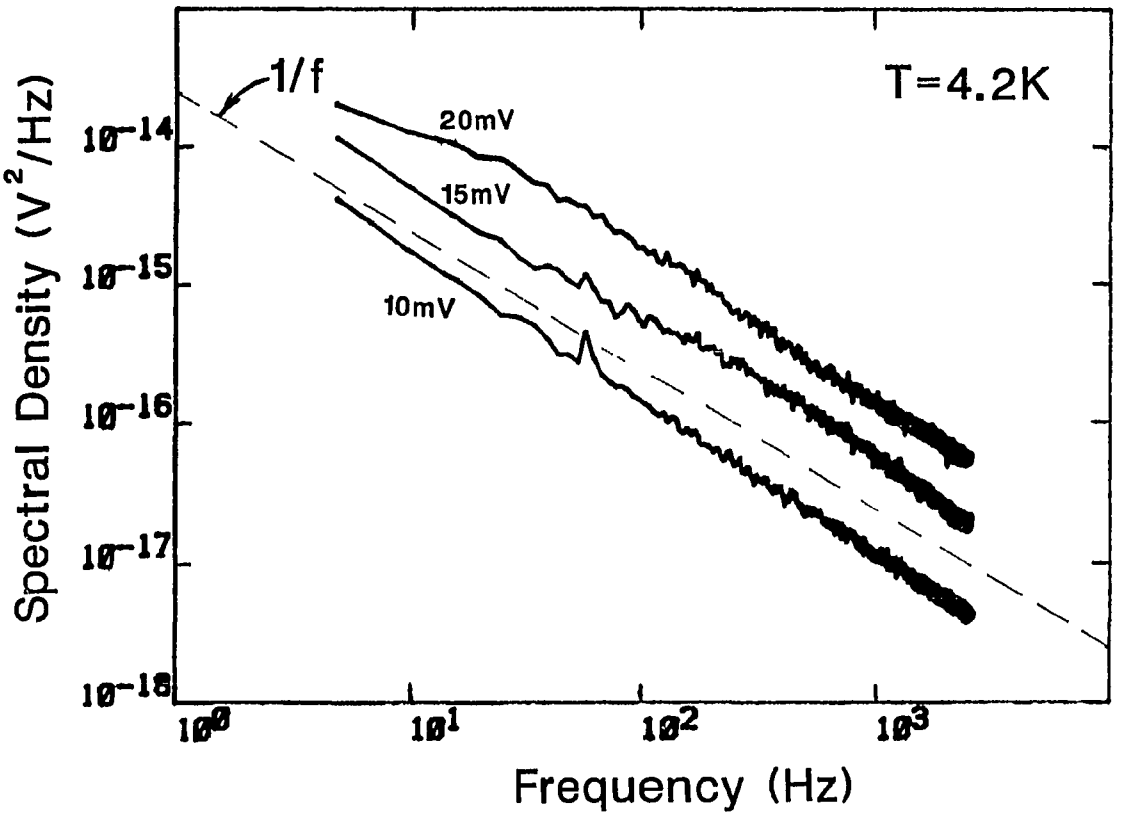

Figure 6.10 - Voltage noise of unshunted junction at 4.2K for three bias voltages.

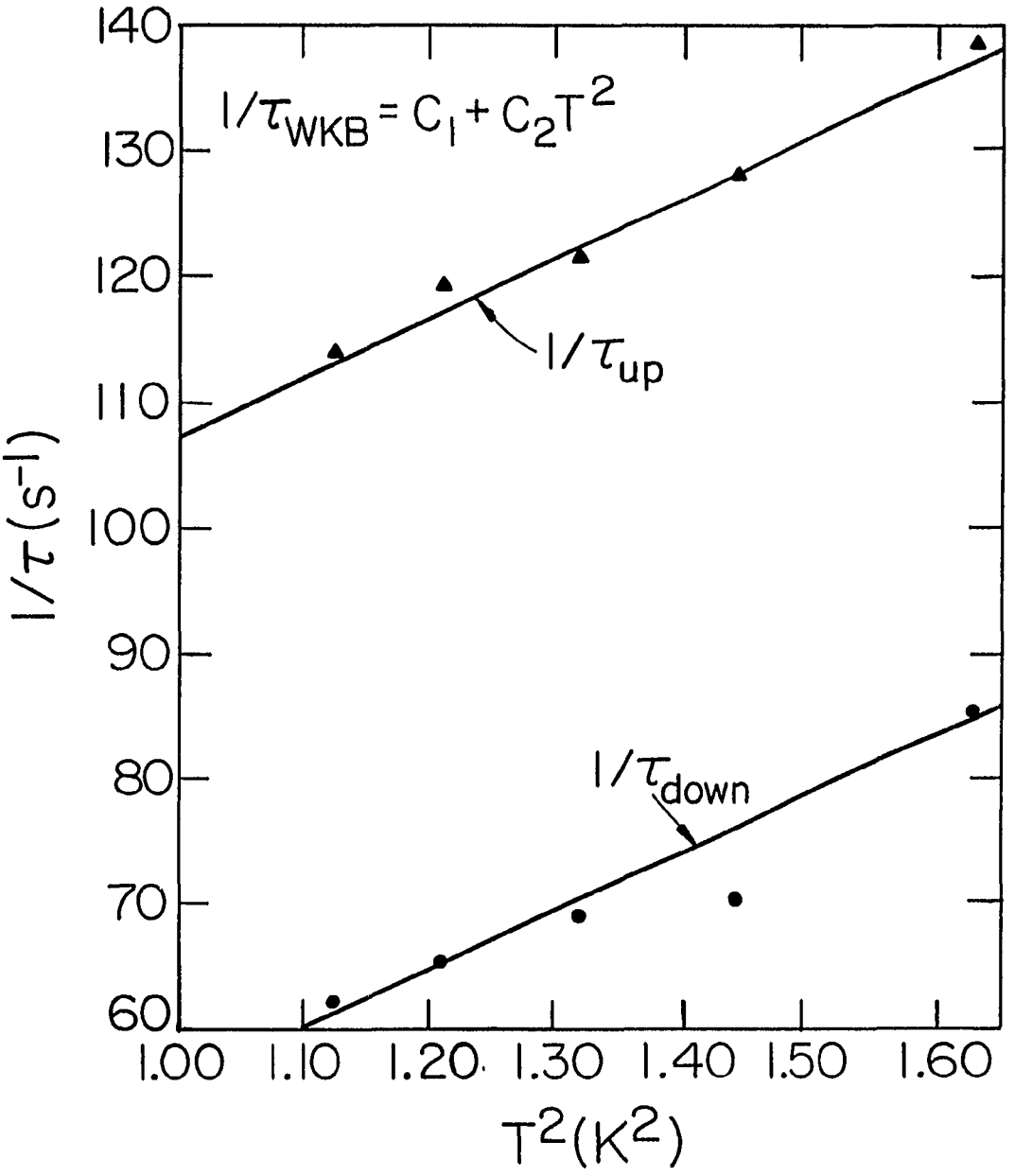

Figure 6.11 - Transition rates versus T^2 in a dc SQUID.

presented in section 6.2. Note that the stronger bias voltage dependence observed in the SQUID is predicted by (6.5) since the SQUID voltage is smaller. In addition, the value of the constant, C~100, deduced from Figure 6.11 is the same for both states and is of the expected order of magnitude for Poole-Frenkel tunneling of ions (Hill, 1971).

6.9 Interactions between traps and hierarchical noise kinetics

The data presented above was obtained by studying individual traps, but very often several traps are active at the same time. In most cases, the voltage noise shows a simple superposition of random telegraph signals as in Figure 6.12. In Figure 6.12a, the traps have similar lifetimes and switching amplitudes; Figure 6.12b shows the superposition of two traps with very different lifetimes. When the switching amplitude of the traps is similar as in these examples, it is possible that the noise may actually be due to a three-level system; however, in that case we would expect to see the system occasionally switch directly from the top to the bottom level as is never observed in these time traces.

In some instances, more complicated behavior is observed due to interactions between the traps as in Figure 6.13. Figure 6.13a seems to show a situation where a fast trap is active only when a neighboring slow trap is in the low voltage state. However, this can just as well be interpreted as a single three-level system where the up voltage state has two characteristic times-- one much longer and one much shorter than the lifetime for the down state. The time trace in Figure 6.13b shows very different two-level switching depending on the state of the slow, large amplitude trap. Note that in this example, there are three types of

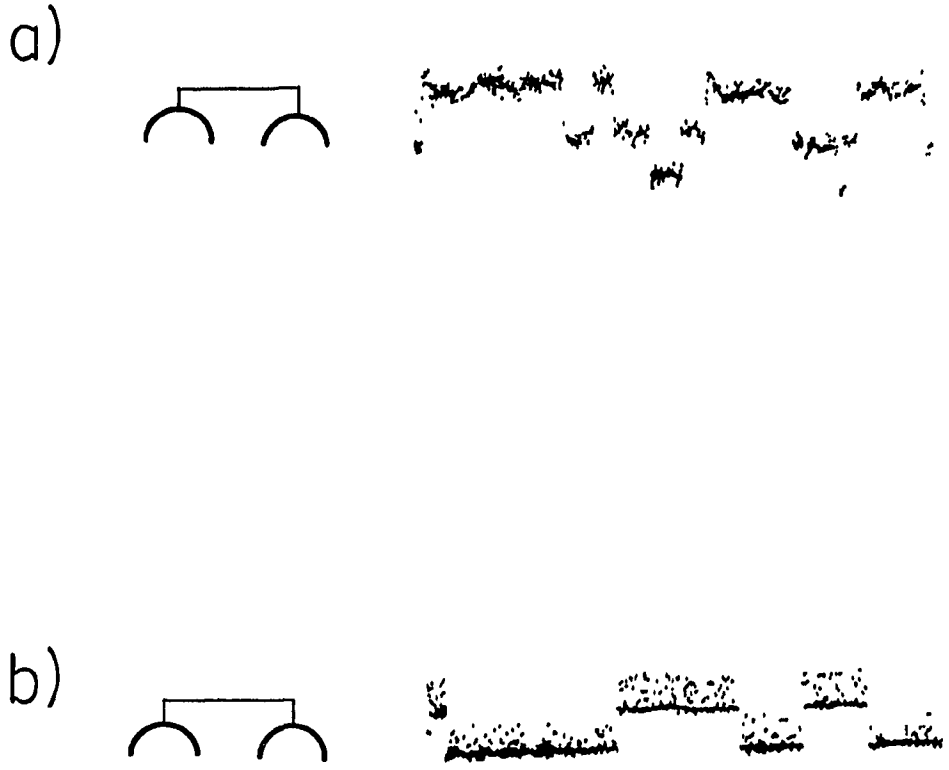

Figure 6.12 - Voltage switching due to the superposition of two two-level traps. (a) The lifetimes for both traps are similar. (b) The lifetimes of the traps are very different.

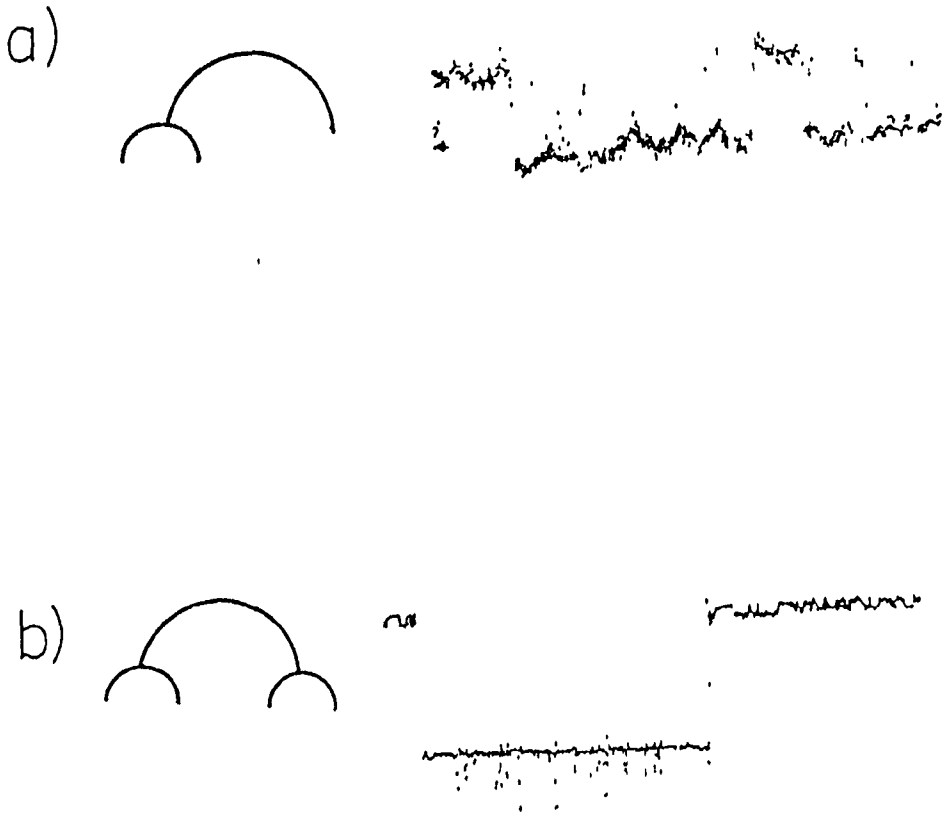

Figure 6.13 - Voltage switching resulting from trap interactions. (a) A fast trap is active only in the low voltage state. (b) Very different two-level switching is observed depending on the state of the slow, large amplitude trap.

switching present which have distinctly different amplitudes and lifetimes. This helps narrow the range of possible interpretations for the origin of the noise.

Figures 6.14a-d shows a very interesting sequence of time traces observed in the same $0.03\mu m^2$ junction at four different bias voltages. The top trace (4a) shows the simple superposition of a slow trap and a much faster trap. In the second trace (4b), a third voltage level appears which is much quieter than the top two levels. The third trace (4c) shows perhaps the most intriguing behavior we have seen. The noise in the lower level is always quiet, while the noise in the upper level can be either quiet or noisy. However, the upper level only shows transitions from the quiet state to the noisy state; it never switches from noisy to quiet, in gross violation of detailed balance. In addition, note that this transition does not exhibit a discrete jump in voltage level. This suggests that it may be associated with the simple movement of an ion and not a charge trapping event. The bottom trace (4d) shows very different two-level switching depending upon the state of the slow, large amplitude switching. These remarkable observations show that the voltage bias can not only change the lifetimes of the individual traps, but can also alter the qualitative appearance of the noise by affecting the interactions between traps.

The distinct types of switching described above can be classified in terms of a hierarchy of configurational states which is organized according to the dynamical relationship between the different states of the system. The schematic diagrams on the left of Figures 6.12, 6.13, and 6.14 depict our interpretation of the hierarchical relationships as

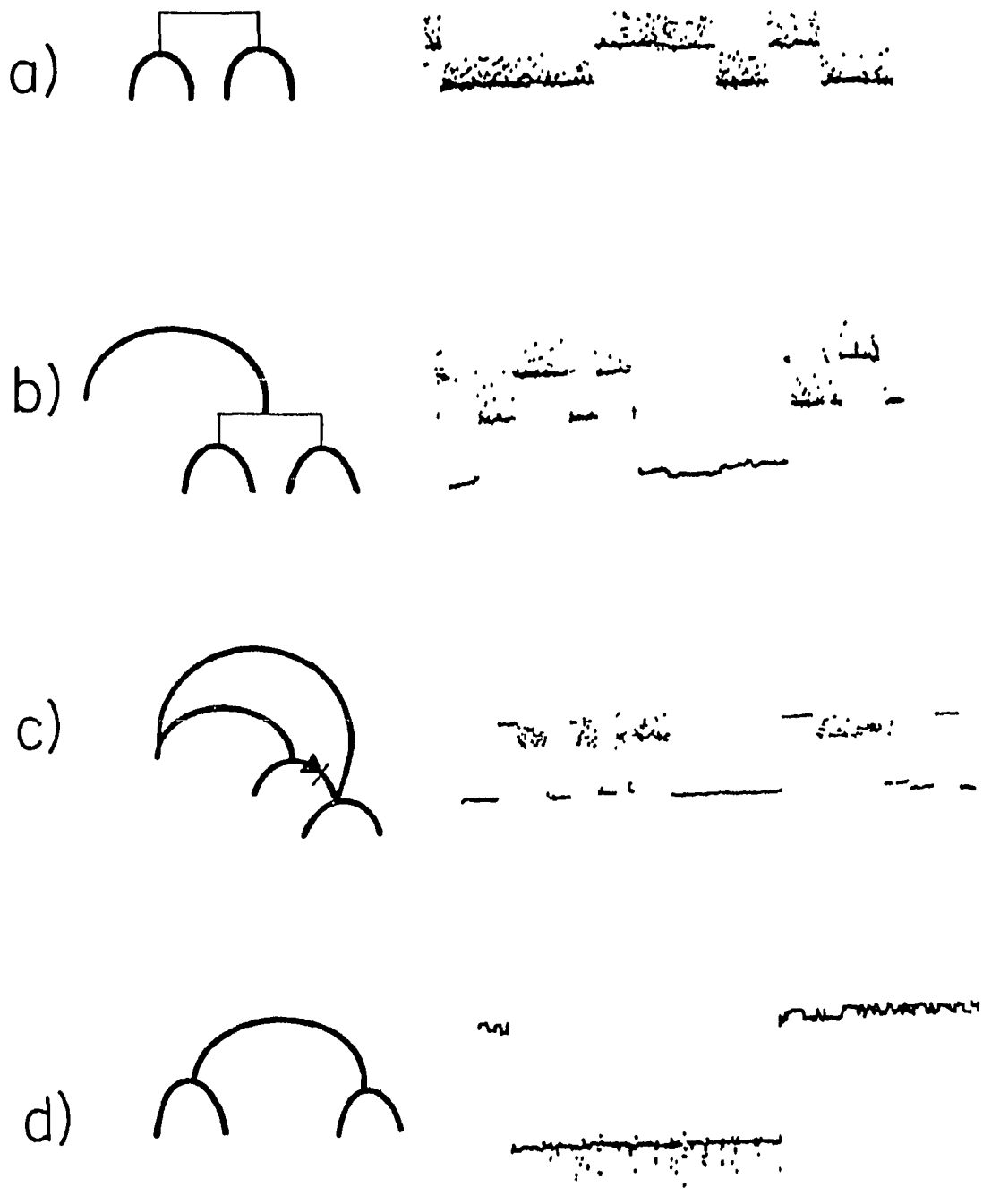

Figure 6.14 - Voltage switching in a 0.03μm^2 junction at four different bias voltages.

deduced from the time traces. Heavy, curved lines represent discrete two-state (trapping) processes. Parallel (independent) processes are connected by thin, straight brackets. Series processes, which by definition are not active at the same time, are connected via another two-state process which controls which of the two traps is active. The amplitude and time scale of the switching provides a convenient means for distinguishing the different levels of the hierarchy; slow, large amplitude switching is generally associated with the upper levels. Note that the unusual behavior in Figure 6.14c does not fit naturally into this simple picture. The apparent violation of detailed balancing requires that one of the connections has diode-like properties; i.e. transitions occur in only one direction.

The time traces in Figures 6.13 and 6.14b-d provide examples of noise that exhibits series kinetics. Series or highly-coupled kinetics are most often associated with systems that have scale invariance (e.g. a spin glass). Though this is clearly not the case here, the existence of hierarchical kinetics in our junctions is not surprising. All systems exhibit interactions to some degree, but as long as the interactions are short-ranged compared to the mean fluctuator spacing, the majority of fluctuators can be assumed to be independent. In our junctions, this assumption fails because of the long-ranged potential of the weakly-screened electron trap; moreover, recent studies of silicon surfaces by Koch and Hamers (1987) using STM (scanning tunneling microscopy) have shown that the surface electron traps tend to cluster. This observation may further explain the surprisingly frequent occurrence of interactions within our junctions. When the noise of these ultrasmall devices is

dominated by a small number of strongly interacting traps, hierarchical fluctuation kinetics will be observed.

In conclusion, we have measured the emission and capture time of individual electron traps residing within the tunneling barrier of very small-area Josephson junctions. Below 4K, the times become constant which demonstrates that the trapping kinetics are dominated by tunneling and implies that the trap remains active even at zero temperature. The voltage bias dependence of the times is consistent with a simple model which predicts that increasing the bias enhances the rate for electrons to tunnel into the trap from one side of the barrier and exit out the opposite side. Finally, we have recorded a variety of complex interactions between traps. The interactions are affected by bias conditions and result in a voltage noise that displays series kinetics. These findings suggest that coupled kinetics may play an important role in determining the dynamic and thermodynamic properties of this system.

REFERENCES

Ambegaokar, V. and Baratoff, A., Phys. Rev. Lett. 10, 486 (1963).

Anderson, P.W., in Progress in Low Temperature Physics, v. 5, ed. C.J. Gorter, (North-Holland, Amsterdam, 1967).

Arai, M.R. and Ambegaokar, V., J. Low Temp. Phys. 47, 499 (1982).

Bardeen, J., Cooper, L.N., and Schrieffer, J.R., Phys. Rev. 108, 1175, (1957).

Caldeira, A.O. and Leggett, A.J., Phys. Rev. Lett. 46, 211 (1981).

Callen, H.B. and Welton, T.A., Phys. Rev. 83, 34 (1951).

Carelli, P. and Foglietti, V., IEEE Trans. Mag. MAG-19, 299 (1983).

Clarke, J., Goubau, W.M., and Ketchen, M.B., J.Low Temp. Phys. 25, 99 (1976).

Clarke, J., in Superconductor Applications: SQUIDs and Machines, ed. B.B. Schwartz and S. Foner, (Plenum, New York, 1977).

Cromar, M.W. and Carelli, P., Appl. Phys. Lett. 38, 723 (1981).

De Gennes, P.G., Superconductivity in Metals and Alloys, (Benjamin, New York, 1966).

Dutta, P., Dimon, P., and Horn, P.M., Phys. Rev. Lett. 43, 646 (1979).

Eisenmenger, W., in Physical Acoustics, ed. W.P. Mason and R.N. Thurston, (Academic Press, New York, 1976).

Falco, C.M., Parker, W.H., Trullinger, S.E., and Hansma, P.K., Phys. Rev. B10, 1865 (1974).

Foglietti, V., Gallagher, W.J., Ketchen, M.B., Kleinsasser, A.W., Koch, R.H., Raider, S.I., and Sandstrom, R.L., Appl. Phys. Lett. 49, 1393, (1986).

Forster, D., Hydrodynamic Fluctuations, Broken Symmetry, and Correlation Functions, (Benjamin/Cummings, Reading, Mass., 1975).

Freeman, M.R., Germain, R.S., Richardson, R.C., Roukes, M.L., Gallagher, W.J., and Ketchen, M.B., Appl. Phys. Lett. 48, 300 (1986).

Fulton, T.A. and Dunkelburger, L.N., Phys. Rev. B9, 4760 (1974).

Gray, K.E., editor of Nonequilibrium Superconductivity, Phonons, and Kapitza Boundaries, proceedings of NATO Advanced Study Institute held in Acquafredda di Marates, Italy, August 1980, (Plenum, New York, 1981).

Greiner, J.H., Kircher, C.J., Klepner, S.P., Lahiri, S.K., Warnecke, R.J., Basavaiah, S., Yen, E.T., Baker, J.M., Brosius, P.R., Huang, H.-C.W., Murakami, M., and Ames, I., IBM J. Res. Dev. 24, 195 (1980).

Hilbert, C. and Clarke, J., J. Low Temp. Phys. 61, 263 (1985a).

Hilbert, C., Clarke, C., Sleator, T., and Hahn, E.L., Appl. Phys. Lett. 47, 639 (1985b).

Hill, R.M., Phil. Mag. 23, 59 (1971).

Howard, R.E., Skocpol, W.J., Jackel, L.D., Mankiewich, P.M., Fetter, L.A., Tennant, D.M., and Epworth, R.W., IEEE Trans. Elec. Dev. ED-32, 1669 (1985).

Ivanchenko, Yu. M. and Zil'berman, L.A., Sov. Phys. JETP 28, 1272 (1968).

Josephson, B.D., Phys. Lett. 1, 251 (1962).

Ketchen, M.B. and Voss, R.F., Appl. Phys. Lett. 35, 812 (1979).

Ketchen, M.B. and Tsuei, C.C., Proceedings SQUID '80, ed. H.D. Halbohm and H. Lubbig, (de Gruyter, New York, 1980).

Ketchen, M.B. and Jaycox, J.M., Appl. Phys. Lett. 40, 736 (1982).

Kirton, M.J. and Uren, M.J., Appl. Phys. Lett. 48, 1270 (1986).

Kleinsasser, A.W. and Buhrman, R.A., Appl. Phys. Lett. 37, 841 (1980).

Koch, R.H., Van Harlingen, D.J., and Clarke, J., Phys. Rev. Lett. 45, 2132 (1980).

Koch, R.H., Van Harlingen, D.J., and Clarke, J., Appl. Phys. Lett. 38, 380 (1981)

Koch, R.H., Clarke, J., Goubau, J., Martinis, J., Pegrum, C., and Van Harlingen, D.J., J. Low Temp. Phys. 51, 107 (1983).

Koch, R.H. and Hamers, R.J., Bull. Am. Phys. Soc. 32, 394 (1987).

Kurkijarvi, J. and Ambegaokar, V., Phys. Lett. 31A, 314 (1970).

Langenberg, D.N., Rev. Phys. Applique 9, 35 (1974).

Likharev, K.K. and Semenov, V.K., JETP Lett. 15, 442 (1972).

Likharev, K.K. and Zorin, A.B., J. Low Temp Phys. 59, 347 (1985).

Machlup, S., J. Appl. Phys. 25, 341 (1954).

Magerlein, J.H., J. Appl. Phys. 54, 2569 (1983).

Mankiewich, P.M., Howard, R.E., Jackel, L.D., Skocpol, W.J., and Tennant, D.M., J. Vac. Sci. Tech. B4, 380 (1986).

McCumber, D.E., J. Appl. Phys. 39, 3113 (1968).

Nyquist, H., Phys. Rev. 22, 110 (1928).

Ralls, K.S., Skocpol, W.J., Jackel, L.D., Howard, R.E., Fetter, L.A., Epworth, R.W., and Tennant, D.M., Phys. Rev. Lett. 52, 228 (1984).

Reif, F., Fundamentals of Statistical and Thermal Physics, (McGraw-Hill, New York, 1965).

Reim, W., Koch, R.H., Malozemoff, A.P., Ketchen, M.B., and Maletta, H., Phys. Rev. Lett. 57, 905 (1986).

Rogers, C.T. and Buhrman, R.H., Phys. Rev. Lett. 53, 1271 (1984).

Rogers, C.T. and Buhrman, R.H., Phys. Rev. Lett. 55, 859 (1985).

Schmid, A., J. Low Temp. Phys. 49, 609 (1982).

Schmidlin, F.W., J. Appl. Phys. 37, 2823 (1966).

Stewart, W.C., Appl. Phys. Lett. 12, 277 (1969).

Taylor, B.N., Parker, W.H., and Langenberg, D.N., Rev. Mod. Phys. 41, 375 (1969).

Tesche, C.D. and Clarke, J., J. Low Temp. Phys. 37, 397 (1979).

Tesche, C.D., Appl. Phys. Lett. 41, 99 (1982).

Tesche, C.D., Brown, K.H., Callegari, A.C., Chen, M.M., Greiner, J.H., Jones, H.C., Ketchen., M.B., Kim, K.K., Kleinsasser, A.W., Notarys, H.A., Proto, G., Wang, R.H., and Yogi, T., IEEE Trans. Mag. MAG-21, 110 (1985).

Tesche, C.D., Proceedings SQUID '85, ed. H.D. Halbohm and H. Lubbig, (de Gruyter, Berlin, 1985).

Tinkham, M., Introduction to Superconductivity, (McGraw-Hill, New York, 1975).

Tucker, J.R. and Feldman, M., Rev. Mod. Phys. 57, 1055 (1985).

Van Harlingen, D.J., Koch, R.H., and Clarke, J., Appl. Phys. Lett. 38, 380 (1981).

Voss, R.F., Laibowitz, R.B., Raider, S.I., and Clarke, J., J. Appl. Phys. 51, 2306 (1980).

Voss, R.F., Laibowitz, R.B., Broers, A.N., Raider, S.I., Knoedler, C.N., and Viggiano, J.M., IEEE Trans. Mag. MAG-17, 395 (1981).

Wakai, R.T. and Van Harlingen, D.J., Proceedings SQUID '85, ed. H.D. Halbohm and H. Lubbig, (de Gruyter, Berlin, 1985).

Wakai, R.T. and Van Harlingen, D.J., Appl. Phys. Lett. 49, 593 (1986)

Wakai, R.T. and Van Harlingen, D.J., Phys. Rev. Lett. 58, 1687 (1987).

Waldram, J.R., Rep. Prog. Phys. 39, 751 (1976).

Weissman, M.B., to be published in Rev. Mod. Phys.

Wellstood, F.C., Urbina, C., and Clarke J., Bull. Am. Phys. Soc. 31, 386, (1986).

VITA

Ronald Tatsuya Wakai was born November 7, 1958 in East Orange, New Jersey. He graduated from Cornell University in 1980 and received a masters degree in physics from the University of Illinois in 1981.